Portable laser-heating system for experiments with diamond anvil cells and its application to studies of geophysically important materials

Von der Fakultät für Biologie, Chemie und Geowissenschaften

der Universität Bayreuth

zur Erlangung der Würde eines

Doktors der Naturwissenschaften

– Dr. rer. nat. –

Dissertation

Vorgelegt durch

Ilya Kupenko, aus Moskau (Russland)

Bayreuth, 2014

This doctoral thesis was prepared at the department of Bayerisches Geoinstitut at the University of Bayreuth and at European Synchrotron Radiation Facility from 01/2011 to 01/2013 and was supervised by Prof. Dr. Leonid Dubrovinsky (Bayerisches Geoinstitut) and Dr. Alexander Chumakov (European Synchrotron Radiation Facility).

This is a full reprint of the dissertation submitted to obtain the academic degree of Doctor of Natural Sciences (Dr. rer. nat.) and approved by the Bayreuth Graduate School of Mathematical and Natural Sciences (BayNAT) of the University of Bayreuth.

Date of submission: 30.05.2014

Date of defense: 07.10.2014

Acting director: Prof. Dr. Franz Xaver Schmid

Doctoral committee:

Prof. Dr. Leonid Dubrovinsky   (1st reviewer)

Dr. Gerd Steinle-Neumann   (2nd reviewer)

Prof. Dr. Tomoo Katsura   (chairman)

Prof. Dr. Jürgen Senker

Zusammenfassung

Untersuchungen unter extremen Bedingungen sind ein wichtiges Hilfsmittel bei der Herstellung neuer Materialien und deren Charakterisierung hinsichtlich der physikalischen und chemischen Eigenschaften. Solche Experimente sind nicht nur in der Physik, Chemie und den Materialwissenschaften sondern auch in den Geowissenschaften interessant, da sie eine Möglichkeit eröffnen, geophysikalisch relevante Materialien unter Bedingungen des tiefen Erdinneren zu untersuchen. Der Schwerpunkt der hier vorliegenden Arbeit liegt auf dem Entwurf und Test eines mobilen kombinierten Hochdruck- und Hochtemperatursystems und dessen Verwendung, um eine fundamentale Fragestellung in der Hochdruck-Mineralphysik zu beantworten, nämlich die Frage hinsichtlich der Platzbesetzung und der elektronischen Konfiguration von Eisen in eisen- und aluminiumhaltigen $MgSiO_3$ Perowskiten unter Bedingungen des unteren Erdmantels. Eine weitere Anwendung dieses Aufbaus, nämlich Untersuchungen zur Hochdruckphase eines potentiellen Wasserstoffspeichermaterials, Amminboran, wird in dieser Arbeit beschrieben.

I.   Entwurf des mobilen Laserheizsystems für Experimente mit Diamantstempelzellen

Die Technik der Laserheizung für Diamantstempelzellen ist augenblicklich die einzige Möglichkeit, Temperaturen von tausenden von Grad unter statischen Drücken im vielfachen Megabar-Bereich zu erreichen, um die Bedingungen des tiefen Erdinneren zu simulieren. Wir haben ein mobiles doppelseitiges Laserheizsystems entwickelt, dass sich einfach zwischen dem Labor und verschiedenen Beamlines einer Synchrotronstrahlungsquelle transportieren läßt. Dieses System erlaubt es, verschiedene analytische Techniken mit in-situ Experimenten unter extremen Bedingungen zu koppeln. Es ermöglicht die Benutzung der Laserheizung zusammen mit der Diamantstempelzellentechnik für Experimente, die eine Bewegung des gesamten Aufbaus als Einheit benötigen, wie z.B. Einkristall-Beugungsexperimente. Unsere technischen Entwicklungen haben die Aufbauzeit für das System auf 2-3 Stunden reduziert.

Das System besteht aus zwei Hauptteilen – die Laserlichtquelle und die Laser-Heizköpfe. SPI Fiberlasers werden als Quelle benutzt und Glasfasern erlauben es, die Netzteile mit der Laserlichtquelle (40 kg) von deren optischen Teilen zu trennen und damit den Platz für die

Probenumgebung zu reduzieren. Die Laser-Heizköpfe beruhen auf einem „FineCutter" System der Fa. Precitec KG. Sie verbinden die Aufgaben der Fokussierung des Laserlichts, der in-situ Probendarstellung, der Beleuchtung und des Erfassens der ausgesandten thermischen Strahlung zur Temperaturmessung.

Erste Experimente mit dem Aufbau wurden an der European Synchrotron Radiation Facility (ESRF) durchgeführt. Dies waren zum einen Einkristall-Beugungsexperimente mit $(Mg_{0.87}Fe_{0.13})(Si_{0.89}Al_{0.11})O_3$ Perowskiten an der Hochdruckstation der White Beam beamline ID09A (Häuserma and Hanfland, 1996) und zum anderen SMS Experimente (Potapkin et al., 2012) mit $(Mg_{0.8}Fe_{0.2})O$ Ferroperiklas an der Nuclear Resonance beamline ID18 (Rüffer and Chumakov, 1996).

II.   Platzbesetzung und elektronische Konfiguration von Eisen in eisen- und aluminiumhaltigen Magnesium-Silikat-Perowskiten.

Eisen- und aluminiumhaltiges $MgSiO_3$ in der Perowskitstruktur (FeAlPv) könnte wenigstens 75% des unteren Erdmantels ausmachen. Es wird vermutet, dass Eisen in dieser Struktur als Eisen(III) und Eisen(II) enthalten ist. FeAlPv hat zwei verschiedene Kationenplätze: einen großen, verzerrten dodekahedral Platz (A-Platz) und einen kleinen, relativ ungestörten oktahedral Platz (B-Platz). Während allgemeine Übereinstimmung herrscht, dass Fe^{2+} allein den A-Platz besetzt, ist die Besetzung von Fe^{3+} in der Diskussion. Einerseits wird berichtet, dass Eisen(III) exklusiv den A-Platz besetzt (McCammon et al., 2008; Potapkin et al., 2013; Vanpeteghem et al., 2006), andererseits jedoch beide Plätze, A und B (Catalli et al., 2011; McCammon, 1997). Weitere Untersuchungen behaupten zusätzlich, dass unter Hochdruck und hohen Temperaturen eine Platzaustauschreaktion stattfindet: $Fe_A^{3+}+Al_B^{3+}\rightarrow Fe_B^{3+}+Al_A^{3+}$ (Catalli et al., 2011; Fujino et al., 2012).

Um die Hypothese des Platzaustausches zu verifizieren, haben wir in-situ Hochdruck-Hochtemperatur-Einkristallbeugungsuntersuchungen von $(Mg_{0.87}Fe^{3+}_{0.09}Fe^{2+}_{0.04})(Si_{0.89}Al_{0.11})O_3$ Perowskiten an der Beamline ID09A der ESRF durchgeführt. Die chemische Zusammensetzung beruht auf den Ergebnissen der Elektronen-Mikrostrahlanalyse und der Mössbauerspektroskopie. Wir nahmen mehrere Datensätze zwischen 65 und 78 GPa: vor, während und nach der Laserheizung bei 1750(50) K. Zusätzlich zu den Atomkoordinaten und den isotropen

thermischen Parametern haben wir die Besetzungszahl des B-Platzes, unter Berücksichtigung von Fe und Si (Fe und Si sind in unseren Einkristallbeugungsuntersuchungen nicht unterscheidbar) und des A-Platzes durch Mg und Fe, besser bestimmt. Der Eisengehalt des A-Platzes stimmt innerhalb des Fehlers mit dem gewonnenen Wert aus der Elektronen-Mikrostrahlanalyse überein. Länger andauernde Laserheizung bei 1750 K hat keinen sichtbaren Austausch von Al und Fe zwischen den Plätzen erkennen lassen; damit gibt es keinen Hinweis, dass Fe den B-Platz besetzt. Unsere Ergebnisse stimmen gut mit den kürzlich erzielten Ergebnissen von Glazyrin et al. (2014) von Fe^{3+}- und Al^{3+}-reichen Perowskiten überein.

Der Spinzustand des Eisens im Krustenmaterial kann die Eigenschaften und Dynamik des Erdinneren signifikant beeinflussen. In Ferroperiklas wurde ein Spinübergang vom hohen Spin (HS) zum niedrigen Spin (LS) in Eisen(II) bei Drücken über 50 GPa beobachtet. Berichte von Änderungen des Spinzustandes in FeAlPv mit unterschiedlichen Valenzen sind kontrovers. Experimentelle Untersuchungen haben gezeigt, dass Eisen(II) in FeAlPv einen HS – IS (intermediären Spin) Übergang oberhalb von 35 GPa macht. Simulationen ergeben jedoch, dass der HS Zustand von Fe^{2+} bei allen Drücken des unteren Erdmantels der stabilste ist. Eisen(III) auf den A-Plätzen bleibt in allen Druckbereichen des unteren Erdmantels im HS Zustand; wohingegen Eisen(III) auf den B-Pätzen einen HS-LS Übergang oberhalb von etwa 50 GPa macht. Dieser letzte Prozeß wird mit einer Platzwechsel-Reaktion, wie oben beschrieben, in Verbindung gebracht.

Die meisten der oben genannten Arbeiten extrapolieren die bei Raumtemperatur gewonnenen Hochdruckdaten bezüglich des Spinzustandes des Eisens zu Temperaturen des unteren Erdmantels. Bei McCammon et al. (2008) war die Temperatur auf 1000 K begrenzt und die Ergebnisse zeigten die Stabilität des Fe^{2+} IS-Zustandes über den des Fe^{2+} HS-Zustandes. Um nun die elektronische Konfiguration des Eisens unter den Bedingungen des tiefen Erdinneren zu bestimmen, führten wir die ersten in-situ Untersuchungen von $Mg_{0.83}Fe_{0.20}Al_{0.06}Si_{0.92}O_3$ Perowskiten bei Drücken bis zu 81 GPa und Temperaturen bis zu 2000 K mit NFS und SMS durch. Konventionelle Mössbauermessungen bei Raumtemperatur ergänzten die Untersuchungen.

Alle drei Methoden zeigten das Erscheinen einer neuen Fe^{2+} Komponente bei Drücken oberhalb von 35 GPa, die wir dem IS Spinzustand zuschreiben genauso wie in den vorherigen Arbeiten.

Die NFS Daten lassen einen scharfen HS-LS Übergang (< 20 GPa) vermuten; die MB und SMS Daten weisen jedoch auf einen langsamen Übergang hin, der sogar bei den höchsten erreichbaren Drücken nicht vollständig ist. Der Unterschied zu vorherigen Beobachtungen scheint in der NFS Technik zu liegen, welche bei sehr frühen Zeiten von der elektronischen Streuung überlagert ist und somit hier nicht immer für eindeutige Ergebnisse sorgt. Diese frühen Zeiten entsprechen jedoch bei MB und SMS den breiten Linien im Spektrum, wie sie im Fall des HS Fe^{2+} anzutreffen sind.

Es gab keinen Hinweis auf einen Spinübergang des Eisen(III) der A-Plätze. Nach Laserheizung bei Drücken oberhalb von 40 GPa wurde eine kleine Komponente (etwa 5%) beobachtet, von der angenommen wird, von LS Fe^{3+} auf den B-Plätzen herzurühren. Dieser kleine Beitrag des Eisens auf den B-Plätzen ist unterhalb der Nachweisgrenze von Röntgenstreumethoden. Die Tatsache von LS Fe_{B}^{3+} ist wahrscheinlich eher kontrolliert von einer Umverteilung von Kationen-Leerstellen als von einer Platzwechselreaktion zwischen Fe^{3+} und Al^{3+}. Der geringe Anteil an LS Fe^{3+}, der in FeAlPv in einer Zusammensetzung, die relevant zum unteren Erdmantel ist, gefunden wurde, zeigt, dass der HS-LS Übergang in Eisen(III) eine vernachlässigbare Rolle bei der Bestimmung der Eigenschaften im tieferen Erdinneren spielt.

NFS und SMS Hochdruck-/Hochtemperaturdaten können durch eine Überlagerung von Unterspektren, die heißen und relativ kalten Teilen der Probe entsprechen und wahrscheinlich von Temperaturgradienten in der Probe herrühren, angepaßt werden. Unsere Daten zeigen, dass der hohe Eisen(III)-Anteil, der kürzlich in abgeschreckten Proben beobachtet wurde, auch unter relevanten Bedingungen des unteren Erdmantels erhalten bleibt. Unsere Daten zeigen auch, dass der Hauptanteil des Eisen(III) in FeAlPv unter Bedingungen des tiefen Erdinneren im HS Zustand erhalten bleibt; wohingegen Eisen(II) in FeAlPv in den IS Zustand übergeht.

III.   Druckinduzierte Strukturänderungen im BH₃NH₃ Komplex

Der Amminboran-Komplex, BH_3NH_3 (**AB**), ist wegen seiner hohen Wasserstoff-Volumendichte ein potenzieller Kandidat für die Wasserstoffspeicherung (Stephens et al., 2007). Unter gewöhnlichen Bedingungen kristallisiert **AB** in der tetragonalen Struktur (Raumgruppe *I4mm*) mit nichtgeordnetem Wasserstoff (Bowden et al., 2007). Sein Hochdruckverhalten wurde in der letzten Dekade gründlich untersucht. Die Synthese von dichteren **AB** Polymorphen würde die

Existenz von Materialien mit großer Wasserstoffdichte, die sogar höher als die des tetragonalen **AB** wäre, bedeuten. Während generelle Übereinstimmung bezüglich des Phasenübergangs von der tetragonalen *I4mm* zu der orthorombischen *Cmc2$_1$* Struktur nahe 1 GPa besteht (e.g., Chellappa et al., 2009; Filinchuk et al., 2009), bleiben die Berichte über Phasenübergänge bei höheren Drücken kontrovers (e.g., Chen et al., 2010; Kumar et al., 2010; Lin et al., 2012).

Um diese Phasenübergänge zu untersuchen, führten wir in-situ Ramanspektroskopie unter Hochdruck bis zu 65 GPa durch. Wir fanden heraus, dass sich **AB** unter quasi-hydrostatischen und nicht-hydrostatischen Bedingungen unterschiedlich verhalten. Das mag die Unterschiede in den Beobachtungen der Phasenübergänge unter 12 GPa erklären. Unsere Messungen bestätigen den Phasenübergang bei etwa 12 GPa (Lin et al., 2008) und lassen einen neuen Übergang bei etwa 27 GPa unter quasi-hydrostatischen Bedingungen vermuten.

Wir haben beobachtet, dass **AB** nichtlineare optische Eigenschaften besitzt, die die Frequenzverdopplung (SHG) des Laserlichts ermöglichen. Die Beobachtung des transmittierten Signals der SHG wurde für die Entwicklung und den Test der oben beschriebenen mobilen Laserheizung benutzt. Dies war speziell für die Verbesserung der Fokussierungsmöglichkeiten der Laserstrahlen hilfreich. Die geringe Streustärke der Atome von **AB** macht Röntgenbeugungsuntersuchungen schwierig, was jede zusätzliche Strukturinformation wertvoll macht. SHG ist nur in anisotropen Medien ohne Inversionssymmetrie möglich. Wir haben SHG beim Durchgang von Nd:YAG (λ = 1072 nm) Laserlicht durch **AB** bei Drücken bis zu 130 GPa beobachtet. Das läßt vermuten, dass die nicht-zentrosymmetrische Punktgruppensymmetrie in diesem Material bis zu sehr hohen Drücken erhalten bleibt.

Summary

Experiments under extreme conditions are an important tool for synthesis of new materials and investigation of physical and chemical properties. Such experiments are of interest not only to physics, chemistry and materials science, but also to geoscience because they provide the opportunity to probe the properties of geophysically relevant materials at conditions of the deep Earth's interior. The current work focuses on the design and testing of a portable system for simultaneous high pressure and high temperature generation and its application in resolving one of the fundamental problems of high-pressure mineral physics, namely the site occupancy and iron electronic configuration in Fe-, Al-bearing $MgSiO_3$ perovskite at conditions of the Earth's lower mantle. The work also demonstrates the application of the developed setup to the investigation of the high-pressure phases of a potential hydrogen storage material, ammonia borane complex.

I. Design of the portable laser-heating system for experiments with diamond anvil cells

The technique of laser heating in diamond anvil cells (DACs) is currently the only way to achieve temperatures of thousands of degrees statically at pressures in the multi-megabar range in order to simulate conditions of the deep Earth's interior. We developed a portable double-sided laser-heating system that can be easily transferred between the laboratory and a synchrotron and between different synchrotron beamlines. The portable system allows for coupling of numerous analytical techniques with *in situ* experiments under extreme conditions. It gives the possibility to use the laser-heating DAC technique for experiments that require movement of the entire setup as a single unit, for example single crystal X-ray diffraction. Our technical developments reduced the time for installation of the laser-heating setup at beamlines to only 2-3 hours.

The system consists of two main parts – a source of laser light and the laser-heating heads. SPI fiber lasers are used as the laser sources, and fibers allow the power units of the laser sources (40 kg) to be separated from the optical parts of the system, hence decreasing the space required for the sample environment. The laser-heating heads are based on a fine cutting device produced by Precitec KG. The laser heads combine the functions of laser beam focusing, *in situ* sample

imaging, illumination, and collection of the emitted thermal radiation for temperature measurements.

The first applications of the setup were demonstrated at the European Synchrotron Radiation Facility (ESRF). These comprise a single crystal X-ray diffraction investigation on $(Mg_{0.87}Fe_{0.13})(Si_{0.89}Al_{0.11})O_3$ perovskite at the High Pressure Station of the White Beam beamline ID09a (Häuserma and Hanfland, 1996) and a Synchrotron Mössbauer Source study (Potapkin et al., 2012) on $(Mg_{0.8}Fe_{0.2})O$ ferropericlase at the Nuclear Resonance beamline ID18 (Rüffer and Chumakov, 1996).

II.   Site occupancy and electronic configuration of iron in Fe-, Al-bearing magnesium silicate perovskite

Iron- and aluminum-bearing $MgSiO_3$ in the perovskite structure (FeAlPv) is considered to comprise at least 75% of the Earth's lower mantle (e.g., Irifune et al., 2010; Ringwood, 1982). Iron is expected to be incorporated into the structure in significant amounts as both ferric and ferrous iron. FeAlPv has two different cation sites – a large distorted dodecahedral site (A-site) and a small relatively undistorted octahedral site (B-site). While there is general consensus that Fe^{2+} occupies exclusively the A-site (i.e., Fe_A^{2+}) the site occupancy of Fe^{3+} is a matter of some debate. Ferric iron has been reported to occupy either exclusively the A-site (McCammon et al., 2008; Potapkin et al., 2013; Vanpeteghem et al., 2006) or to occupy both the A- and B- sites (McCammon, 1997; Catalli et al., 2011). Several studies have additionally proposed that a site exchange reaction takes place at high pressures and high temperatures: $Fe_A^{3+}+Al_B^{3+}\rightarrow Fe_B^{3+}+Al_A^{3+}$ (Catalli et al., 2011; Fujino et al., 2012).

In order to test the site exchange hypothesis we conducted an *in situ* high-pressure high-temperature single crystal X-ray diffraction investigation on $(Mg_{0.87}Fe^{3+}_{0.09}Fe^{2+}_{0.04})(Si_{0.89}Al_{0.11})O_3$ perovskite at beamline ID09a at the ESRF. The chemical formula is based on the results of electron microprobe analysis and Mössbauer spectroscopy. We collected several datasets between 65 and 78 GPa: before, during, and after laser heating at 1750(50) K. In addition to the atomic coordinates and isotropic thermal parameters we refined the occupancy of the B-site considering Fe and Si (Si and Al are not distinguishable within our single crystal X-ray diffraction experiments) and of the A-site by Mg and Fe. We found that the

refined amount of iron in the A-site coincided within uncertainty with the value determined by the electron microprobe. Extended laser heating at 1750 K did not cause any detectable exchange of Al and Fe between the sites; therefore, there is no evidence that Fe enters the B site. Our results correlate well with the recent results of Glazyrin et al. (2014) on Fe^{3+}- and Al^{3+}-rich perovskite.

The spin state of iron in mantle phases may significantly influence the properties and dynamics of the Earth's interior (e.g., Frost et al., 2004; Goncharov et al., 2008; Potapkin et al., 2013). In ferropericlase the high-spin (HS) to low-spin (LS) crossover in ferrous iron has been observed at pressures higher than 50 GPa (Badro et al., 2003). Reports of iron spin crossover(s) in FeAlPv in different valence states are controversial. Experimental investigations have shown that ferrous iron in FeAlPv exhibits HS-intermediate-spin (IS) crossover above ~ 35 GPa (McCammon et al., 2008; Potapkin et al., 2013). However, computational simulations find HS configuration of Fe^{2+} to be the most stable at lower mantle pressures (Hsu et al., 2012; Zhang and Oganov, 2006). Ferric iron in the A-site has been reported to remain in the HS state over all lower mantle pressures; whereas ferric iron in the B-site has been found to undergo HS-LS crossover above ~ 50 GPa (Catalli et al., 2011; Fujino et al., 2012). The latter process has been associated with the site-exchange reaction described above.

The majority of previous reports extrapolate high-pressure iron spin state data at ambient temperature to lower mantle temperatures. In McCammon et al. (2008) the temperature was limited to 1000 K and results showed the stability of IS Fe^{2+} relative to HS Fe^{2+}. In order to probe electronic configuration of iron at conditions of the deep Earth's interior we conducted a first *in situ* investigation on $Mg_{0.83}Fe_{0.20}Al_{0.06}Si_{0.92}O_3$ perovskite at pressures up to 81 GPa and temperatures up to 2000 K by means of Nuclear Forward Scattering (NFS) and Synchrotron Mössbauer Source (SMS) techniques complemented by room temperature conventional Mössbauer spectroscopic (MS) investigations.

The data measured by all three methods show the appearance of a new Fe^{2+} component assigned to the IS state at pressures above 35 GPa, similar to previous studies. The NFS data suggest the HS-IS crossover to be sharp (< 20 GPa); whereas the MS and SMS data show a more sluggish crossover that is not complete even at the highest pressure achieved in the study. The difference between previous observations appears to be due to the peculiarity of the NFS technique. NFS

spectra at very early collection times are superimposed by electronic scattering and may provide not reliable results. These early times correspond to broad lines in absorption spectra, which appear in the case of HS Fe^{2+}. No evidence of spin crossover of ferric iron in the A-site was found. After laser heating at pressures above 40 GPa, a minor component (~ 5% of the total iron content) thought to arise from LS Fe^{3+} in the B-site was observed. This low amount of iron in the B-site is below the detection limit of X-ray diffraction methods. The presence of LS Fe_B^{3+} is likely controlled by a redistribution of cation vacancies rather by the site exchange reaction between Fe^{3+} and Al^{3+}. The low amount of LS Fe^{3+} detected in FeAlPv with composition relevant to the lower mantle shows that HS-LS crossover in ferric iron plays a negligible role in determining the properties of the deep Earth.

NFS and SMS high-temperature high-pressure spectra can be fitted as a superposition of subspectra corresponding to hot and relatively cold parts of the sample, possibly arising from temperature gradients within the sample. Our data show that the high ferric iron content observed previously in quenched samples (Frost et al., 2004) is also maintained at conditions relevant to the Earth's lower mantle. Our data also show that the major fraction of ferric iron in FeAlPv remains in the HS state at conditions of the deep Earth's interior; whereas all ferrous iron in FeAlPv converts to the IS state.

III.   Pressure induced structural changes in the ammonia borane complex

The ammonia borane complex BH_3NH_3 (**AB**) is a potential candidate for hydrogen storage due its remarkably high hydrogen volume density (Stephens et al., 2007). At ambient conditions **AB** crystallizes in the tetragonal structure (space group *I4mm*) with disordered hydrogen (Bowden et al., 2007). Its high-pressure behavior has been intensively investigated during the last decade. Synthesis of dense **AB** polymorphs would imply the existence of materials with bulk hydrogen density even higher than that of the tetragonal **AB** phase. While there is general consensus regarding the phase transition from the tetragonal *I4mm* to the orthorhombic *Cmc2₁* structure near 1 GPa (e.g., Chellappa et al., 2009; Filinchuk et al., 2009), reports on phase transitions at higher pressures remain controversial (e.g., Chen et al., 2010; Kumar et al., 2010; Lin et al., 2012).

In order to investigate these phase transitions, we conducted an *in situ* high-pressure Raman spectroscopic investigation of **AB** up to 65 GPa. Our data show that **AB** behaves differently under compression at quasi-hydrostatic and non-hydrostatic conditions, which may explain the difference in observations of phase transitions below 12 GPa. Our study confirms the previously reported phase transition at ~ 12 GPa (Lin et al., 2008) and indicates a new transition at ~ 27 GPa under quasi-hydrostatic conditions.

We observed that **AB** has a nonlinear optical property, namely the capability of second harmonic generation (SHG) of laser light. The observation of the transmitted signal of SHG in the visible range was used for a development and testing of the portable laser-heating system described above, in particular for the improvement of the module for temperature measurements and for the investigation of laser beam focusing abilities.

The low scattering power of the elements constituting **AB** complicates X-ray diffraction studies of its structure, which makes any additional structural information valuable. SHG is possible only in anisotropic media without the inversion symmetry. We observed SHG during the passage of Nd:YAG (λ= 1072nm) laser light through **AB** up to 130 GPa, which suggests that the non-centrosymmetric point group symmetry is preserved in the material up to very high pressures.

Acknowledgements

I would like to deeply acknowledge my supervisors Leonid Dubrovinsky and Alexander Chumakov for their productive supervision and for the warm and friendly environment during my work with them.

The administrations of the Bayerisches Geoinstitut, the German Science Foundation (DFG), the Federal Ministry of Education and Research (BMBF), and of the European Synchrotron Radiation Facility are acknowledged for financial support of this work and providing of the necessary instrumentation and scientific facilities.

I would like to thank all my co-authors and especially Catherine McCammon, Rudolf Rüffer and Natalia Dubroviskaia for the productive discussions and suggestions regarding the manuscripts constituting this PhD thesis. I would also like to thank Stephan Übelhack, Sven Linhardt, Jean-Philippe Celse, Detlef Krausse, Leila Van Yzendoorn, Lydia Kison-Herzing, Petra Buchert, Nicole Fischer, Stefan Keyssner and Gerti Gollner for their help with the technical and administrative issues.

I would like to acknowledge my colleagues and friends for the good time we spend together and their useful advices. Particular thanks to Gleb Parakhonskiy, Innokenty and Anastasia Kantor, Valerio Cerantola, Maxim and Elena Bykovy, Clemens Prescher, Ana Černok, Konstantin Glazyrin, Natalia Solopova and Svyatoslav Shcheka.

Finally, I would like to express my gratitude to my parents Igor and Elena for providing me with good education and teaching me how to be a good person. I would also like whole-heartedly thank my wife Anna and my daughter Alisa for their support and patience.

Table of Contents

I.   Introduction

Studying materials at conditions of extreme pressure and temperature are of interest to many research fields. It helps to investigate physical properties and new phenomena in solid-state physics. It leads to discovery of new phases and compounds in chemistry and materials science. High-pressure technologies are especially valuable for geoscience because their application allows for simulating otherwise inaccessible conditions of the deep Earth's interior.

1.1   Experiments at conditions of extreme pressure and temperature

By definition pressure is a force divided by an area. Therefore, there are two principal ways to achieve high pressures: to increase a force and to reduce an area. The first approach is realized in large volume apparatuses. The most widely used of them are a piston cylinder and a multi-anvil press. A typical piston cylinder apparatus consist of a pressure vessel (bomb) and a piston, driven by a hydraulic press in a cylinder against an end load (Boyd and England, 1960). The apparatus allows samples to be heated with a resistive heater up to 3000 K. For pressure generating devices there is always a tradeoff between a sample size and the highest achievable pressure. A piston cylinder is suitable for studying samples of a ~ 15 mm^3 volume, but is limited to ~ 4 GPa. A typical multi-anvil press implements a ceramic octahedral assembly with a sample placed between eight tungsten carbide anvil cubes compressed by outer six tool-steal anvils driven by a hydraulic press (Kubo and Akaogi, 2000). A typical pressure limit is ~ 27 GPa, and a sample volume is ~ 1 mm^3. A resistive heater can be placed inside the assembly to achieve temperatures up to ~ 2500 K. The exceptional multi-anvil apparatuses can generate pressures up to 90 GPa using sintered diamonds (Zhai and Ito, 2011), but such machines are extremely rare and cannot be easy coupled to various analytical techniques.

In order to achieve ultrahigh pressures a substantial area reduction of anvils is indispensable and an appropriate anvil material should be chosen. It should be very hard, incompressible, and should not plastically deform during compression. These properties are best represented by single crystal diamonds and, therefore, the method is realized by the diamond anvil cell (DAC) technique. It allows for generating multi-megabar pressures but a sample volume is in the order of magnitude of 10^{-4} mm^3. The DAC technique is described in more details in the "methods and instruments" section. Simulations of the conditions of the Earth's interior by large volume

apparatuses are limited to the uppermost of the lower mantle. The conditions of deeper interiors can be simulated in DACs.

1.2   Temperature generation in diamond anvil cells

Generation of high temperatures in high-pressure devices is important to simulate conditions of planetary interiors. There are two main methods of high temperature generation in a DAC – external electrical resistive heating and laser heating. External resistive heating allows for routine generation of temperatures up to ~ 1100 K. The heating is very homogeneous with minor gradients in a sample chamber and can last up to several days. Measurements of the temperature are quite reliable because are monitored by thermocouples. However, several drawbacks arise at temperatures above ~ 800 K: graphitization of diamonds, pressure instability due to differences in thermal expansion coefficients of various mechanical parts of a DAC (diamonds, seats, and the body of the cell), and a number of other technical issues (Dubrovinskaia and Dubrovinsky, 2003). Operation at temperatures higher than 800 K requires an inert atmosphere for diamonds and cooling of an entire body of a DAC that significantly complicates a setup. Therefore, resistive heating in DACs is a good tool for physical and chemistry experiments at extreme conditions but is not fully suitable for *in situ* studies of materials at temperatures of the deep Earth's interior.

The technique of laser heating in DACs expands an upper limit of achievable temperature conditions to the Earth's core. But laser heating is much less homogeneous than resistive heating and leads to thermal stress and significant temperature gradients. In order to reduce the temperature gradients double-sided laser-heating systems are usually applied.

Uncertainty of temperature determination is the other disadvantage. Temperature measurements are realized by a specrtoradiometry method (Shen et al., 2010) that measures only the highest surface temperature (Campbell et al., 2007). The method is based on fitting of spectra of the emitted thermal radiation to the Planck grey body radiation function:

$$I(\lambda) = \frac{2hc^2\varepsilon}{\lambda^5(e^{\frac{hc}{\lambda kT}}-1)} \qquad (1),$$

where *I(λ)* is intensity at a given wavelength *λ*, *h* is the Planck constant, *c* is the speed of light, *ε* is emissivity, *k* is the Boltzmann constant, *T* is temperature. The grey body assumption is an approximation because emissivity of real materials is a function of wavelength and sample conditions, which introduces additional uncertainty.

The other disadvantage is inapplicability of a laser-heating technique to materials transparent in the laser spectral range. In these cases a material should be mixed with some absorber of laser radiation, which will not react with a sample during a heating process. Special sample preparation should be performed in order to provide thermal insulation between a sample and diamonds because diamonds draw of heat from a sample and prevent heating due to their extremely high thermal conductivity. Nevertheless, the technique of laser heating in DACs remains the only way of material examination statically at conditions of the deep Earth.

II.   Motivation

2.1   Portable laser-heating system for experiments with diamond anvil cells

There are numerous facilities, where the technique of laser heating in diamond anvil cells (DACs) is coupled with different analytical methods for *in situ* investigations such as Raman spectroscopy or X-ray diffraction (Boehler et al., 2008; Santoro et al., 2005), including specialized beamlines at the third-generation synchrotrons (Hirose, 2006; Prakapenka et al., 2008; Schultz et al., 2005; Shen et al., 2001).
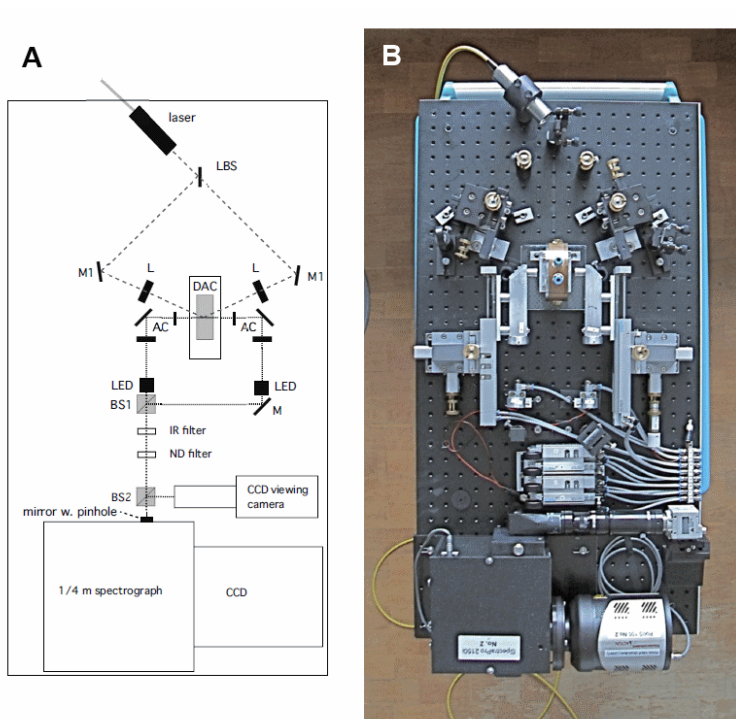
Fig. 2.1.1. Schematic of the layout (A) and photograph (B) of the portable laser-heating stand. LBS: laser beam splitter; M: mirrors; L: focusing lenses; AC: collecting achromats; DAC: diamond anvil cell; LED: light-emitting diode; BS: beam splitters; IR: infrared; ND: neutral density (Boehler et al., 2009).

Modern scientific challenges demand higher flexibility of research techniques including laser heating in DACs. Various techniques (e.g., single crystal X-Ray diffraction) require systems that can be moved or rotated during data collection. Stationary laser-heating systems are usually rather bulky, which prevent their coupling with other equipment. A system that can be easily moved between different analytical facilities, including transfer from a laboratory to a

synchrotron or between synchrotron beamlines would improve the situation and enhance scientific capabilities. As a result, since 2009 portable laser-heating systems began to emerge (Boehler et al., 2009; Dubrovinsky et al., 2009).

A portable system reported by Boehler et al. (2009) provides double-sided heating by splitting of the incoming laser beam to two equal intensity parts implementing a beam splitter cube (Fig. 2.1.1). The optical components for laser focusing and for collection of incandescent radiation are aligned separately and are optimized for their purpose and their different wavelength. The system is mounted on the 90x40 cm optical breadboard. This configuration makes the system rather large and prevents its use for single crystal X-ray diffraction studies. Moreover, the design of the system has a disadvantage: simultaneous temperature and X-ray measurements are not possible due to shadowing of an X-ray primary beam or a scattered signal by inserting optical components used for thermal radiation collection, which is unacceptable for measurements with the long data collection time because temperature may vary over a timescale of minutes during laser heating.
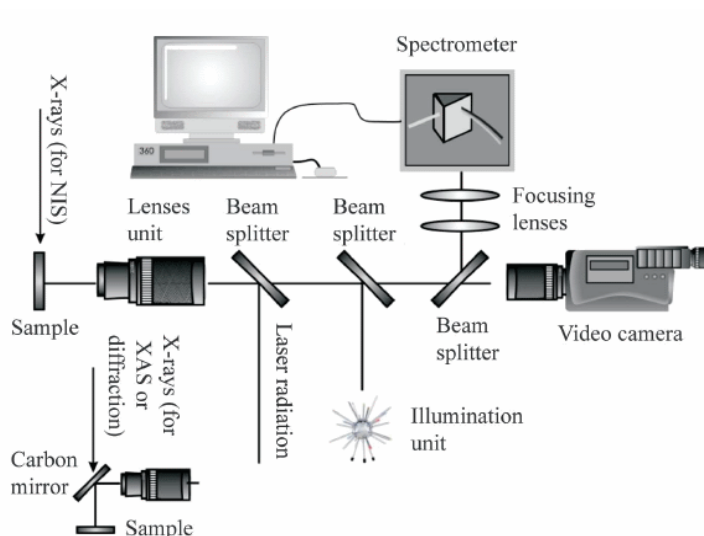
Fig. 2.1.2. Schematic diagram of the optical components of the UniHead (Dubrovinsky et al., 2009).

A system designed by Dubrovinsky et al. (2009) (Fig. 2.1.2) contains main optical components in the so-called "UniHead" – the modification of the industrial fine cutting laser head produced by Precitec KG, which allows the entire system to be placed to a common aluminum plate (30x35 cm^2). The system was successfully used for routine in-house experiments (e.g., Gu et al.,

2011; Parakhonskiy et al., 2011), *in situ* synchrotron X-ray absorption and diffraction investigations (Narygina et al., 2011), and (with some modifications) synchrotron single-crystal X-ray diffraction experiments (Dubrovinsky et al., 2010). But the system is only capable of one-sided laser heating and, thus, its application is limited to optically thin samples.

Methodological part of this thesis project was aimed to further develop the portable laser-heating setup (Dubrovinsky et al., 2009), particularly to make it double-sided, and to test it for geoscience and materials science applications.

2.2   The origin and the structure of the Earth. Fe-, Al-bearing $MgSiO_3$ perovskite at conditions of the Earth's lower mantle

Models of composition of the deep Earth's interior are based on the three main constrains: the cosmic abundances of the elements, the model of the Earth formation and evolution, and the seismic velocities observations.

The Sun and planets are believed to form from a common mass of interstellar dust and gas around 4.5 billion years ago (Anderson, 1989). The formation of the planet starts from the condensation in the cooling nebula. The accretion begins with the precipitation of highly refractory compounds, namely oxides, silicates, and titanates of Ca and Al, and refractory metals (W, Ir, Re, Os, Pt) at 1800-1400 K (Lewis, 2004). At 1400-1250 K the condensation of the major elements (Mg, Si, Fe, Ni) occurs with formation of forsterite Mg_2SiO_4, enstatite $MgSiO_3$, and Fe-Ni alloy. Moderately volatile elements such as Na and K then react with Al-bearing minerals at 1250-650 K forming alkali aluminosilicates. FeS appears at very low temperatures, less than 680 K. The ice-forming elements (C, H, O, N) condense below 300 K and the lightest elements in form of H_2 and He maintain in gaseous form. The hypothesis of the well-mixed nebula condensation deducts that the chemical composition of the Earth should have more or less the same proportion of condensable elements as the Sun and the most chemically primitive meteorites (CI chondrites) (Table 2.2.1). Both moderately volatile and highly volatile elements are depleted in the Earth relative to the Sun and CI chondrites, the more volatile they are the more depleted. This depletion is best explained by a progressive removal of the nebular gas during cooling.

The growth of the planets begins with the formation of micron-size dust particles of a condensing material (Goodman, 2000). Due to gravitational forces the initial bodies grow to form first meter-, than kilometer-, and tens-kilometer-sized planetesimals. The gravitational interactions control the further grow – large bodies are absorbing smaller and at the final stage the formation is dominated by the collisions of the Mars size objects. The high amount of the gravitational energy during accretion, especially from massive impacts is sufficient to melt (at least partially) the protoplanets. Cooling and crystallization of the planets over millions of years leads to their chemical differentiation according to the density and melting temperature. It results in forming of the radially zoned Earth with refractory and iron-rich core and silicate mantle.

Table 2.2.1. Cosmic abundances of some elements. Data from Anders & Ebihara (1982).

Element	Atoms/Si	Element	Atoms/Si
H	2.72×10^4	Si	1
He	2.18×10^3	P	0.0104
C	12.1	S	0.515
N	2.48	Ar	0.104
O	20.1	K	3.770×10^{-3}
Ne	3.76	Ca	0.0611
Na	0.0570	Cr	0.0134
Mg	1.075	Fe	0.90
Al	0.0849	Ni	0.0493

The division of the modern Earth to regions is based on the observed seismic velocities discontinuities in a radial direction (the so-called Preliminary Reference Earth Model (Dziewonski and Anderson, 1981)) (Fig. 2.2.1). The widely accepted pyrolite model, proposed by Ringwood (1962) describes the mantle as the mixture of olivine $(Mg,Fe)_2SiO_4$ and pyroxene $(Mg,Fe)SiO_3$. The seismic velocities discontinuities are caused by pressure driven phase transitions of olivine into a wadsleyite (410-km discontinuity) and ringwoodite (520-km discontinuity). The pyroxene polymorphs undergo numerous phase transformations. At moderate pressures in the presence of Al and Ca pyroxene transforms into a garnet. The traditional lower mantle starts near 660-km discontinuity (caused by a garnet-perovskite transition and decomposition of ringwoodite into $(Mg,Fe)(Si,Al)O_3$ perovskite (FeAlPv) and $(Mg,Fe)O$) and is relatively homogeneous down to about 300 km above the core-mantle boundary. Therefore, it is believed to consist of about 75% of FeAlPv, 20% of $(Mg,Fe)O$ ferropericlase, and 5% of $CaSiO_3$

perovskite. At the lowermost of the lower mantle (D'' layer) FeAlPv undergo a phase transition to the postperovskite structure (Murakami et al., 2004). Beneath the D'' layer the Earth core starts. It is apparently divided to the liquid outer core (from ~ 2900 km) and the solid inner core (from ~ 5180 km). According to the cosmic abundances, the core should mainly consist of Fe with a minor fraction of ~ 10% of Ni forming an alloy. However, some amount of light elements (C, O, H, S, Si) should also contribute to the alloy in order to obtain the densities of the core.
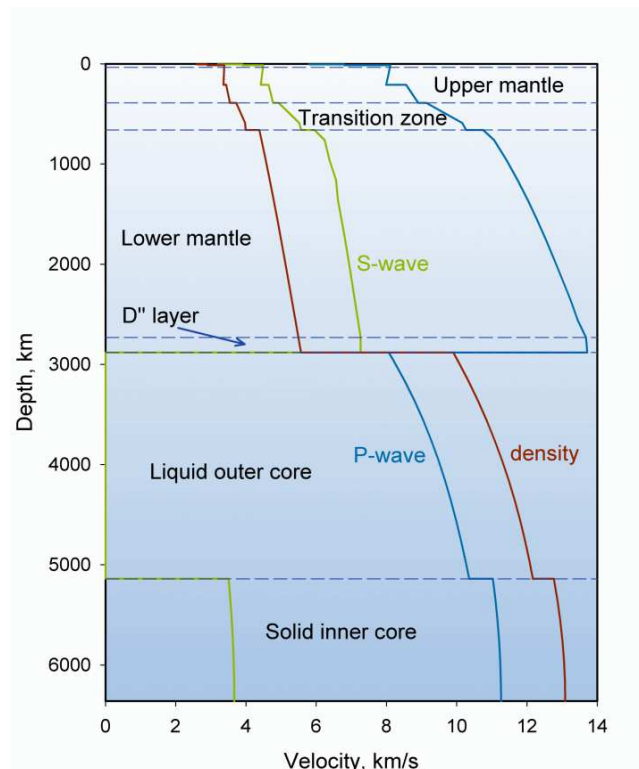
Fig. 2.2.1. Preliminary Reference Earth Model (Dziewonski and Anderson, 1981) seismic sound wave velocities and density radial profiles.

Seismological observations allow for constraining a pressure and density of the deep Earth's interior, but the temperature-depth profile is much less obvious. One of the most important reference points is an inner-outer core boundary because it separates solid and liquid iron-nickel alloys. Hence, the determination of melting temperature of the alloy at the pressure of inner-outer core boundary (~ 329 GPa) may well constrain the geotherm. This temperature determined by different methods gives a range from ~ 4900 K (Boehler, 1993) to ~ 6200 K (Anzellini et al., 2013). The range leads to temperatures from ~ 1800-1900 K at the uppermost of the lower mantle to 2200-2500 K close to the core-mantle boundary.

The exact Fe content in the mantle minerals is not well known (Fiquet et al., 2008). Average composition of chondrites allows for constraining the iron content in form of both Fe^{2+} and Fe^{3+} by ~ 10 mol. % (Sturhahn, 2005). Computations by generalized inverse method gives a total iron content in the lower mantle of 10 ± 6 mol. % for a pyrolite model (Mattern et al., 2005).

High pressures relevant for the lower mantle may cause a redistribution of the *3d* electrons of iron and result in spin-pairing crossover. Both ferrous and ferric iron may be presented in one of the three possible spin states – high-spin (HS), intermediate-spin (IS), and low-spin (LS) – depending on the relative magnitudes of the crystal field splitting and spin pairing energy (Fig. 2.2.2).
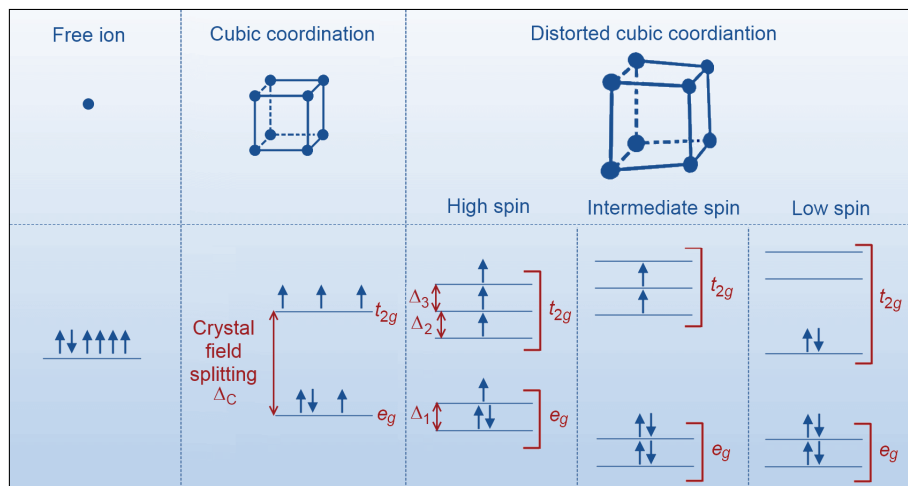
Fig. 2.2.2. Representative energy diagram of Fe^{2+} in different coordination and possible spin configurations. The splitting showed for a cubic coordination represents also dodecahedral and tetrahedral coordination. $\Delta_{1,2,3}$ are the splitting of the e_g and t_{2g} energy levels due to the Jahn-Teller distortion. Modified after Burns (1993).

It was found that iron in (Mg,Fe)O undergo HS-LS crossover at lower mantle pressures (Badro et al., 2003). But the spin state of iron in FeAlPv is still a matter of debates. The spin state of iron in mantle minerals may strongly influence the properties of the Earth's interior. For example Badro et al. (2004) proposed that spin crossover of Fe^{2+} in FeAlPv increases the transparency of the mantle in the infrared region and, thus, increases the radiative thermal conductivity; Ohta et al. (2007) observed an increase of the electrical conductivity of (Mg,Fe)O at the pressures corresponding to HS-LS crossover.

Iron can occurs in both ferrous and ferric forms in FeAlPv and may occupy one of the two perovskite sites – a large distorted 8-12-coordinated dodecahedral site, hereafter referred to as A, and a smaller relatively undistorted octahedral site, hereafter referred to as B (Fig. 2.2.3). While it is well accepted that Fe^{2+} occupies exclusively the A-site, the site occupancy of Fe^{3+} is still under debate. Ferric iron has been observed to occupy either exclusively the A-site (McCammon et al., 2008; Potapkin et al., 2013) or both the A- and B-sites (Badro et al., 2004; Catalli et al., 2011, 2010; Hummer and Fei, 2012). Several studies have additionally predicted an exchange of Fe^{3+} from the A- to B-site at high pressures (Catalli et al., 2011, 2010; Fujino et al., 2012). In order to refine the site occupancy of iron at conditions of the lower mantle additionally to measurements of its spin and electronic state by various techniques (X-ray emission, Nuclear Forward Scattering, conventional Mössbauer spectroscopy, etc.), a single crystal X-ray diffraction experiment is required. It was not possible to conduct an experiment of this type at conditions corresponding to the Earth's lower mantle without implementing a setup that allows an entire laser-heating system with a DAC to be rotated during data collection.

Numerous studies have been performed in order to identify the iron spin state in FeAlPv, but with conflicting results. Some studies conclude that Fe^{3+}_A undergoes HS-LS crossover (Jackson, 2005; Li et al., 2006), although the majority of studies do not report spin crossover in Fe^{3+}_A (Catalli et al., 2011, 2010; Fujino et al., 2012; Lin et al., 2012; McCammon et al., 2008; Potapkin et al., 2013). Meanwhile there is a common view that Fe^{3+}_B undergoes HS-LS crossover at mantle pressures in studies where Fe^{3+} is believed to occupy the-B site (Catalli et al., 2011, 2010; Fujino et al., 2012; Lin et al., 2012). There is also general consensus that Fe^{2+} undergoes a dramatic change at mantle pressures through the appearance of a new component with extremely high quadrupole splitting in Mössbauer spectra at high pressure (reviewed by McCammon et al., 2013), even though there are conflicting interpretations of this change: HS-IS crossover (Lin et al., 2008; McCammon et al., 2010, 2008; Potapkin et al., 2013), or a structural modification of the local environment (Lin et al., 2012). Moreover, most predictions of FeAlPv behavior at lower mantle conditions have been inferred by extrapolation of high-pressure data measured at ambient temperature or from ab initio calculations.
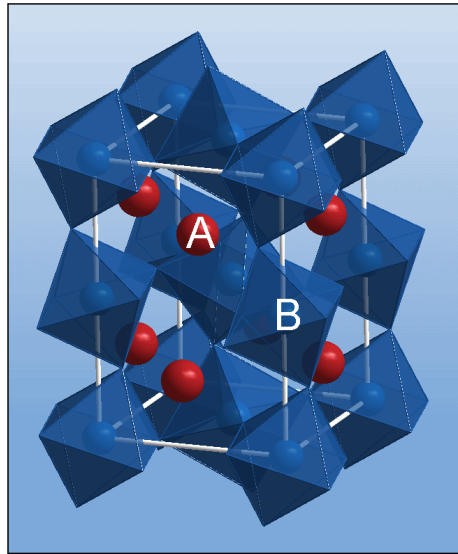
Fig. 2.2.3. Crystal structure of (Mg,Fe)(Si,Al)O$_3$ perovskite. The dodecahedral A-site is occupied by Mg and Fe. The octahedral B-site is mainly occupied by Si and Al.

Geophysical part of this thesis project was aimed to couple single crystal X-ray diffraction and Mössbauer spectroscopy techniques with the technique of laser heating in DACs in order to probe *in situ* the site occupancy and electronic configuration of iron in FeAlPv at conditions of the deep Earth's interior.

2.3   High-pressure phases of the ammonia borane complex

The ammonia borane complex (**AB**) is a possible candidate for hydrogen storage due to its remarkably high gravimetric (19.6 wt % H) and volumetric (145 gH L^{-1}) hydrogen content (Blaquiere et al., 2008; Stephens et al., 2007). At ambient conditions **AB** is a soft white powder. It crystallizes in the hydrogen disordered tetragonal *I4mm* structure. Numerous studies have been performed in order to investigate high-pressure phases of **AB**, but with controversial results. In a number of previous studies phase transitions in **AB** have been recognized by pressure dependence of Raman spectra and has been observed near 1 GPa (Chellappa et al., 2009; Custelcean and Dreger, 2003; Lin et al., 2008; Nylén et al., 2009; Xie et al., 2009), at 5 GPa (Chellappa et al., 2009; Lin et al., 2008; Nylén et al., 2009; Xie et al., 2009), at 8 GPa (Xie et al., 2009), at 10 GPa (Chellappa et al., 2009; Xie et al., 2009), and at 12 GPa (Lin et al., 2008). The

phase transition at 1 GPa has been in detail investigated using X-Ray diffraction (Chen et al., 2010; Filinchuk et al., 2009; Kumar et al., 2010; Lin et al., 2012) and thermal conductivity measurements (Andersson et al., 2011) and is identified as a disorder-order phase transition from the tetragonal *I4mm* to the orthorhombic *Cmc2$_1$* structure. Meanwhile there is no consensus regarding behavior of **AB** on compression based on X-Ray diffraction data. Filinchuk et al. (2009) have not observed further transitions up to 12 GPa, while Kumar et al. (2010) have suggested one more transition to the triclinic *P1* structure around 8 GPa with no further transitions up to 27 GPa. Chen et al. (2010) have observed a phase transition at 5 GPa and no transformations have been detected upon compression up to 23 GPa. High-pressure phases possibly are much denser then the ambient pressure one and thus have much higher hydrogen volume density. An investigation of the stability field of high-pressure phases and knowledge regarding their structures may give a hint for synthesis of new hydrogen-rich compound(s). It can be very useful in a future design of a storage medium for hydrogen.

The materials science part of this thesis project was aimed to conduct a high-pressure Raman study of **AB** in order to determine its phase transitions and to complement the study by the investigation of the nonlinear interaction of **AB** with laser radiation.

2.4   Summary of the aims of the thesis project

- Methodological part of this thesis project was aimed to further develope the portable laser-heating setup (Dubrovinsky et al., 2009), particularly to make it double-sided, and to test it for geoscience and materials science applications.

- Geophysical part of this thesis project was aimed to couple single crystal X-ray diffraction and Mössbauer spectroscopy techniques with the technique of laser heating in DACs in order to probe in situ the site occupancy and electronic configuration of iron in FeAlPv at conditions of the deep Earth's interior.

- The materials science part of this thesis project was aimed to conduct a high-pressure Raman study of **AB** in order to determine its phase transitions and to complement the study by the investigation of the nonlinear interaction of **AB** with laser radiation.

III. Methods and instruments

3.1 High-pressure experiments

3.1.1 Diamond anvil cells

The diamond anvil cell (DAC) technique was introduced in the late 50th (Weir et al., 1959). The basic principle is to squeeze a material between two perfectly aligned culets of the gem quality diamonds (Fig. 3.1.1.1). One of the most valuable characteristics of the DAC technique is transparency of anvils to a wide range of electromagnetic radiation. That allows for *in situ* studying of pressurized samples using different absorption, scattering, and emission methods.
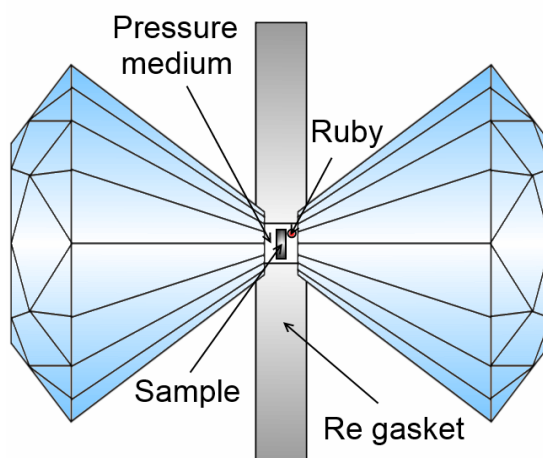
Fig. 3.1.1.1. Schematic diagram of diamond anvil cell loading.

The process of cell assemblage starts with gluing of bases of a pair of gem quality diamonds to hard-metal seats, which transmit load from the cell body to the diamonds. The seats are fixed to the metallic driven parts of the DAC. Force can be applied in several ways, but the most common DACs are mechanical screw driven and membrane cells. The membrane allows for pressure adjusting without disturbing the cell, which is an important advantage for synchrotron researches. But this type of cells is not well suitable for high-temperature experiments due to thermal expansion of gas in the membrane, which complicates pressure control. For the current work piston-cylinder type BX90 mechanical DACs (Kantor et al., 2012) (Fig. 3.1.1.2) were used because they provide better stability at high temperatures and are easier to prepare and operate compared to the other types of DACs.

Fig. 3.1.1.2. Photographs of a BX90 diamond anvil cell.

The maximum pressure that can be achieved in a DAC is defined by the culets' size of the diamonds. This experimental work was aimed for studying materials at lower mantle pressures; therefore, diamonds with 250 µm culets were used, which may achieve a pressure up to 90 GPa. For the correct application two diamonds should be strictly coaxial and perfectly aligned against each other. Tilt between the diamonds leads to an achievable pressure reduction and may result in sample loss or diamonds destruction. Typically a 200 μm thick Re gasket was pre-indented to about 30 μm thick and a 125 μm hole was drilled in the centre as a pressure chamber where a sample was placed with or without pressure medium. Re gaskets have good mechanical properties and contain no iron that is critical for Mössbauer spectroscopic experiments.

3.1.2   Loading of pressure transmitting media

A DAC design causes non-uniform stress. The stress is uniaxial perpendicular to a surface of diamond culets and thus produces non-homogenous strain. Pressure can be considered as a thermodynamic parameter only if a sample is surrounded by hydrostatic media (liquid or gas). Moreover, non-uniform stress leads to destruction of single crystal samples and thus is inapplicable for experiments with single crystals. In order to avoid these problems and to achieve quasi-hydrostatic conditions a special pressure transmitting media are used. The best choices are noble gases: He, Ne, Ar; they crystallize at relatively high pressure and remain quasi-hydrostatic even after crystallization due to relatively low yield strength. For the current work Ne or He as pressure transmitting media were used. He provides better hydrostatic conditions, but during high-temperature experiments it starts to diffuse intensively through diamonds, which usually leads to sample loss or diamonds destruction. A sufficient amount of gases cannot be loaded into

a DAC at ambient conditions. Argon, nitrogen, and some other gases can be loaded by cryogenic liquefying, but for neon and helium special high-pressure "bombs" are used. A cell at ambient pressure is placed inside the device and the entire "bomb" is pumped with gas afterwards. After this the DAC should be pressurized in order to trap the gas inside the DAC's pressure chamber and the remaining gas from the "bomb" should be released. For the current work the gas loading system (Kurnosov et al., 2008) designed in the Bayerisches Geoinstitut (BGI) was used for loadings.

3.1.3 Measurements of the pressure

Determination of the pressure is a crucial point in any DAC experiment. Usually methods based on calibrants loaded in a pressure chamber together with a sample are used. Equations of states of many materials are well known and, therefore, pressure can be derived from diffraction patterns during diffraction experiments. For this purpose phases with the cubic symmetry and simple structures are preferable in order to minimize a number of diffraction lines and, thus, to avoid an overlapping of reflections from a sample and a pressure standard. For the X-ray diffraction experiments of the current work a pressure was determined from the Ne equation of state (Fei et al., 2007).

If diffraction is unavailable or inconvenient two main techniques are widely used: ruby fluorescence spectroscopy and Raman spectroscopy of a diamond cullet. A ruby fluorescence method is a rapid and easy way to measure a pressure. It is a secondary pressure calibration scale – the pressure dependence of the wavelength λ of the Al_2O_3:Cr^{3+} R_1 peak (Fig. 3.1.3.1) was obtained based on shock wave equations of states of metals (Mao et al., 1986). The pressure can be derived from the equation:

$$P(GPa) = \frac{A}{B}\left[\left(\frac{\lambda}{\lambda_0}\right)^B - 1\right] \qquad (2),$$

where λ is a measured wavelength of the peak and λ_0 is a wavelength of the peak at ambient pressure, A=1905, B=5 for non-hydrostatic conditions and B=7.665 for quasi-hydrostatic conditions. For the current work commercially available ruby spheres several microns in diameter were used. For correct pressure measurements the spheres should not be bridged between diamonds because highly non-uniform stress results in distortion of the spectrum.

31
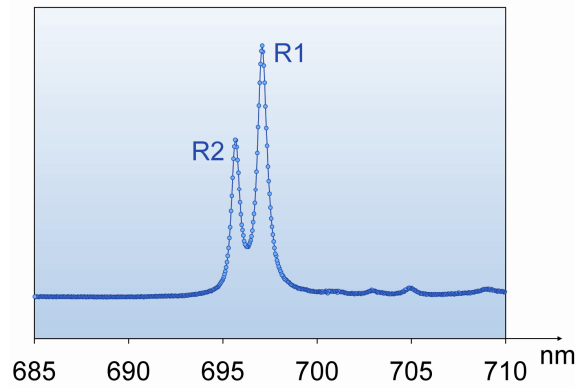
Fig. 3.1.3.1. Ruby fluorescence spectra.

Pressure measurements by a ruby fluorescence method are limited to ~ 100 GPa due to broadening and weakening of the R_1 peak. Therefore, for experiments above megabar pressure dependence of the first order Raman mode of a diamond cullet is used (Fig. 3.1.3.2). The high-wavenumber edge of the Raman band is correlated with normal stress of the culet face (Akahama and Kawamura, 2006). Quasihydrostatic pressure can be derived from the equation

$$P(GPa) = K_0 \left(\frac{\Delta v}{v_0}\right) \left[1 + \frac{1}{2}(K_0' - 1)\left(\frac{\Delta v}{v_0}\right)\right] \qquad (3),$$

where Δv is a measured wavenumber of the high-frequency edge and v_0 is the edge frequency at ambient pressure, K_0=547 GPa, K_0'=3.75. A position of the high-wavenumber edge is defined as a minimum of a first derivative of the spectrum (inset in Fig. 3.1.3.2).
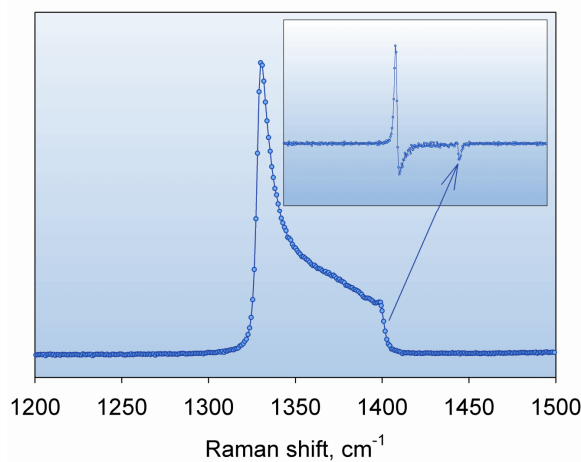
Fig. 3.1.3.2. Typical Raman spectrum from the centre of a diamond cullet. The inset shows a first derivative of the spectrum used for the correct determination of the high-wavenumber edge.

32

### 3.1.4 Laser-heating system for diamond anvil cells

High-temperature data presented in the current work were obtained using a double-sided portable laser-heating system that was developed during this Ph. D. project. Detailed description of the system is presented in the Chapter 5.1.

3.2 Mössbauer spectroscopy

3.2.1 Basic principles

In order to comply the momentum conservation law when a free nucleus emits a γ-quantum it must recoil because the emitted quantum with the energy E has the momentum p=E/c (where c is the speed of light). The recoil takes energy and thus the energy of the emitted quantum is smaller than that of the γ-transition by $\Delta_r E = p^2/2M$ (where M is the mass of the atom). The same energy is transferred to a free nucleus during absorption. Therefore, absorption and emission lines of the γ-transition are shifted by $2\Delta_r E$. This value is much greater than the natural linewidth Γ_0 of the γ-transition (for the ^{57}Fe nuclei $\Gamma_0 = 4.6 \times 10^{-9}$ eV and $\Delta_r E = 2 \times 10^{-3}$ eV) (e.g., Greenwood & Gibb, 1971). In 1958 Rudolf Mössbauer (Mössbauer, 1958) discovered that by placing emitting and absorbing nuclei in a crystal, one can use the crystal lattice for recoil, decreasing the recoil energy loss. In this case emission and absorption lines overlap. It allows resonance absorption of the γ-quanta to be observed.

For a typical Mössbauer spectroscopy experiment a source material differs from an absorber material under study. The nuclear radius in the excited state is different than that in the ground state $R_e \neq R_g$. The electronic densities are mainly set up by all s-electrons (1s, 2s, 3s, etc.) of the electronic shells and are different for the nuclei of the source and the absorber $\rho_S \neq \rho_A$. Therefore, electric monopole interactions are different in the source and the absorber and affect the nuclear ground and excited state levels to a different extent. This leads to the measured isomer shift (Fig. 3.2.1.1) (Greenwood and Gibb, 1971):

$$\delta = \Delta E_A - \Delta E_S = \frac{2}{3}\pi Z e^2 (\rho_A - \rho_S)\left(R_e^2 - R_g^2\right) \qquad (4),$$

where ΔE_S and ΔE_A are energy differences between the excited and ground states of a source material and an absorber material consequently. The monopole interaction does not change degeneracy of the energy levels and, therefore, does not cause splitting of the absorption lines

(Fig. 3.2.1.1). The second component that contributes to the shift between the emission and the absorption lines is a second-order Doppler shift that is related to the vibration of the atom on its lattice site

$$\frac{\Delta_{SOD}E}{E} = -\frac{\langle v^2 \rangle}{2c^2} \qquad (5),$$

where v is a velocity of the atom. It depends on Debye temperature and absolute temperature of the solid. In a single Mössbauer spectrum it is impossible to separate contributions of the isomer shift and second-order Doppler shift, so one always operates with a sum of both called a centre shift (CS).The CS varies for different valence and spin states and for different coordination numbers of ^{57}Fe (Fig. 3.2.1.2).
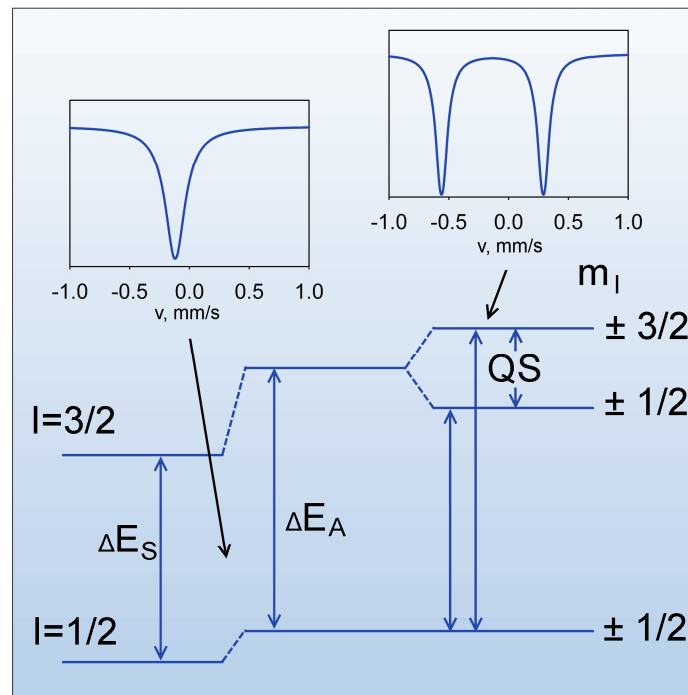
Fig. 3.2.1.1. The diagram of the ^{57}Fe nuclear energy splitting due to isomer shift and quadrupole splitting (QS) and corresponding absorption spectra.

Any nucleus with a spin quantum number of greater than I=1/2 has non-spherical charge distribution and thus possesses quadrupole moment eQ. This core quadrupole moment interacts with the electrical field gradients, which are caused by deviation from the spherical symmetry in

the electronic environments of the nucleus, and splits the degenerate I=3/2 level into two sub-levels with magnetic spin quantum numbers $m_I = \pm 3/2$ and $\pm 1/2$ (Fig. 3.2.1.1). There are two sources that can contribute to the total electrical field gradients: a lattice contribution that is produced by electrons of ligands around the Mössbauer central atom and a valence contribution that is the product of the electrons in the valence orbitals of the Mössbauer atom. The electric quadrupole splitting gives information on the oxidation state, the spin state, and the local symmetry of the Mössbauer atom and in a general case depends on pressure and temperature.
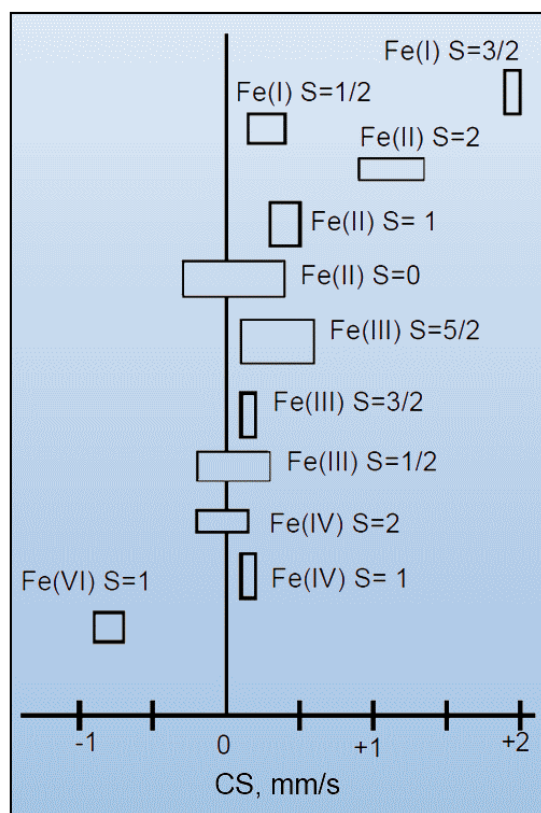
Fig. 3.2.1.2. An overview of the centre shift (CS) of different Fe-compounds with various oxidation states relative to α-Fe. S is a bulk spin number. Modified after Greenwood & Gibb (1971).

The Zeeman Effect between the magnetic moment of the nucleus and the magnetic field at the nuclear site leads to a further splitting of the nuclear levels to 6 non-equivalent sub-levels. The corresponding absorption spectrum comprise of the six lines. In this work I did not study materials with magnetic interactions and, hence, do not discuss this subject further.

3.2.2 Radioactive Mössbauer source

Conventional Mössbauer sources implement the fact that the decay of the majority of radioactive nuclides produces usually highly excited daughter nuclei. These can decay to the ground state by emission of γ-quanta. The exited state of ^{57}Fe in the Mössbauer sources in BGI is performed by the decay of ^{57}Co isotope: ^{57}Co+e^{1-}→^{57}Fe. The ^{57}Co isotope has sufficient activity and approximately 9 month half-life, which makes experiments and source operation relatively convenient and simple. For experiments with DAC it is required a highly collimated source due to a small size of the samples. For this reasons the 370 MBq ^{57}Co high specific activity source in a 12 µm thick Rh matrix with active dimensions of 500 µm x 500 µm was used.
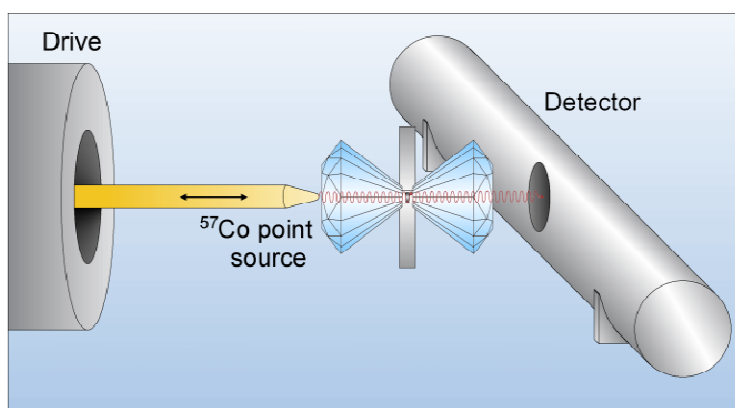
Fig. 3.2.2.1. Schematic diagram of a high-pressure Mössbauer experiment.

As mentioned above the emission and absorption lines should overlap with high precision in order to obtain absorption spectra. It is usually not the case because an exact energy of the lines depends on the valence and spin states, as well as on the crystallographic environment of the nucleus. In order to make the lines overlapping Doppler modulation is usually used. A source is mounted to a velocity drive (Fig. 3.2.2.1) and is accelerated through a range of velocities in order to produce a Doppler effect and scan the gamma ray energy through a given range. A typical range of velocities for ^{57}Fe may be ±5-15 mm/s (1 mm/s = 48.075 neV). An absorption spectrum is collected by a gas-proportional detector. For the current work materials enriched in ^{57}Fe were used in order to decrease the collection time, which typically was 3-4 days per spectrum for experiments with DACs. The spectra were fitted using a full transmission integral with a normalized Lorentzian source lineshape using the MossA software package (Prescher et al., 2012).

3.2.3 Nuclear Forward Scattering

Conventional Mössbauer spectroscopy is not well suited for studying samples with dimensions less than ~ 100 µm, which is the case for experiments with DACs. Low brilliance of sources results in a long measuring time, which excludes *in situ* laser heating of samples and, thus, limits temperature to a maximum of about 800 K available by resistively heated DACs. The alternative is the time domain Nuclear Forward Scattering (NFS) technique that allows a beam to be focused to ~ 10 µm in diameter and drastically reduces collection time. After a prompt pulse of non-resonant radiation a delayed signal of nuclear scattering is measured as a function of time. The synchrotron pulse excites all nuclear resonance sub-levels simultaneously. A time pattern in forward direction (Fig. 3.2.3.2b) arises from the interference of radiation components with different energies. A quantum beat period is determined by the splitting, therefore, by the hyperfine field (Fig. 3.2.3.3). For the current work NFS data were collected at the Nuclear Resonance beamline ID18 (Rüffer and Chumakov, 1996) (Fig. 3.2.3.1) at the European Synchrotron Radiation Facility (ESRF) during operation in 4-bunch mode, which provides a time window of 704.24 ns. The spectra were collected over 10-60 min each. The spectra were fitted using the CONUSS package (Sturhahn, 2000).
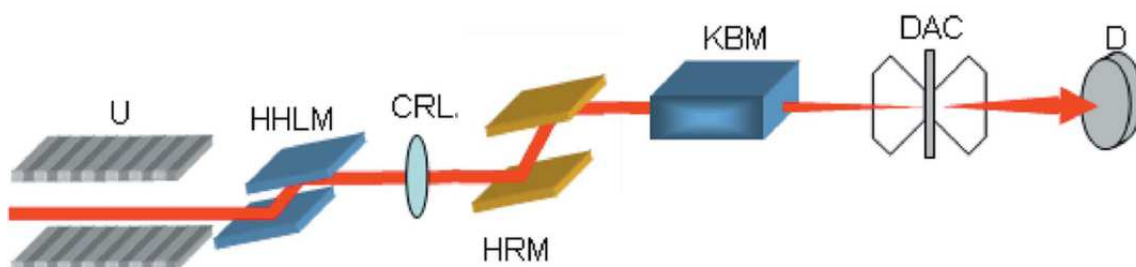

Fig. 3.2.3.1. Optical scheme for a high-pressure experiment with DACs using the Nuclear Forward Scattering technique. U: undulator; HHLM: high-heat-load monochromator; CRL: compound refractive lens; HRM: high-resolution monochromator; KBM: Kirkpatrick-Baez mirrors; DAC: diamond anvil cell; D: avalanche photodiode detector. Modified after Potapkin et al. (2012).
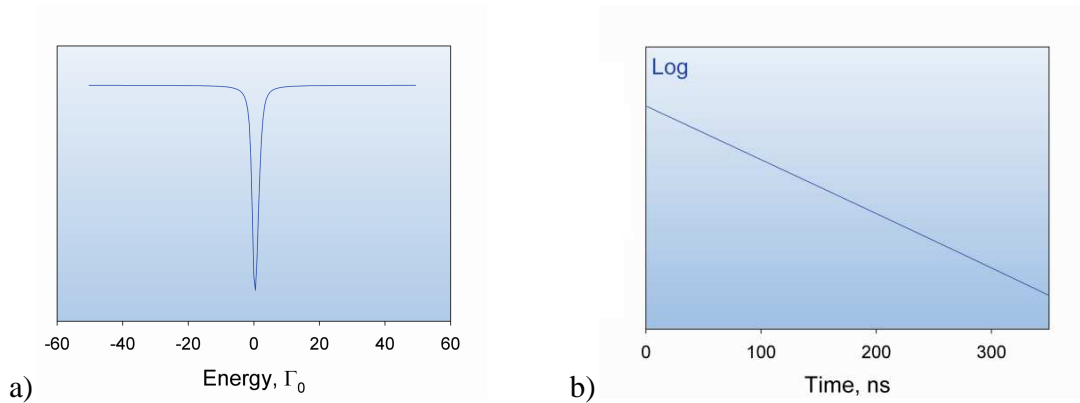
Fig. 3.2.3.2. A Mössbauer single line absorption spectrum (a) and a corresponding Nuclear Forward Scattering spectrum (b).
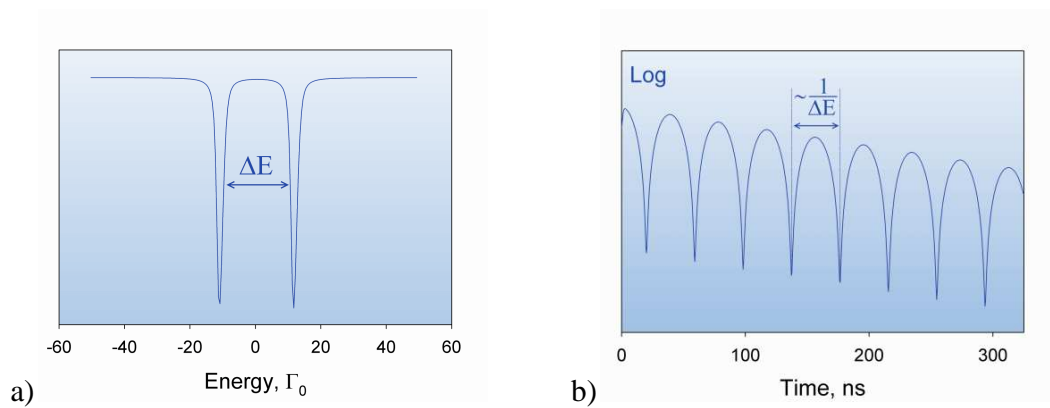
Fig. 3.2.3.3. A Mössbauer quadrupole absorption spectrum (a) and a corresponding Nuclear Forward Scattering spectrum (b).

3.2.4 Synchrotron Mössbauer Source

NFS technique is not well suited to study materials with a large number of spectral components (which is the case for Fe-, Al-bearing magnesium silicate perovskite) due to complexity of spectra and non-uniqueness of fitting models. In order to avoid these drawbacks a recently developed at beamline ID18 at the ESRF Synchrotron Mössbauer Source (SMS) (Potapkin et al., 2012) was used in order to perform energy domain Mössbauer spectroscopy at pressure-temperature conditions relevant to the lower mantle. Optical scheme for a high-pressure experiment with DACs using the SMS is presented on Fig. 3.2.4.1. The key element of the source that provides neV resolution is the iron borate $^{57}FeBO_3$ single crystal enriched in the ^{57}Fe isotope up to 95%, grown by Kotrbová et al. (1985). In this crystal all (NNN) reflections with

odd N (i.e. (111), (333), etc.) are forbidden for electronic diffraction, while they are allowed for nuclear diffraction because of a specific polarization factor of nuclear resonant scattering in the presence of hyperfine interactions (Smirnov et al., 1969). These reflections are employed to extract nuclear scattering radiation. In the presence of hyperfine splitting of the nuclear levels the crystal functions as a multi-line nuclear radiator. Such a source is obviously not convenient for spectroscopic studies. Yet a special case of combined magnetic dipole and electric quadrupole interactions can be realized in iron borate close to its Neel temperature in the presence of a weak external magnetic field, where a single-line spectrum of emitted radiation can be obtained (Smirnov et al., 1997). The energy width of the emitted line is close to the natural linewidth of the Mössbauer resonance. The SMS gives the possibility to focus a beam to tens of micrometers and thus to collect spectra within the laser-heated spot. For the current work the typical time for one measurement was 2-3 hours depending on the sample. The spectra were fitted using a full transmission integral with a normalized Lorentzian-squared source lineshape using the MossA software package (Prescher et al., 2012).
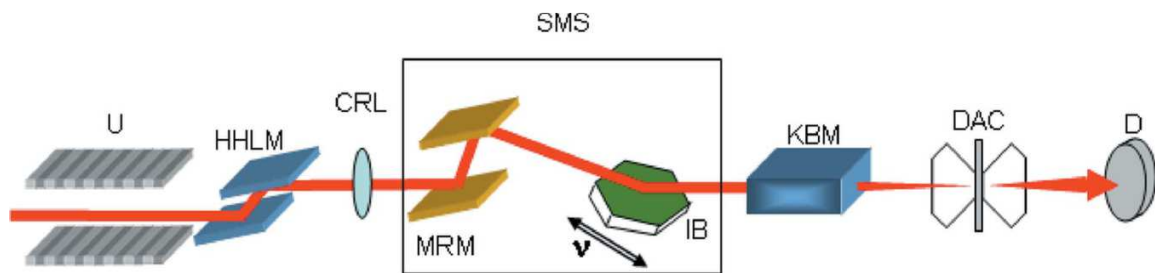
Fig. 3.2.4.1. Optical scheme for a high-pressure experiment with DACs using the Synchrotron Mössbauer Source (SMS). U: undulator; HHLM: high-heat-load monochromator; CRL: compound refractive lens; MRM: medium-resolution monochromator; IB: iron borate crystal; KBM: Kirkpatrick-Baez mirrors; DAC: diamond anvil cell; D: avalanche photodiode detector (Potapkin et al., 2012).

3.3   X-ray diffraction

Since its discovery X-ray diffraction is the most important and powerful tool for structure determination. X-ray diffraction may be described as a reflection on lattice planes. Angles of X-ray reflections are used to determine size and shape of a unit cell using the Bragg equation $2d \times \sin\theta = n\lambda$ (d is a distance between lattice planes, θ is an incident angle of the beam, λ is a wavelength of X-ray radiation) (Fig. 3.3.1). Intensity of reflections allows the content of a unit

cell to be derived because various atoms in a structure contribute to a different extend to the intensity of the diffracted beam. A measure of the scattering amplitude by an isolated atom is called the scattering factor Since the scattering is essentially due to the interactions with the electron shell of the atoms, the scattering factor is the higher the heavier the atom is. The scattering factor decreases with scattering angle due to destructive interference between beams diffracted at different parts of the electron shell.
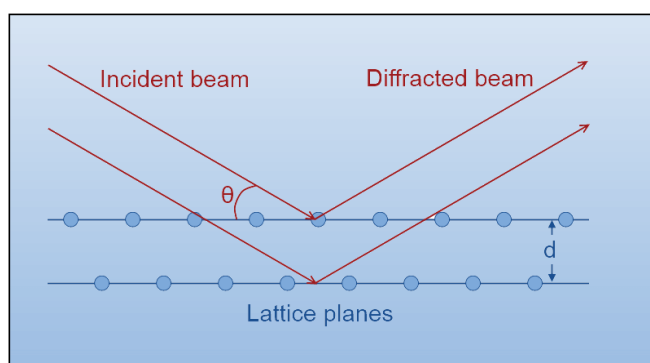
Fig. 3.3.1. Basic principle of X-ray diffraction.

Synchrotron radiation has several advantages relative to conventional X-ray sources. From the Bragg equation one can see that the shorter is the wavelength the greater is the number of reflections that can be observed. This is crucial for DAC experiments because the opening angle of a DAC is usually very limited. Intensity of the synchrotron X-ray beam is several orders of magnitude higher compared to X-ray tubes and, therefore, data collection goes much faster. The beam can be focused to a micron-size. Altogether it allows for coupling of the synchrotron X-ray diffraction technique with *in situ* laser heating in DACs. For the current work the diffraction data was collected at the High Pressure Station of the White Beam beamline ID09a (Häuserma and Hanfland, 1996) at the ESRF. The data were processed using the Crysalis software (Oxford Diffraction (2006) Crysalis RED, version 1.171.31.8. Oxford Diffraction Ltd., Abingdon, Oxfordshire). Crystal structure refinements of integrated intensities have been carried out with the SHELXL-97 WinGX version (Farrugia, 1999; Sheldrick, 2008).

3.4   Raman spectroscopy

Raman spectroscopy is a non destructive technique for observation of vibrational, rotational, and other low-frequency modes in materials (Bowley et al., 1990). It is based on inelastic scattering

of incident monochromatic radiation, usually from a laser. Laser radiation may scatter from a lattice with no interaction with phonons (Rayleigh scattering) or may excite (Stokes Raman scattering) or absorb (anti-Stokes Raman scattering) phonon (Fig. 3.4.1). Intensity ratios of Stokes and anti-Stokes Raman lines are determined by Boltzmann's law and, therefore, at ambient temperature anti-Stokes lines are appreciably less intense than the corresponding Stokes lines. For this reason, only the Stokes part of a spectrum is generally used.

For the current work Raman spectroscopy was performed by exciting Raman modes using the 514.5 nm Ar^{3+} ion laser in order to avoid overlapping of ruby fluorescence and Raman lines. The scattered radiation was collected in a backscattering geometry and analysed by a T64000 system (Dilor XY) with a liquid nitrogen cooled CCD detector. A 1800 groove/mm grating was used with a final resolution of 0.6 cm^{-1}.
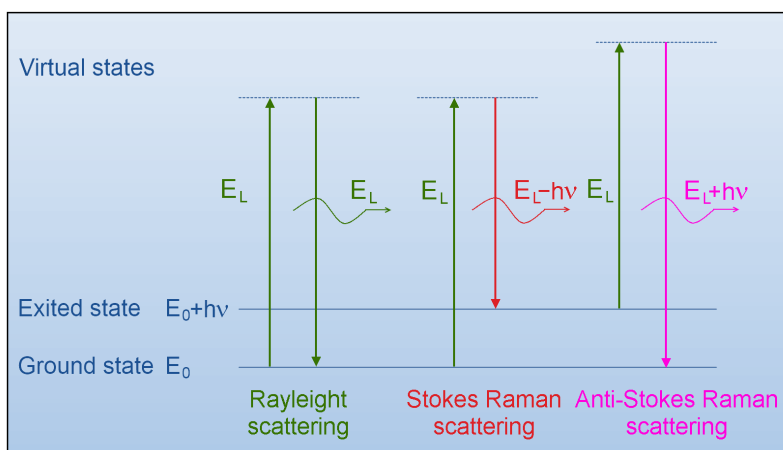

Fig. 3.4.1. Scattering process scheme. E_L is incident laser energy; $h\nu$ is phonon energy.

IV. Scope of the thesis

This part summarizes the results presented in Chapter 5, which have been published or submitted in peer-review journals. Subsection 4.1 describes the design and testing of a portable double-sided laser-heating system and its application to structural studies of silicate perovskites at conditions of the Earth's lower mantle. Subsections 4.2 and 4.3 describe a study of the spin state of iron in silicate perovskite in different valence and electronic states at high pressures and temperatures using the Nuclear Forward Scattering and Synchrotron Mössbauer Source techniques, respectively. The last subsection 4.4 describes a study of high-pressure behavior of the ammonia borane complex and illustrates application of the portable laser-heating setup to a research oriented on materials science. All four manuscripts have been written by me as a first author and I have actively participated in the experiments preparation, data collection, and data analyzes.

4.1 Design of the portable double-sided laser-heating system for experiments with diamond anvil cells

The main aim of this PhD project was a further development of a portable laser-heating setup (Dubrovinsky et al., 2009), particularly making it double-sided, and its testing for geoscience and materials science applications. The system should be compatible with different analytical techniques (first of all with X-ray diffraction and nuclear resonance spectroscopy), easily transferable between the laboratory and synchrotron facilities, or between synchrotron beamlines.

The laser-heating system consists of two main components – sources of laser light and the universal laser-heating heads (UniHeads). As the laser source two SPI modulated fiber lasers are used with a maximum output power of 50 W and 100 W (the excitation wavelength is 1071 nm). The lasers can be operated in continuous or pulse modes with a pulse frequency up to 100 kHz. The lasers require no water cooling and use only a standard electrical plug (100-240 V AC, 2 A at 230 V).

The UniHeads are based on the fine cutting laser heads (Precitec KG) and their functions in the laser-heating system are:

- Focusing incoming laser radiation on a sample within a diamond anvil cell (DAC)
- Providing high-magnification imaging of a sample and its illumination
- Collecting thermal radiation from a sample for temperature measurements

The main optical components of the laser-heating system are presented on the Fig. 4.1.1.
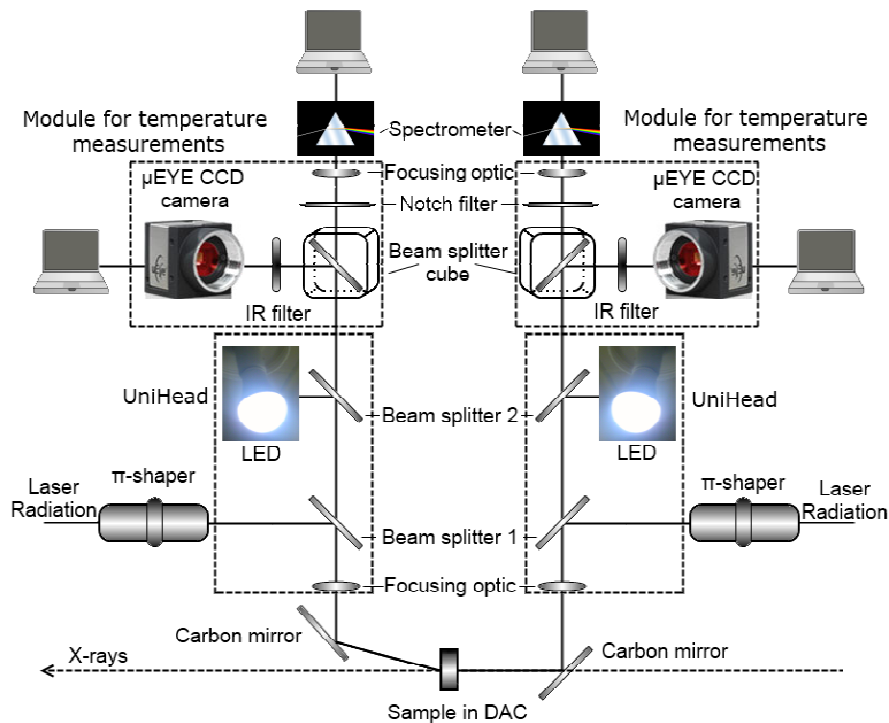
Fig. 4.1.1. Schematic diagram of the optical components of the laser-heating system.

The output of the lasers is collected by π-shapers (Prakapenka et al., 2008) in order to convert the original laser beam with a Gaussian shape intensity distribution to flat top distribution, with ~ 50 µm full width at half maximum (FWHM), for more homogeneous heating. In order to make the laser beam and the incident X-ray beam coaxial carbon mirrors with a 100 nm silver coating (produced at Bayreuth University) mounted at ~ 45° angles to optical axes of the UniHeads are employed.

A sample is illuminated with light emitting diodes built into the UniHeads. Both of the UniHeads are equipped with modules for *in situ* temperature measurements and visual observation. The module incorporates a focusing lens projecting the central part of the heated spot onto the end of an optical fiber, a µEYE[TM] CCD camera, and a beam splitter cube. In order to prevent saturation

of the cameras by reflected laser radiation infrared filters are employed. The measurements of a temperature are performed with a multi-wavelength specrtroradiometry method (Shen et al., 2010), i.e., by fitting of the thermal radiation in a given wavelength range (usually 600 to 850 nm) to the Planck radiation function. For our experiments an Ocean Optics QE65000 spectrometer or an Acton SP2300 spectrometer (Princeton Instruments) with a PIXIS400 CCD detector were used. In order to prevent the incidence of laser radiation into the detectors 1064 nm notch filters are employed.
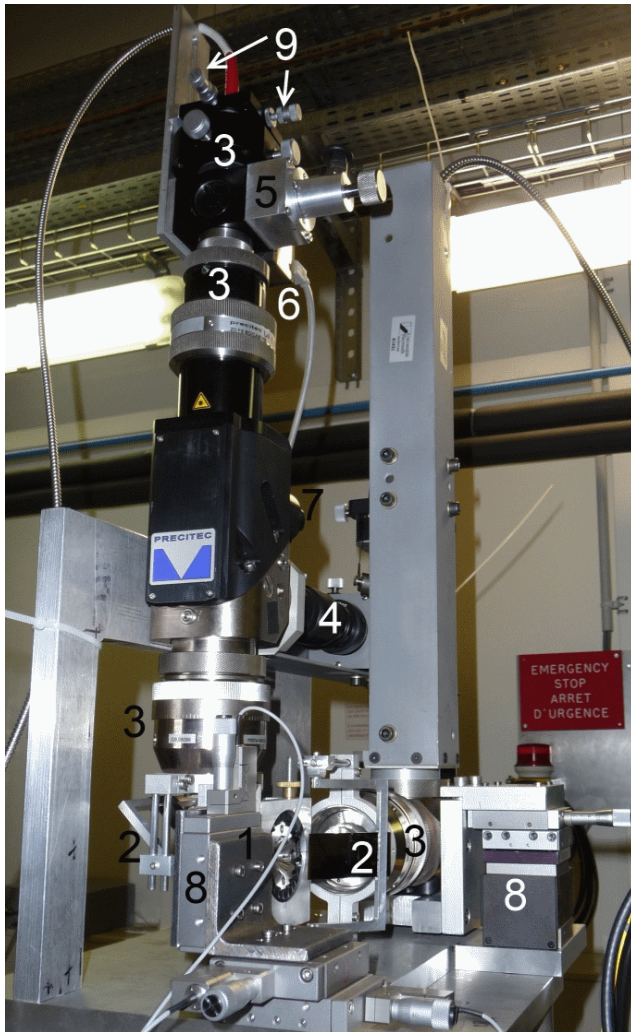
Fig. 4.1.2. Photograph of the double-sided portable laser-heating system mounted for experiments at ESRF beamline ID18. 1: holder with a diamond anvil cell; 2: carbon mirrors; 3: focusing optics; 4: π-shaper; 5: beam-splitter cube; 6: CCD camera; 7: LED; 8: 3-axis translation stages; 9: adjustable screws for spectrometer focusing.

All parts of the system (except the laser source) are mounted on a common aluminum plate (0.35x0.30 m^2, and thickness 15 mm). A typical setup is shown on the Fig. 4.1.2. The plate with the assembled and pre-aligned system can be transferred in an ordinary passenger car as a single

unit. The complete installation of the system from the beginning and its alignment requires two to three hours.

For the first test of the setup a Synchrotron Mössbauer Source (SMS) study of $Fe_{0.2}Mg_{0.8}O$ was selected, since its Mössbauer spectra at high pressure and temperatures up to about 800 K are already known from a previous work using externally heated DACs (Kantor et al., 2009). The sample was compressed to ~ 29 GPa in a DAC and then laser-heated. Upon one-sided laser heating with a 50 µm focused laser beam (or during double-sided heating with poor alignment of the X-ray beam with respect to the laser beams) the spectra showed a superposition of the subspectra corresponding to a relatively cold and hot material, caused by temperature inhomogeneities in the sample. Double-sided heating with the correct alignment of the X-ray beam and the laser spot resulted in homogeneous heating. Temperature gradients also arose from double-sided laser heating of thick samples (above ~ 20 µm thickness), when the interior of the sample remained colder than the surface.

Using our novel setup we also conducted an *in situ* high-pressure, high-temperature single crystal X-ray diffraction investigation of Fe-, Al-bearing magnesium silicate perovskite (FeAlPv) in order to refine the site occupancy of iron and to test the possibility of an experiment that requires rotation of the system as a single unit. Single crystals of $(Mg_{0.87}Fe^{3+}_{0.09}Fe^{2+}_{0.04})(Si_{0.89}Al_{0.11})O_3$ perovskite were loaded into a DAC along with Ne as pressure-transmitting medium and compressed. We collected the diffraction data at pressures between 65 and 78 GPa (where pressure was determined from the Ne thermal equation of state (Fei et al., 2007)) in several sets, namely before, during, and after laser heating at 1750(50) K. We found that (a) the refined amount of iron in the A-site coincided within uncertainty of our measurements with the value determined from the electron microprobe data, (b) laser heating did not affect the chemical composition of FeAlPv in our experiments, and (c) high temperature did not promote any chemical exchange reactions between the A- and B- perovskite structural sites.

4.2 Nuclear Forward Scattering and conventional Mössbauer study of Fe-, Al-bearing magnesium silicate perovskite at lower mantle conditions

We conducted a first *in situ* Nuclear Forward Scattering (NFS) study of FeAlPv with composition $Mg_{0.83}Fe_{0.21}Al_{0.06}Si_{0.91}O_3$ at pressure and temperature conditions of the Earth's

lower mantle. The study was complemented by NFS and conventional Mössbauer spectroscopy (MS) measurements at high pressure and ambient temperature.

Fig. 4.2.1. Effect of pressure on the hyperfine parameters of $Mg_{0.83}Fe_{0.21}Al_{0.06}Si_{0.91}O_3$ perovskite as measured by Mössbauer spectroscopy (MS) and nuclear forward scattering (NFS): (a) Centre shift (CS); (b) Quadrupole splitting (QS); (c) Relative abundance. Green and red curves indicate the trends of the relative abundance for the Fe^{2+} high-spin (HS) low QS and Fe^{2+} intermediate-spin (IS) components, respectively, while the dashed and solid curves indicate the trends for the MS and NFS data, respectively. For clarity the relative abundance of the Fe^{3+} and HS high QS Fe^{2+} components are not shown, which remain relatively constant at all pressures at values of 20% and 10%, respectively.

The pre-synthesized in a multi-anvil apparatus and well characterized sample of FeAlPv was loaded into a DAC along with Ne as pressure-transmitting medium. Room temperature NFS spectra were collected upon compression up to 81 GPa. Additionally at 43, 63, and 81 GPa the sample was laser heated at 1200-2000 K and spectra were collected during laser heating. MS spectra of the FeAlPv sample were collected up to 72 GPa at room temperature.

The low-pressure spectra are fitted to three doublets, one assigned to high-spin (HS) Fe^{3+} and two assigned to HS Fe^{2+}, according to their hyperfine parameters (Fig. 4.2.1). This assignment

46

provides good fits and self-consistent interpretation, although a later SMS study showed that this model have to be corrected (see Chapter 4.3). At pressures above 37 GPa a new component attributed to intermediate-spin (IS) Fe^{2+} appears and its relative abundance grows with pressure at the expense of the dominant HS Fe^{2+} doublet (low quadrupole splitting (QS) component). The second HS Fe^{2+} (high QS component) and HS Fe^{3+} doublets do not undergo any dramatic changes, only the pressure driven increase of the QS and decrease of the centre shift (CS). NFS data show that HS-IS crossover in Fe^{2+} completes entirely at the 35-55 GPa pressure range, while MS data show that HS Fe^{2+} and IS Fe^{2+} have comparable relative abundances up to the highest pressure achieved in the current study (Fig. 4.2.1). We attributed this difference to the well focused nature of a synchrotron beam that significantly reduces pressure gradients in the radial direction. A later SMS study showed that the difference had been caused not by pressure gradients but by the fundamental peculiarity of the NFS technique (see the Chapter 4.3). We observe no evidence of Fe^{3+} spin crossover.
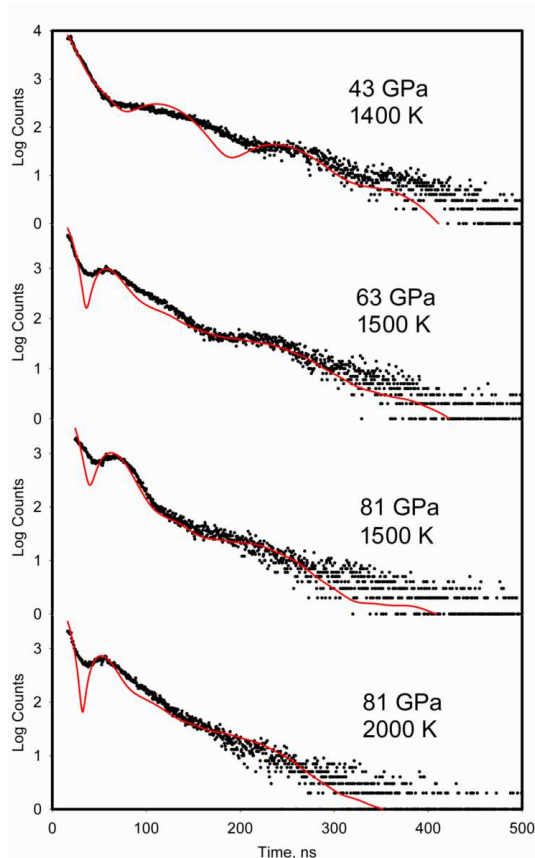

Fig. 4.2.2. High-pressure Nuclear Forward Scattering spectra of $Mg_{0.83}Fe_{0.21}Al_{0.06}Si_{0.91}O_3$ perovskite at high temperature. The solid lines show the theoretical fits.

The high-temperature data (Fig. 4.2.2) were fitted with two QS-interactions attributed to Fe^{2+} and Fe^{3+}, according to their relative abundances. The derived hyperfine parameters show that Fe^{3+} remains in the HS state and Fe^{2+} is in the IS state, according to the trends in CS and QS temperature behavior of both components and previously shown stabilization of IS Fe^{2+} relative to HS Fe^{2+} at high temperatures. We attributed the misfits seen on Fig. 4.2.2 to small deviations in pressure and temperature, but a model that diminished these misfits was created only after a treatment of the SMS high-temperature data (see the Chapter 4.3).

4.3   Oxidation state of the lower mantle: *in situ* observations of the iron electronic configuration in magnesium silicate perovskite at extreme conditions

Despite numerous NFS studies (Catalli et al., 2011, 2010; Jackson, 2005; Li et al., 2006; Lin et al., 2012; McCammon et al., 2010, 2008; Chapter 4.2) significant controversies remain about high-pressure evolution of the iron electronic state in FeAlPv. There are several components contributing to Mössbauer spectra of FeAlPv, arising from multiple sites, valence states and spin states, which leads to spectral complexity and, therefore, to non-uniqueness of fitting models. Energy domain MS is a more definitive method that allows different components contributions to be distinguished. Therefore, we conducted an energy domain SMS study of the sample from the same synthesis run as reported in Chapter 4.2.

The sample of FeAlPv was loaded into a DAC along with Ne as pressure-transmitting medium. Room temperature SMS spectra were collected at pressures between 12 and 77 GPa. At each pressure step above 39 GPa the sample was laser heated at ~ 2000 K (measured by a spectroradiometry method) and spectra were collected before, during, and after heating.

At low pressure and ambient temperature the spectra consist of two main absorption features with a shoulder in between that can be fitted with two doublets (Fig. 4.3.1) that correspond to HS Fe^{2+} and HS Fe^{3+}, according to their hyperfine parameters. Upon pressure increase a new doublet begins to emerge above ~ 40 GPa and becomes well resolved above 52 GPa (Fig. 4.3.1). The doublet has extremely high QS. It is similar to the component observed in previous studies (McCammon et al., 2008; Potapkin et al., 2013), and is attributed to IS Fe^{2+}, consistent with all previous experimental data (XES, NFS, MS) (e.g., Jackson, 2005; Li et al., 2004; Lin et al.,

2012; Narygina et al., 2010). Upon pressure increase abundance of the IS component grows at the expense of the doublet corresponding to HS Fe^{2+}. After heating of the sample at ~ 40 GPa and ~ 2000 K a doublet with a very narrow linewidth (FWHM ~ 0.1 mm/s), a relatively low CS ~ –0.2 mm/s, and QS ~ 0.9 mm/s is observed (Fig. 4.3.1). The CS of the new narrow doublet remains almost unchanged at pressures up to 77 GPa. Relative abundance of the component in all our experiments remained below ~ 5%, and its first appearance at 40 GPa and slight increase of intensity upon re-heating of the sample at higher pressures correlate clearly with a decrease of the abundance of the HS Fe^{3+} component by a similar amount.

At high temperatures CS values of Mössbauer components provide a novel possibility of an internal thermometer to probe mean temperature of a sample independently of the spectroradiometry measurements. The high-temperature spectra show a superposition of components that can be modeled as absorption arising from hotter and cooler (hereafter referred to as "warm") material (Fig. 4.3.2). The "warm" components of the spectra consist of the same components as at ambient temperature: two doublets corresponding to Fe^{2+} (low QS and high QS) and one Fe^{3+} doublet. The hot components of the spectra consist of two doublets, which can be assigned to Fe^{2+} and Fe^{3+}. All of the experimental data available from XES, NFS and MS methods are consistent with assignment of the ferrous component at high temperatures to IS Fe^{2+}.

We associate the new low CS doublet at ambient temperature spectra with a partial shift of ferric iron into the B-site (Fe_B^{3+}). Rapid saturation of the change of the abundance of Fe_B^{3+} with increasing pressure suggest that the occupation of the B-site by ferric iron is controlled by the number of defects arising from synthesis of the sample at 26 GPa, rather as the result of by an exchange reaction involving Al^{3+} (Catalli et al., 2011; Fujino et al., 2012). We note that high-pressure high-temperature single crystal X-ray diffraction studies of FeAlPv (Dubrovinsky et al., 2010; Glazyrin et al., 2014; Chapter 4.1) firmly exclude the presence of Al on the A-site, while a few percents of Fe on the B-site would be hardly detectable by X-ray diffraction methods. Our data show that Fe_B^{3+} is in the low-spin (LS) already at about 40 GPa and its amount does not increase upon heating. We see no evidence of a spin change involving Fe_A^{3+}, neither at high pressures nor at high temperatures. We, therefore, conclude that HS-LS crossover in Fe^{3+} plays a negligible role in determining the properties of the deep Earth, while at the same time changes in

the type and distribution of vacancies (e.g., in the A- and B-sites) in FeAlPv may significantly influence elastic properties of the material and geochemistry of the Earth's lower mantle, in particular its upper part.
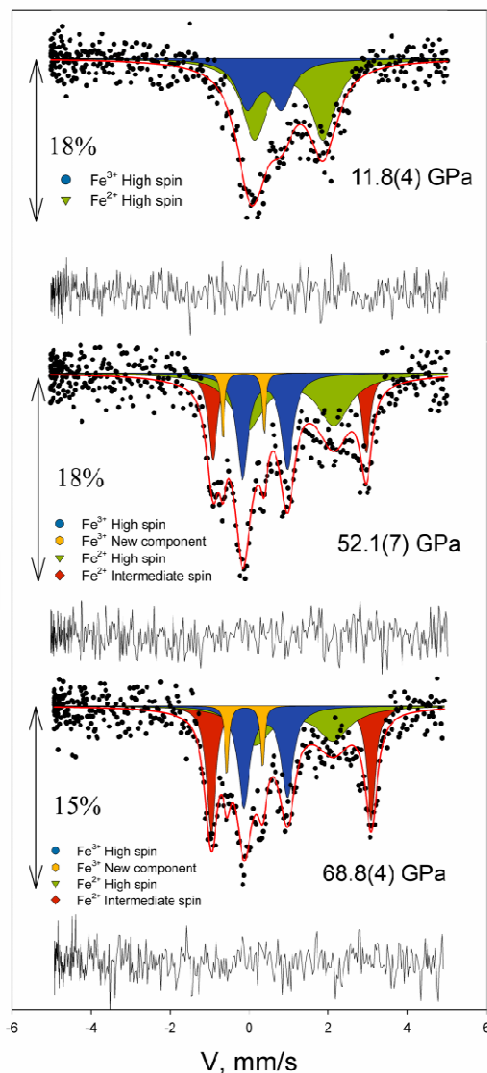
Fig. 4.3.1. Selected high-pressure SMS spectra of $Mg_{0.83}Fe_{0.21}Al_{0.06}Si_{0.92}O_3$ perovskite at room temperature. The solid lines show the theoretical fit, the arrows show the amount of absorption, and the residual is indicated below each spectrum. After 39 GPa the sample was laser heated at ~ 2000 K at each pressure step.

The SMS data enable a reevaluation of NFS data collected on a similar sample at similar conditions (Chapter 4.2). Both the conventional MS and NFS data from Chapter 4.2 can be fitted with the model proposed in the current chapter. Notably, the refitted NFS spectra also confirm

additional low CS component with about 5% abundance. In Chapter 4.2 we attributed the differences of the NFS and MS Fe^{2+} spin crossover pressure ranges (Fig 4.2.1) to pressure gradients inside the DAC. SMS data were collected at the same conditions as NFS data on the same beamline and therefore should show similar results; however, SMS data indicate a much broader pressure range for HS-IS crossover. In the time domain representation the FWHM of the
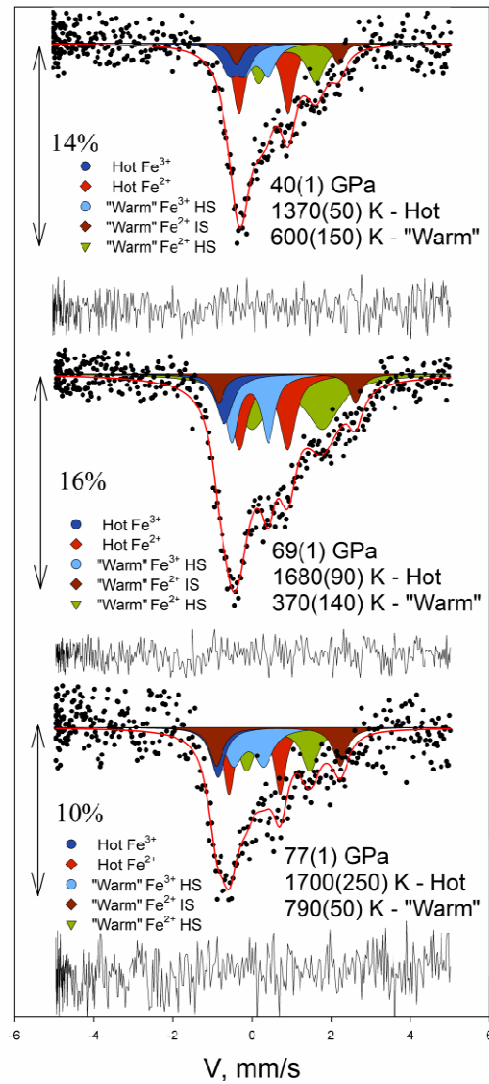
Fig. 4.3.2. Selected high-pressure SMS spectra of $Mg_{0.83}Fe_{0.21}Al_{0.06}Si_{0.92}O_3$ perovskite at high temperature. The solid lines show the theoretical fit, the arrows show the amount of absorption, and the residual is indicated below each spectrum. Due to nonhomogeneous heating the spectra show a superposition of absorption data arising from hotter and cooler (referred to as "warm") material. Temperatures were determined from the centre shift values. HS: high-spin; IS: intermediate-spin.

corresponding lines in absorption spectra determines the decay rate of the corresponding beats. A time window of NFS spectra is gated to exclude electronic scattering of a synchrotron X-ray beam, which appear at early time of the spectra and, therefore, cuts off the initial part of the quantum beats. The FWHM of the HS Fe^{2+} component is the highest among the all components of FeAlPv (Fig. 4.3.1) and its main contribution should therefore appear in a gated region. The FWHM of the HS Fe^{2+} doublet increases with pressure, which amplifies the effect. As a result, the component cannot be detected (or is difficult to detect) at high pressures. Our results show the disadvantage of the NFS technique for studies of multi-component systems with a high dispersion of component linewidths. The NFS high-temperature data presented in the Chapter 4.2 show only a limited number of spectral features and, therefore, the unique fit is not possible. We observe that the five-doublet fit reported in the current chapter significantly improves the quality of the NFS high temperature fits.

Our *in situ* measurements at pressures up to ~ 80 GPa and temperatures above 1700 K have unambiguously established the valence and spin states of iron in FeAlPv at lower mantle conditions. Our data confirm the conclusions based on the studies of quenched samples that a large proportion of iron in the lower mantle is in the ferric state (Frost et al., 2004; McCammon, 2005, 1997).

4.4   High-pressure investigation of BH₃NH₃

Although the main purpose of the designed laser-heating setup is to generate high temperatures, the other properties of laser radiation can be used in researches.

We investigated high-pressure behavior of the ammonia borane complex (**AB**) by means of Raman spectroscopy. Observed pressure induced changes of the lattice modes (Fig. 4.4.1), the B-H and N-H rocking deformation modes (Fig. 4.4.2), and the N-H-stretching modes (Fig. 4.4.3) allow us to infer two phase transitions: at ~ 10 and ~ 26 GPa. Raman modes of molecular solids under pressure blue shift because the corresponding chemical bonds stiffen as a result of compression. In **AB** the modes in the N-H-stretching region are red shifting with pressure (Fig. 4.4.3), which indicates strengthening of the B-H···H-N dihydrogen bonding accompanied by weakening of the N-H bond.
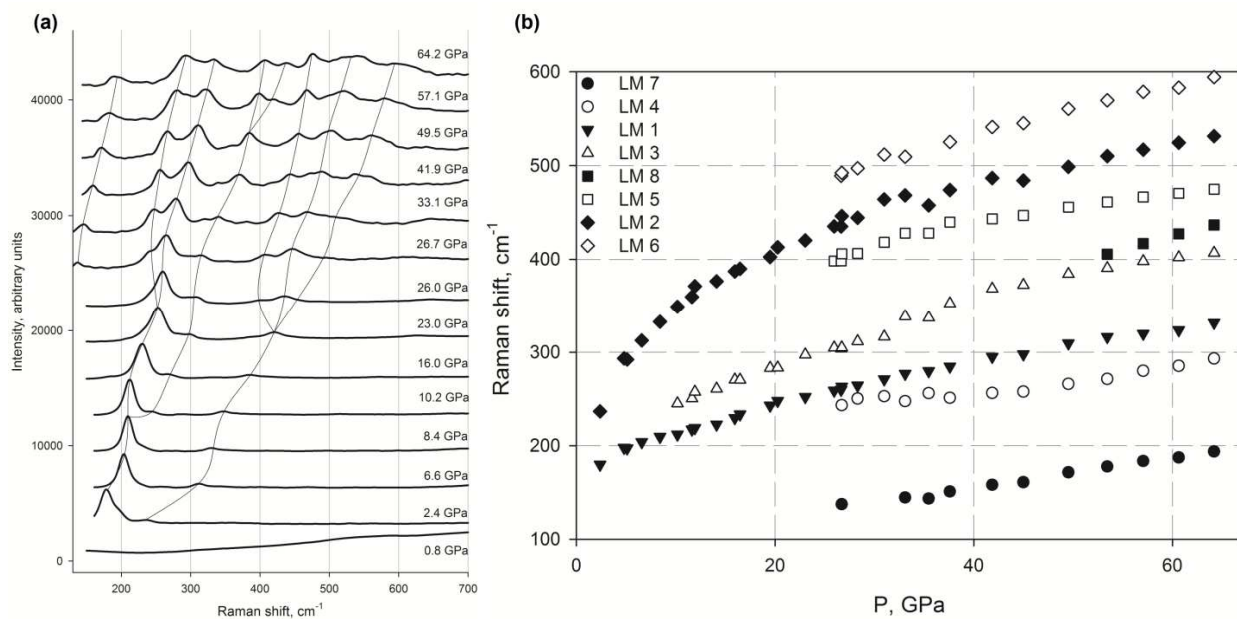
Fig. 4.4.1. Raman spectra of ammonia borane shown in the lattice vibration region (a) and the Raman frequency shift of the lattice modes (LM) as a function of pressure (b).
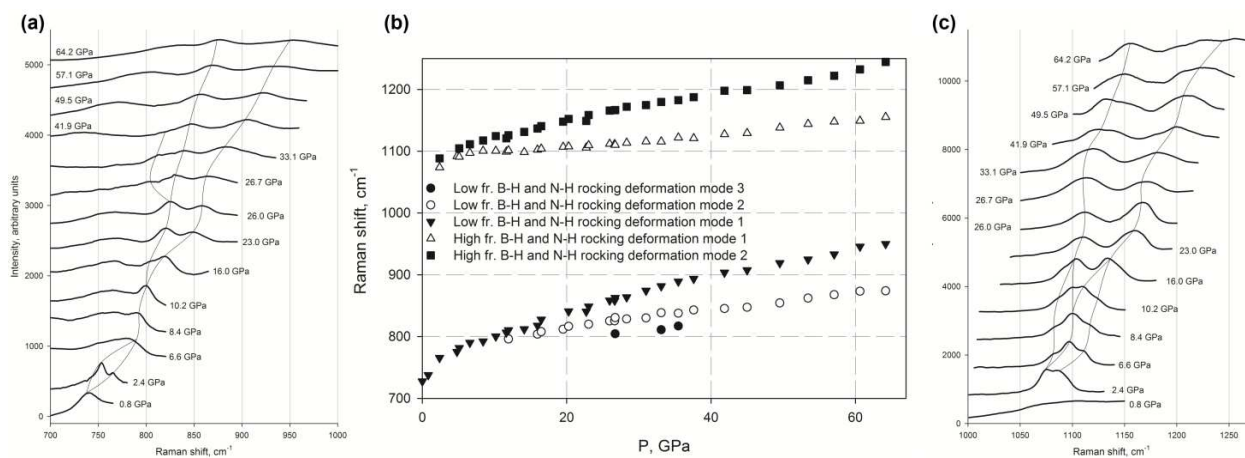
Fig. 4.4.2. Raman spectra of ammonia borane shown in the B-H and N-H rocking deformation region (a,c) and the Raman frequency shift of the corresponding modes as a function of pressure (b).

X-ray studies of the **AB** crystal structure are complicated by the low scattering power of its constituting elements. That is why any additional information about the symmetry of high-pressure phase(s) is valuable. We realized that **AB** has nonlinear optical properties, namely the capability of second harmonic generation of laser light. The system reported in Chapter 4.1 was used to observe the generation of second harmonic (λ=535.5 nm) during the passage of laser

radiation (λ=1071nm) through the **AB** sample at pressures up to 130 GPa (Fig. 4.4.4). Second harmonic generation is possible only in anisotropic media without the inversion symmetry. Our observations allow for inferring that regardless of phase transformations **AB** remains as the non-centrosymmetric structure up to at least 130 GPa.
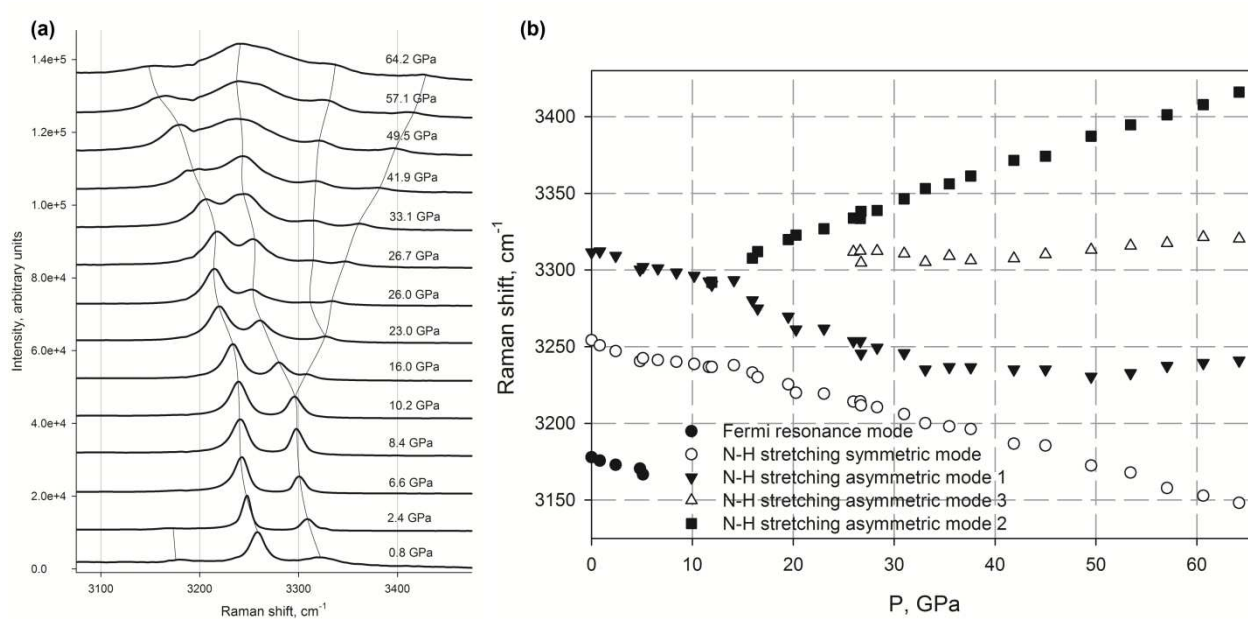

Fig. 4.4.3. Raman spectra of ammonia borane shown in the N-H stretching region (a) and the Raman frequency shift of the corresponding modes as a function of pressure (b).
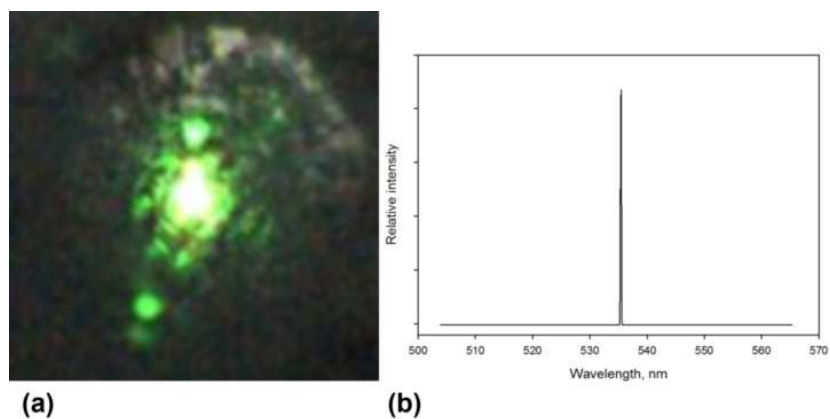

Fig. 4.4.4. Photograph showing green light generated upon irradiation of ammonia borane by 1071 nm laser radiation at 130 GPa (a); the spectrum of the corresponding generated second harmonic (b).

54

4.5   List of manuscripts and statement of author's contribution

[1]   Kupenko, I. (IK), Dubrovinsky, L. (LD), Dubrovinskaia, N. (ND), McCammon, C. (CM), Glazyrin, K. (KG), Bykova, E. (EB), Boffa Ballaran, T. (TB), Sinmyo, R. (RS), Chumakov, A.I. (AC), Potapkin, V. (VP), Kantor, A. (AK), Rüffer, R. (RR), Hafland, M.(MH), Crichton, W. (WC), Merlini, M. (MM) (2012). Portable double-sided laser-heating system for Mössbauer spectroscopy and X-ray diffraction experiments at synchrotron facilities with diamond anvil cells. Review of Scientific Instruments, 83(12), 124501.

The methodology described in the paper was developed by IK with technical help by LD, KG, and ND. The single crystal diffraction data were collected and analyzed by EB, IK, KG, and LD. The Synchrotron Mössbauer Source spectra were collected and analyzed by VP, IK, and CM. All authors were involved in the data discussion. IK did a final assessment of the results and wrote the manuscript with help of other co-authors. The total contribution of IK is 70%.

[2]   Kupenko, I. (IK), McCammon, C. (CM), Sinmyo, R. (RS), Prescher, C. (CP), Chumakov, A. I., (AC) Kantor, A. (AK), Rüffer, R. (RR), Dubrovinsky, L. (LD) (2014). Electronic spin state of Fe,Al-containing $MgSiO_3$ perovskite at lower mantle conditions. Lithos, 189, 167–172.

The samples were synthesized by RS and characterized by IK, RS, and CM. The conventional Mössbauer spectra were collected by IK. The Nuclear Forwards Scattering spectra were collected by IK with help and assistance by AK, RS, CP, AC, RR, CM, and LD. All spectra were analyzed by IK. Interpretation of results and writing of the manuscript were carried out by IK with help of CM, LD, and other co-authors. The total contribution of IK is 80%.

[3]   Kupenko, I. (IK), McCammon, C. (CM), Sinmyo. R. (RS), Cerantola V. (VC), Potapkin V. (VP), Chumakov A.I. (AC), Kantor, A. (AK), Rüffer, R. (RR), Dubrovinsky, L. (LD). (2014). Oxidation state of the lower mantle: in situ observations of the iron electronic configuration in magnesium silicate perovskite at extreme conditions. Earth and Planetary Science Letters, submitted.

The samples were synthesized by RS and characterized by IK, RS, and CM. The Synchrotron Mössbauer Source spectra were collected by IK with help and assistance by VC, AK, VP, AC, RR, and LD. All spectra were analyzed by IK. Interpretation of results and writing of the

manuscript were done by IK with help of CM, LD and other co-authors. The total contribution of IK is 80%.

[4]   Kupenko, I. (IK), Dubrovinsky, L. (LD), Dmitriev, V. (VD), Dubrovinskaia, N. (ND) (2012). *In situ* Raman spectroscopic study of the pressure induced structural changes in ammonia borane. The Journal of Chemical Physics, 137, 074506.

The Raman spectra and Second Harmonic Generation spectra were collected and analyzed by IK. All authors were involved in the data interpretation and writing of the manuscript. The total contribution of IK is 85%.

V.   Results

5.1   Portable Double-Sided Laser-Heating System for Mössbauer Spectroscopy and X-ray Diffraction Experiments at Synchrotron Facilities with Diamond Anvil Cells

I. Kupenko[1,3], L. Dubrovinsky[1], N. Dubrovinskaia [2], C.McCammon[1], K. Glazyrin[1], E. Bykova[2], T. Boffa Ballaran[1], R. Sinmyo[1], A.I.Chumakov[3], V.Potapkin[1,3], A. Kantor[1,3], R.Rüffer[3], M. Hanfland[3], W. Crichton[3], M. Merlini[4]

[1]*Bayerisches Geoinstitut Universität Bayreuth D-95440 Bayreuth, Germany*

[2]*Material Physics and Technology at Extreme Conditions, Laboratory of Crystallography, University of Bayreuth, D-95440 Bayreuth, Germany*

[3]*European Synchrotron Radiation Facility, BP 220, F-38043 Grenoble, France*

[4]*Dipartimento di Scienze della Terra, Università degli Studi di Milano, Via Botticelli 23, 20133 Milano (Italy)*

5.1.1   Abstract

The diamond anvil cell (DAC) technique coupled with laser heating is a major method for studying materials statically at multimegabar pressures and at high temperatures. Recent progress in experimental techniques, especially in high-pressure single crystal X-ray diffraction, requires portable laser-heating systems which are able to heat and move the DAC during data collection. We have developed a double-sided laser heating system for DACs which can be mounted within a rather small (~ 0.1 m^2) area and has a weight of ~ 12 kg. The system is easily transferable between different in-house or synchrotron facilities and can be assembled and set up within a few hours. The system was successfully tested at the High Pressure Station of White Beam (ID09a) and Nuclear Resonance (ID18) beamlines of the European Synchrotron Radiation Facility (ESRF). We demonstrate examples of application of the system to a single crystal X-ray diffraction investigation of $(Mg_{0.87},Fe^{3+}_{0.09},Fe^{2+}_{0.04})(Si_{0.89},Al_{0.11})O_3$ perovskite (ID09a) and a Synchrotron Mössbauer Source (SMS) study of $(Mg_{0.8}Fe_{0.2})O$ ferropericlase (ID18).

5.1.2 Introduction

Studies of materials at conditions of extreme pressure (*P*) and temperature (*T*) are important in many areas of natural science including physics (Dewaele et al., 2008; Gregoryanz et al., 2005; Lin et al., 2004), chemistry and material synthesis (Palyanov et al., 2011; Schröder et al., 2011; Zerr et al., 2009), but especially for geosciences because of their possibility to simulate conditions of the deep Earth's interior (Kolesnikov et al., 2009; Mikhaylushkin et al., 2007; Wu et al., 2009).

The DAC) technique is a useful and easy-to-use tool for investigations under high pressure. The technique was initiated in the late 1950s, and has now become the most successful method of pressure generation in the multimegabar pressure range (Dubrovinskaia et al., 2010; Eremets, 1996). Laser heating in DACs was first introduced by Ming & Bassett (1974) and is well described in the literature (Boehler, 2000). There are numerous facilities, including specialized beamlines at the third-generation synchrotrons (Hirose, 2006; Prakapenka et al., 2008; Schultz et al., 2005; Shen et al., 2001), where the DAC laser-heating technique is coupled with different analytical methods for *in situ* investigations such as the Raman spectroscopy or X-ray diffraction (Boehler et al., 2008; Santoro et al., 2005). However, until recent times all these laser-heating systems were linked to certain equipment or to a beamline.

Modern scientific challenges demand higher flexibility in the capabilities of research techniques including laser heating in DACs. As a result, since 2009 portable DAC laser-heating systems that can be easily moved between different analytical facilities, including transfer from in-house to a synchrotron or between synchrotron beamlines, began to emerge (Boehler et al., 2009; Dubrovinsky et al., 2009). However no portable double-sided laser-heating system was able to meet all scientific needs. The system described by Boehler et al. (2009) allows double-sided laser heating but requires a large area (0.4 m^2) for the support and cannot be used for single-crystal studies. Moreover, the design of the system (Boehler et al., 2009) has a disadvantage in that simultaneous temperature and X-ray measurements are not possible due to the blocking or shadowing of the X-ray primary beam or scattered signal by inserting optical components used for collecting thermal radiation. The system described by Dubrovinsky et al. (2009) was successfully used for routine in-house experiments (Gu et al., 2011; Parakhonskiy et al., 2011), *in situ* synchrotron X-ray absorption and diffraction investigations (Narygina et al., 2011) and

(with some modifications) synchrotron single-crystal X-ray diffraction experiments (Dubrovinsky et al., 2010). But the system is only capable of one-sided laser-heating and, thus, it is limited to application to optically thin samples.

Here we report on the development of a compact double-sided laser-heating system which allows for single-crystal diffraction studies and other experiments which require rotation of the system with the DAC during data collection. The new system provides a more homogeneous temperature distribution within the sample (e.g., it allows higher temperatures without possible destruction due to thermal stress), and permits the use of thicker samples, thus providing an opportunity to use the system to work with materials that are more difficult to heat.

5.1.3   Design of the laser-heating system

The system consists of two major components – the sources of laser light and two universal laser-heating heads (UniHeads) (Fig. 5.1.3.1). The UniHeads are based on the finite cutting laser head (Precitec KG) and their functions in the portable laser system are to focus incoming laser radiation on the sample within the DAC, to provide high magnification imaging of the sample in the DAC with coaxial illumination, and to give access for multiwavelength spectroradiometry for temperature measurements (Shen et al., 2010).

A. Laser

As a laser source we have used two SPI100 modulated fiber lasers with a maximum output power of 100 W each at an excitation wavelength of 1071 nm. The weight of one laser and its power supply is 40 kg. An additionally integrated red laser source (630-680 nm) is used as an aid for initial beam alignment. The standard output of the SPI lasers has a Gaussian power distribution with a full width at $1/e^2$ height of ~ 3 mm. The output power level can be monitored and controlled by an external interface. The SPI lasers can be operated in a continuous or pulse mode with a frequency up to 100 kHz and a minimum pulse width of 10 μs. The lasers require no water cooling and use only a standard electrical plug (100-240 V ac, 2 A at 230 V).

B. Focusing optics and beam targeting

The output of the 1071 nm laser radiation is collected by a π-shaper (MolTech GmbH), bent at 90° using a specially coated beam splitter (Beam Splitter 1 on Fig. 5.1.3.1, with a reflectivity

more than 99.99% above 1050 nm, but transparent in the 400-900 nm wavelength range), and focused by a set of lenses with a 80 mm working distance installed in the UniHead. The π-shaper converts the original laser beam intensity distribution (Gaussian shape , 3 mm in diameter) to a flat top distribution with ~ 50 μm full width at half maximum (FWHM) (Prakapenka et al., 2008).
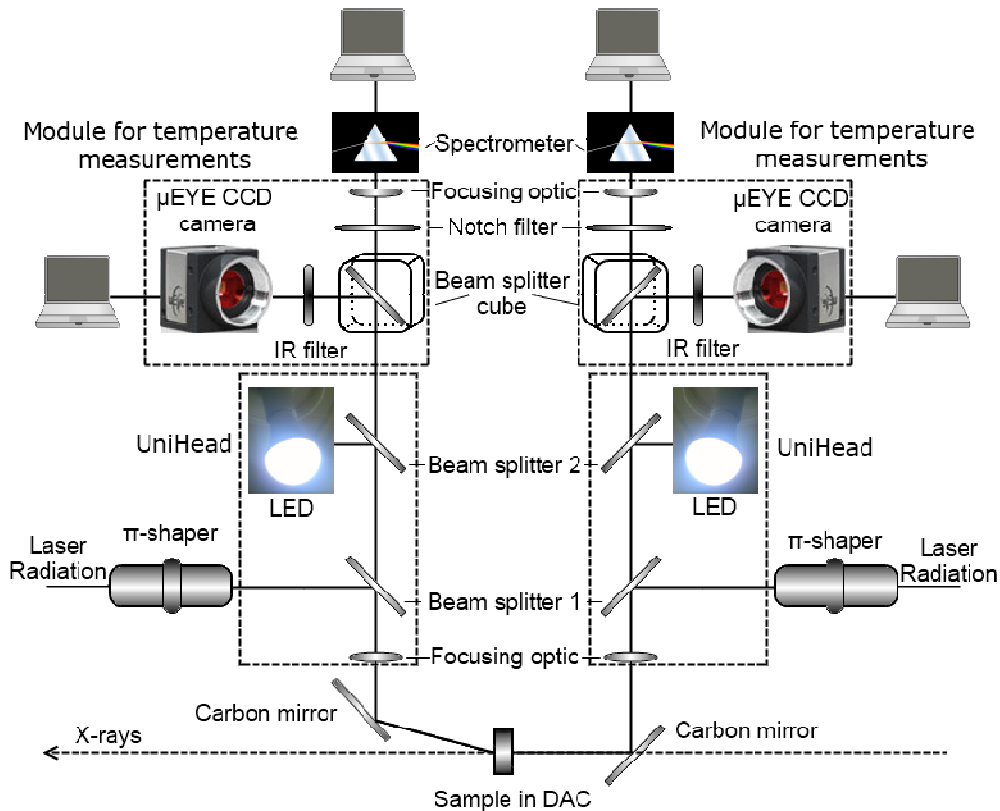
Fig. 5.1.3.1. Schematic diagram of the optical components of the laser-heating system.

In order to direct the laser beam onto the sample and make it coaxial with the incident X-ray beam, we employ carbon mirrors mounted at approximately 45° angles to the axis of the UniHeads (Figs. 5.1.3.1, 5.1.3.2). The carbon mirrors are produced at Bayreuth University using glassy carbon substrate (1 or 2 mm thick) by Sigma Aldrich Inc. They are coated by a 100 nm thick silver film, and protected by a 5 nm thick silica film. For X-ray diffraction experiments, to prevent shadowing of the X-ray beam and undesirable scattering from mirrors, the carbon mirror on the downstream side of the DAC is mounted with an angle slightly less than 45° (usually about 41°-42°). X-ray scattering from the upstream glassy carbon mirror is blocked by the body of the DAC.

C. Illumination, observation and spectroradiometry module

The sample is illuminated by a light emitting diode (LED) built into the UniHead (Fig. 5.1.3.1). The LED is controlled by an external power supply. For visual observation of the sample, high-resolution µEYE[TM] Charge-Coupled Device (CCD) cameras are used. To prevent saturation of the cameras by the reflected laser light, KG3 infra red (IR) filters (SCHOTT) are employed. The UniHeads are equipped with optical output modules for temperature measurements. They consist of a µEYE[TM] CCD camera, a focusing lens projecting the central part (of about 10 µm in diameter) of the image of the heated spot onto the end of the optical fiber, and a beam-splitter cube (50/50, Edmund Scientific Inc) (Pippinger et al., 2011). The beam-splitter cube is movable and can be fixed in two positions (Fig. 5.1.3.1). The main position is within the optical path (in this position 50% of the light is transferred to the CCD camera for visual observations). In the case of low intensity of emitted light, the beam-splitter cube can be fixed outside the optical path (where all light radiated by the heated spot is transmitted to the optical fiber). In our experiments we used an Ocean Optics QE65000 spectrometer or an Acton SP2300 spectrometer (Princeton Instruments) with a PIXIS400 CCD detector. To prevent the incidence of the laser IR light onto the detector, 1064 nm notch filters (Edmund Optics) are used. The temperature measurements are performed by the standard spectroradiometry method (Shen et al., 2010), i.e., by fitting the thermal radiation spectrum in a given wavelength range (usually 600 to 850 µm) to the Planck radiation function. The software[1] allows calibration and on-line monitoring of the temperature. The system response spectra are calibrated using the melting point of platinum (Pippinger et al., 2011).

D. System alignment

All parts, the UniHeads, a 3-axis translation stage for a DAC holder, and the holder with the DAC are mounted on a common aluminum plate (0.35×0.30 m^2, and thickness 15 mm). This plate should be first fixed to the beamline goniometer. In the experiments described below the upstream UniHead was set up horizontally and the downstream UniHead was set up vertically (Fig. 5.1.3.2). The downstream UniHead is firmly mounted on the plate and has no degrees of freedom. The sample in the DAC is aligned with respect to this UniHead using the 3-axis

---

[1] Kantor, I. & Kantor, A., unpublished
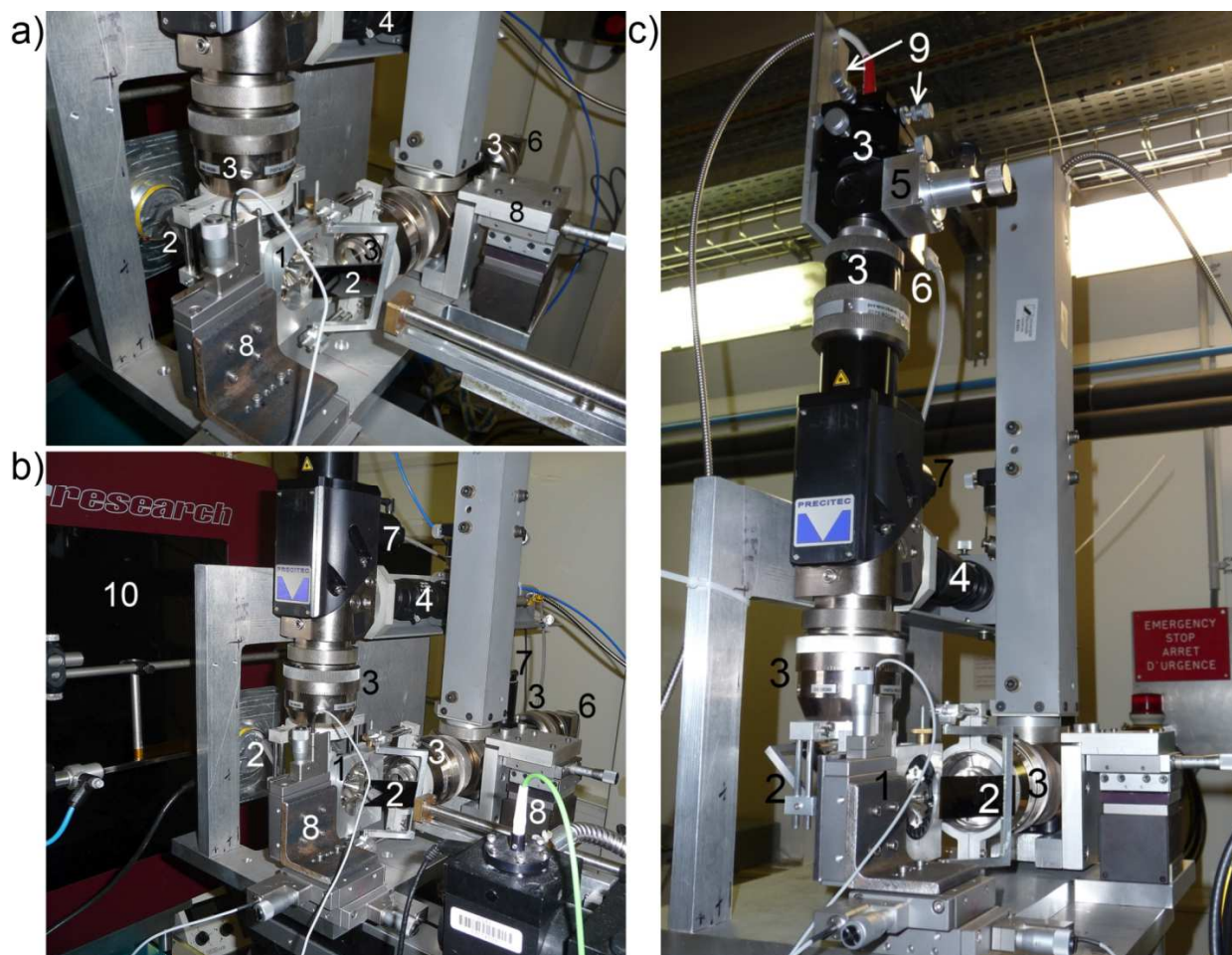
Fig. 5.1.3.2. Photographs of the double-sided portable laser-heating system mounted for experiments at ESRF beamlines ID09a (a,b) and ID18 (c). 1, holder with DAC; 2, carbon mirrors; 3, focusing optics; 4, π-shaper; 5, beam-splitter cube; 6, CCD camera; 7, LED; 8, 3-axis translation stages; 9, adjustable screws for spectrometer focusing; 10, MAR555 CCD detector.

translation stage. The red alignment laser within the SPI100 can be used to simplify the process. The upstream UniHead is mounted on its own 3-axis translation stage and is aligned to the sample within the DAC afterwards. Focusing of the laser beams on the sample is achieved through adjustable lenses of the π-shapers (Prakapenka et al., 2008). The last part of the procedure is the alignment of the spectrometers. For this purpose the end of the optical fiber, which comes to the spectrometer, is connected to the visible (in our experiments 532 nm) diode laser, whose light is focused on the sample. By means of the adjustable screws (Fig. 5.1.3.2c) of the spectroscopic module, it is placed exactly at the position of the center of the heated area. According to our experience, the complete installation of the system and its alignment requires

two to three hours. After the sample within the DAC is aligned with respect to the lasers, the whole system is aligned with respect to the X-ray beam as "one piece" using standard beamline procedure. Rotation of the system as a whole allows a constant angle of incidence of the laser beam to be maintained and thereby ensures homogeneous heating.

5.1.4 Examples of application of the portable double-sided laser-heating system

A. Mössbauer spectroscopy investigation of $Fe_{0.2}Mg_{0.8}O$ at high *P,T*

Electrical and magnetic properties strongly depend on pressure and temperature. Energy domain [57]Fe Mössbauer spectroscopy is not only one of the best methods to study the valence and spin state of iron at high pressure, but also it is ideally suited to test temperature homogeneity in laser-heated DACs. However, conventional energy-resolved Mössbauer spectroscopy utilizes radioactive sources with low brilliance. Therefore, high-pressure Mössbauer studies require collection times that are too long to be effectively applied for laser-heated DACs. The time domain analog of traditional Mössbauer spectroscopy is realized via time-resolved nuclear forward scattering of synchrotron radiation (Rüffer and Chumakov, 1996; Zhao et al., 2004). However, this method is not well suited to materials with a large number of components due to the non-uniqueness of fitting models. Recently, this problem was solved by developing (Potapkin et al., 2012) a Synchrotron Mössbauer Source (SMS)[2] at the Nuclear Resonance beamline (Rüffer and Chumakov, 1996) ID18 at the European Synchrotron Radiation Facility (ESRF). The SMS method allows energy-domain Mössbauer measurements to be performed using synchrotron radiation as a source of gamma-rays. In contrast to radioactive sources, the beam emitted by the SMS is nearly fully resonant, has high brilliance and can be focused to a 10 μm horizontal and 5 μm vertical spot sizes. The method opens the possibility for rapid and high quality measurements in DACs at high pressures and, if it is coupled with laser heating, at high temperatures. In order to test the double-sided laser-heating system with the SMS, we selected $Fe_{0.2}Mg_{0.8}O$ (ferropericlase, Fp20), since its Mössbauer spectra at high pressure and temperature are already known from our previous work using an externally heated diamond anvil cell (Kantor et al., 2009). Pellets of Fp20 of 30 to 40 μm in diameter with a thickness of about 15 μm were loaded along with Ne as a pressure-transmitting medium (Kurnosov et al., 2008) into a pressure

---

[2] SMS as an acronym for "Synchrotron Mössbauer Source" should not be confused with the same acronym coined by Advanced Photon Source users that means "Synchrotron Mössbauer Spectroscopy"
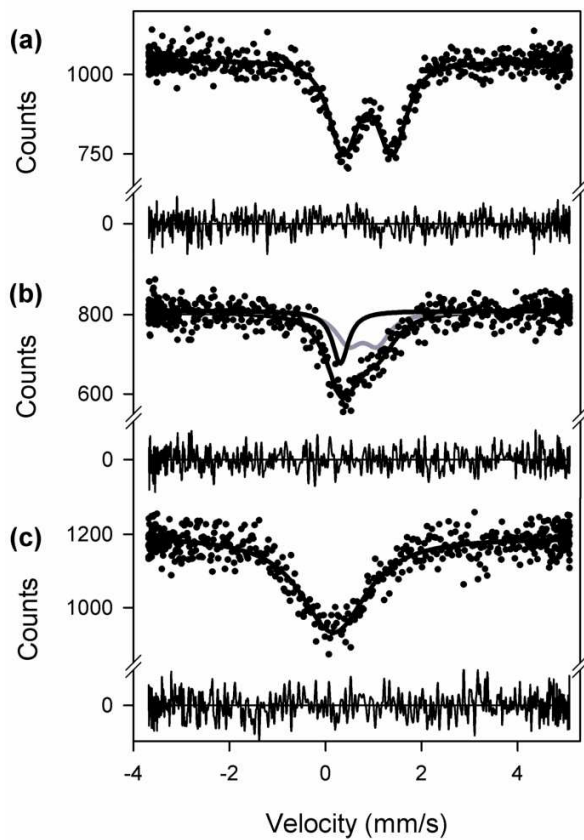
Fig. 5.1.4.1. Spectra of $Fe_{0.2}Mg_{0.8}O$ at 29 GPa collected using the SMS: (a) room temperature; (b) laser heating with poor alignment between laser and synchrotron beams; (c) double-sided laser heating with good alignment. The solid lines show the fits to experimental data. The temperatures determined from the centre shift of the fitted subspectra are 450 K (grey doublet in (b)), 1000 K (black singlet in (b)) and 1300 K (singlet in (c)). The fit residuals are shown below each spectrum.

chamber (initial diameter of 100 μm and a height of about 30 μm) made in a Re gasket. The sample was compressed using a symmetric piston-cylinder type DAC fabricated at Bayerisches Geoinstitut. All measurements were carried out at beamline ID18 using the SMS and each spectrum was collected for 10 minutes. The room temperature Mössbauer spectrum of the high-spin phase (P < 50 GPa) consists of a single quadrupole doublet arising from octahedrally coordinated Fe^{2+} (Fig. 5.1.4.1a) (Kantor et al., 2006). Upon one-sided laser heating with a 50μm focused beam (or during double-sided heating when the X-ray beam and laser spot are not well aligned), the spectrum becomes asymmetric (Fig. 5.1.4.1b). Since we know from previous experiments (Kantor et al., 2009) on $Fe_{0.2}Mg_{0.8}O$ that temperature causes a decrease in quadrupole splitting, we interpret the spectrum shown in Fig. 5.1.4.1b as a superposition of relatively cold material (grey doublet) and hotter material (black singlet) subspectra, caused by temperature inhomogeneities in the sample, corresponding approximately to temperatures of 450 K and 1000 K, respectively. The temperatures were determined from the centre shift of the fitted subspectra. Fitting the spectrum to only two subspectra is a simplification, as in reality the

spectrum is comprised of a distribution of doublets, where centre shift and quadropole splitting decrease with temperature. During double-sided heating with the correct alignment of the X-ray beam and the laser spot, the Mössbauer spectrum becomes more symmetric (Fig. 5.1.4.1c) and shows a temperature of 1300 K. We found that temperature gradients also arise from double-sided laser heating of thick samples (above ~ 20 µm), where the interior of the sample remains colder than the surface.

B. Single crystal X-ray diffraction of Fe,Al-rich magnesium silicate perovskite in a double-sided laser-heated DAC

Iron- and aluminum-bearing magnesium silicate perovskite $(Mg,Fe,Si,Al)O_3$ is likely the main component of the Earth's lower mantle. Iron and aluminum may significantly affect the properties of magnesium silicate perovskite, especially due to electronic transitions in Fe^{2+} and Fe^{3+}. Recent single crystal diffraction studies (Boffa Ballaran et al., 2012; Dubrovinsky et al., 2010) reveal that ferrous and ferric magnesium silicate perovskites do not demonstrate any sign of irregular changes in the behavior of the molar volume, lattice parameters, and mean bond distances of the $(Si,Al)O_6$ octahedra and $(Mg,Fe)O_8$-polyhedra which could be related to the high-spin–low-spin (HS-LS) crossover. Catalli et al., (2010) suggested that spin crossover could be favored at high temperatures and pressures above ~ 40 GPa by the reaction $Fe_A^{3+(HS)}+Al_B^{3+} \rightarrow Fe_B^{3+(LS)}+Al_A^{3+}$ (where subscripts "A" and "B" denote the corresponding positions in the perovskite structure). Glazyrin et al., (2014) did not find evidence of such a process for Fe^{3+}- and Al^{3+}-rich compositions ($Fe^{3+}/\Sigma Fe > 0.9$, $Al^{3+} \sim 0.4$). In order to check if such a site exchange would take place in magnesium silicate perovskite with moderate aluminum and ferric iron content, we employed the portable double-sided laser heating system at beamline ID09a (Häuserma and Hanfland, 1996) at the ESRF.

Single crystals of $(Mg_{0.87}Fe^{3+}_{0.09}Fe^{2+}_{0.04})(Si_{0.89}Al_{0.11})O_3$ perovskite (the crystal chemical formula is based on results of electron microprobe analysis and Mössbauer spectroscopy) were synthesized in a multianvil apparatus (Dubrovinsky et al., 2010). A crystal with dimensions of ~ $0.015 \times 0.010 \times 0.010$ mm^3 was loaded along with Ne as a pressure-transmitting medium (Kurnosov et al., 2008) into a pressure chamber made in a Re gasket (with an initial diameter of 100 µm and a height of about 30 µm) and compressed using a symmetric piston-cylinder type

DAC equipped with ALMAX-type diamonds (80° opening and 250 μm culets). Diffraction data were collected with radiation of wavelength 0.4149 Å, beam size 10x10 μm^2, and a crystal-to-detector distance of about 399 mm using the MAR555 Flatpanel detector. Ninety-six frames in the omega scanning range of –28° to +20° degrees were collected (0.5° scanning step size) with an exposure time of 1 s. At each pressure-temperature point, data were collected at two different positions of the DAC that varied by 90° along the compression direction, and the datasets were merged. The data were processed using the Crysalis software (Oxford Diffraction (2006) Crysalis RED, version 1.171.31.8. Oxford Diffraction Ltd., Abingdon, Oxfordshire). Crystal structure refinements of integrated intensities were carried out with the SHELXL-97 WinGX version (Farrugia, 1999; Sheldrick, 2008).

We collected the diffraction data at pressures between 65 and 78 GPa (where pressure was determined from the Ne thermal equation of state (Fei et al., 2007)) in several sets, namely before, during, and after laser heating at 1750(50) K (Table 5.1.4.1). For each P, T data point we obtained between 105 and 125 unique reflections. In addition to the atomic coordinates and isotropic thermal parameters, we refined the occupancy of the B-site by Si and Fe (Si and Al are not distinguishable), and that of the A-site by Mg and Fe (Table 5.1.4.1). Structural refinements on the integrated intensities converged with values of the R-factor below 5%. We found that (a) the refined amount of iron in the A-site coincides, within uncertainty, with the value determined by microprobe data, (b) laser heating does not affect the chemical composition of the magnesium silicate perovskite in our experiments, and (c) high temperature does not promote any chemical exchange reactions between the A- and B-sites (i.e., there is no evidence that Fe enters the B-site during heating). It should be mentioned that homogeneous heating is a critical parameter suppressing undesirable diffusion and formation of chemical inhomogeneities. Our results are in full agreement with the results of Glazyrin et al. (2014), obtained from magnesium silicate perovskite of another composition. Note that previous data that we reported using a one-sided laser-heating system (Dubrovinsky et al., 2010) allowed the collection of only less than 70 reflections per run, which precluded a refinement of cation site occupancies.

Table 5.1.4.1. Results of a single crystal structural refinement of $(Mg_{0.87}Fe^{3+}_{0.09}Fe^{2+}_{0.04})(Si_{0.89}Al_{0.11})O_3$ perovskite (space group P*bnm*) at different pressures and temperatures.

P, GPa	T, K	R1, %	a, Å	b, Å	c, Å	V Å³/unit cell	Atomic parameters (xyzU) Si_B, Fe_B, Mg_A, Fe_A*
65.9(5)	298	3.2	4.4875(3)	4.7138(3)	6.4826(23)	137.13(15)	A -0.0178(4) 0.4305(5) 0.25 0.016(1)
							B 0 0 0 0.014(1)
							O1 0.1135(11) 0.0346(8) 0.25 0.019(1)
							O2 0.1873(6) 0.3063(7)
							-0.0578(8) 0.017(2)
							1.00(1) 0.00(1) 0.88(2) 0.12(1)
78(1)	1750(50)	4.4	4.4733(6)	4.7101(5)	6.4874(45)	136.69(20)	A -0.0183(5) 0.4334(7) 0.25 0.030(1)
							B 0 0 0 0.025(1)
							O1 0.1131(14) 0.0326(12) 0.25 0.034(2)
							O2 0.1832(8) 0.3080(9)
							-0.0616(14) 0.031(2)
							1.01(1) 0.00(1) 0.88(2) 0.12(1)
63.2(3)	298	3.7	4.4975(5)	4.7270(4)	6.4996(7)	138.18(11)	A -0.0167(3) 0.4305(5) 0.25 0.026(1)
							B 0 0 0 0.023(1)
							O1 0.1183(8) 0.0313(8) 0.25 0.027(1)
							O2 0.1868(6) 0.3051(6) -0.0603(7) 0.027(1)
							1.01(1) 0.00(1) 0.87(2) 0.128(16)

*The notation "Si_B, Fe_B, Mg_A, Fe_A" indicates the occupancy of the corresponding atom in the A- or B-site.

5.1.5 Conclusions

We have developed a portable laser-heating system that allows homogeneous double-sided heating with in situ visual observation of the sample and temperature measurement. The system can be easily mounted in the laboratory or at large scale scientific facilities, including synchrotron beamlines. All major components of the system are commercially available, which facilitates its duplication. The ready-to-use system can be assembled and aligned by users with only basic training. The system has been successfully tested for single crystal X-ray diffraction and for energy-domain Mössbauer spectroscopy using the SMS at the ESRF.

5.1.6 Acknowledgments

5.2 Electronic spin state of Fe,Al-containing MgSiO₃ perovskite at lower mantle conditions

I. Kupenko[a,b,*], C. McCammon[b], R. Sinmyo[b], C. Prescher[b], A.I. Chumakov[a], A. Kantor[a], R. Rüffer[a], L. Dubrovinsky[b]

a European Synchrotron Radiation Facility, BP 220, F-38043 Grenoble, France

b Bayerisches Geoinstitut Universität Bayreuth D-95440 Bayreuth, Germany

Corresponding author. E-mail address: kupenko@esrf.fr

5.2.1 Abstract

We have investigated silicate perovskite with composition $Mg_{0.83}Fe_{0.21}Al_{0.06}Si_{0.91}O_3$ relevant for the lower mantle at pressures up to 81 GPa and temperatures up to 2000 K using conventional Mössbauer spectroscopy and synchrotron Nuclear Forward Scattering (NFS) combined with double-sided laser heating in a diamond anvil cell. Room temperature Mössbauer and NFS spectra at low pressure are dominated by high-spin Fe^{2+}, with minor amounts of Fe^{3+} and a component assigned to a metastable position of high-spin Fe^{2+} in the A-site predicted by computational studies. NFS data show a sharp transition (< 20 GPa) from high-spin Fe^{2+} to a new component with extremely high quadrupole splitting, similar to previous studies. Mössbauer data show the same transition, but over a broader pressure range likely due to the higher pressure gradient. The new Fe^{2+} component is assigned to intermediate-spin Fe^{2+}, consistent with previous X-ray emission studies. NFS data at high temperatures and high pressures comparable to those in the lower mantle are consistent with the presence of Fe^{2+} only in the intermediate-spin state and Fe^{3+} only in the high-spin state. Our results are therefore consistent with the occurrence of spin crossover only in Fe^{2+} in Fe-, Al-containing perovskite within the lower mantle.

5.2.2 Introduction

Magnesium silicate perovskite (Pv) is considered to be the most abundant constituent of the Earth's lower mantle with stability from a depth of 660 km to approximately 2700 km, which is several hundred kilometers above the core-mantle boundary (Liu, 1976). Pv incorporates notable amounts of iron and aluminum (5-10 mol%) into its structure (e.g., Lee et al., 2004). While the

properties and behavior of pure $MgSiO_3$ Pv are mostly understood, the effects of these additional cations remain controversial.

The electronic spin state of iron in different valence states in Pv can strongly influence many properties of the Earth's interior such as thermal conductivity (Badro et al., 2004), electrical conductivity (Ohta et al., 2010; Potapkin et al., 2013), and thermodynamic properties (Frost et al., 2004; McCammon, 1997). An accurate determination of the Fe spin state in Pv is complicated by the presence of two different crystallographic sites (a large distorted 8-12-coordinated site, hereafter referred to as A, and a smaller relatively undistorted octahedral site, hereafter referred to as B). Iron occurs both as ferrous (Fe^{2+}) and ferric (Fe^{3+}) in Fe-, Al-containing magnesium silicate perovskite (FeAlPv), with $Fe^{3+}/\Sigma Fe$ ratios up to at least 60% (Frost et al., 2004; McCammon, 1997), that strongly depend on the Al concentration (McCammon et al., 2004).

While it is well accepted that Fe^{2+} occupies exclusively the A-site, the site occupancy of Fe^{3+} is still under debate. Ferric iron has been observed to occupy either exclusively the A-site (McCammon et al., 2008; Potapkin et al., 2013) or both the A- and B-sites (Badro et al., 2004; Catalli et al., 2011, 2010; Hummer and Fei, 2012). Several studies have additionally predicted an exchange of Fe^{3+} from the A- to the B-site at high pressures (Catalli et al., 2011, 2010; Fujino et al., 2012); however the possibility of such exchange was disproved by recent single-crystal X-ray diffraction studies conducted at high pressure and high temperature (Glazyrin et al., 2014; Kupenko et al., 2012b).

The spin state of iron in iron-containing magnesium silicate perovskite (FePv) as well as in FeAlPv is also a matter of debate. Some studies conclude that Fe_A^{3+} undergoes high-spin (HS) to low-spin (LS) crossover (Jackson, 2005; Li et al., 2006), although the majority of studies do not observe spin crossover in Fe_A^{3+} (Catalli et al., 2011, 2010; Fujino et al., 2012; Lin et al., 2012; McCammon et al., 2008; Potapkin et al., 2013). Meanwhile there is a general consensus that Fe_B^{3+} undergoes HS to LS crossover at mantle pressures in studies where Fe^{3+} is reported to occupy the B site (Catalli et al., 2011, 2010; Fujino et al., 2012; Lin et al., 2012). There is also general agreement that Fe^{2+} behavior undergoes a dramatic change at mantle pressures through the appearance of a new component with extremely high quadrupole splitting in Mössbauer spectra

70

at high pressure (reviewed by McCammon et al., 2013), even though there are conflicting interpretations of this change: HS to intermediate-spin (IS) crossover (Lin et al., 2008; McCammon et al., 2010, 2008; Potapkin et al., 2013), HS to LS crossover (Badro et al., 2004) or a structural modification of the local environment (Lin et al., 2012).

Numerous theoretical studies have been made that examine the spin behavior of iron in different valence states and different crystallographic sites, but with often conflicting results (Bengtson et al., 2009, 2008; Caracas et al., 2010; Hsu et al., 2011, 2010; Li, 2005; Stackhouse et al., 2007; Umemoto et al., 2010; Zhang and Oganov, 2006). However one point on which all computational models agree in the instability of IS Fe^{2+} at all lower mantle pressures, which is in conflict with experimental results that show a decrease in the unpaired spin density of iron in FePv and FeAlPv (reviewed by McCammon et al., 2013).

Despite the many investigations, a systematic study of FeAlPv with mantle composition at mantle conditions is still lacking. Moreover all predictions of FeAlPv behavior at lower mantle conditions have been inferred by extrapolation of data measured at ambient temperatures or from ab initio calculations. Here we report the first *in situ* NFS study of FeAlPv with composition $Mg_{0.83}Fe_{0.21}Al_{0.06}Si_{0.91}O_3$ at pressure and temperature conditions of the lower mantle. The study is complemented by NFS and conventional Mössbauer spectroscopy measurements at high pressure and ambient temperature that provide high resolution data for the analysis of individual site and valence state contributions.

5.2.3 Experimental methods

The sample of FeAlPv was synthesized in the multianvil press from a mixture of MgO, SiO_2, Al_2O_3, $^{57}Fe_2O_3$ (90% enriched) starting materials in a rhenium capsule at 26 GPa and 1800°C for 30 min. Before synthesis, the starting material was heated at 1273 K for 1 day in a CO-CO_2 gas-mixing furnace, in which oxygen fugacity was controlled at $\log fO_2 = -21$ to reduce Fe^{3+} to Fe^{2+}. After the multianvil experiment, the recovered sample was characterized at ambient conditions using both the electron microprobe (JEOL, JXA-8200, under the operating conditions 15 kV and 15 nA) and Mössbauer spectroscopy. Results of electron microprobe analysis showed that the chemical composition of the sample is $Mg_{0.828(18)}Fe_{0.208(13)}Al_{0.059(2)}Si_{0.911(23)}O_3$ and Mössbauer spectroscopy showed the iron to be predominantly in the ferrous state (~ 20% $Fe^{3+}/\Sigma Fe$).

Mössbauer spectra were recorded at room temperature in transmission mode on a constant acceleration Mössbauer spectrometer with a nominal 370 MBq ^{57}Co high specific activity source in a 12 µm thick Rh matrix with active dimensions of 500 µm × 500 µm. The velocity scale was calibrated relative to 25 µm thick α-Fe foil using the positions certified for (former) National Bureau of Standards standard reference material no. 1541; line widths of 0.36 mm/s for the outer lines of α-Fe were obtained at room temperature. Spectra took 3-4 days each to collect. Centre shifts were calculated relative to α-Fe. Spectra were fitted using a full transmission integral with a normalized Lorentzian source lineshape using the MossA software package (Prescher et al., 2012). Mössbauer spectra of the FeAlPv sample were collected up to 72 GPa at room temperature (Fig. 5.2.3.1). The sample was annealed preceding data collection at all pressures above 30 GPa in order to relax stress.

NFS data were collected on the Nuclear Resonance (ID18) beamline (Rüffer and Chumakov, 1996) of the European Synchrotron Radiation Facility during operation in 4-bunch mode, with the beam focused to 6 µm vertical and 11 µm horizontal dimension using Kirkpatrick-Baez mirrors. All of the spectra were collected over 10-60 min each. NFS data were fit using the CONUSS package (Sturhahn, 2000). The centre shift was determined relative to a $K_2Mg^{57}Fe(CN)_6$ reference absorber. Room temperature NFS spectra were collected up to 81 GPa. Additionally at 43, 63 and 81 GPa the sample was laser heated at 1200 K–2000 K and spectra were collected during laser heating.

High-pressure measurements were carried out using cylindrical-type diamond anvil cells (Kantor et al., 2012). Samples of FeAlPv were loaded together with a few ruby balls used as a pressure marker. The diamond anvils used had 250 μm culets. A 200 μm thick Re gasket was pre-indented to about 30 μm thickness and a 125 μm hole was drilled in the centre. Samples were loaded at room temperature and Ne was loaded as a pressure medium at a pressure of 1.2 kbar (Kurnosov et al., 2008).

For high temperature measurements a modified version of the portable double-sided laser heating system was used (Dubrovinsky et al., 2010, 2009; Kupenko et al., 2012b). The setup was installed at the ID18 beamline and consists of two SPI modulated fiber lasers (wavelength 1071 nm) with 100 W maximum power and two laser heating heads. The system implements π-shapers (Prakapenka et al., 2008) that convert an initial Gaussian-shaped beam to one with a flat

top distribution with ~ 50 μm full width at the half maximum (FWHM) in order to provide homogeneous heating. The measurement of temperature was performed with the standard spectroradiometry method (Shen et al., 2010) using an Ocean Optics QE650000 spectrometer.
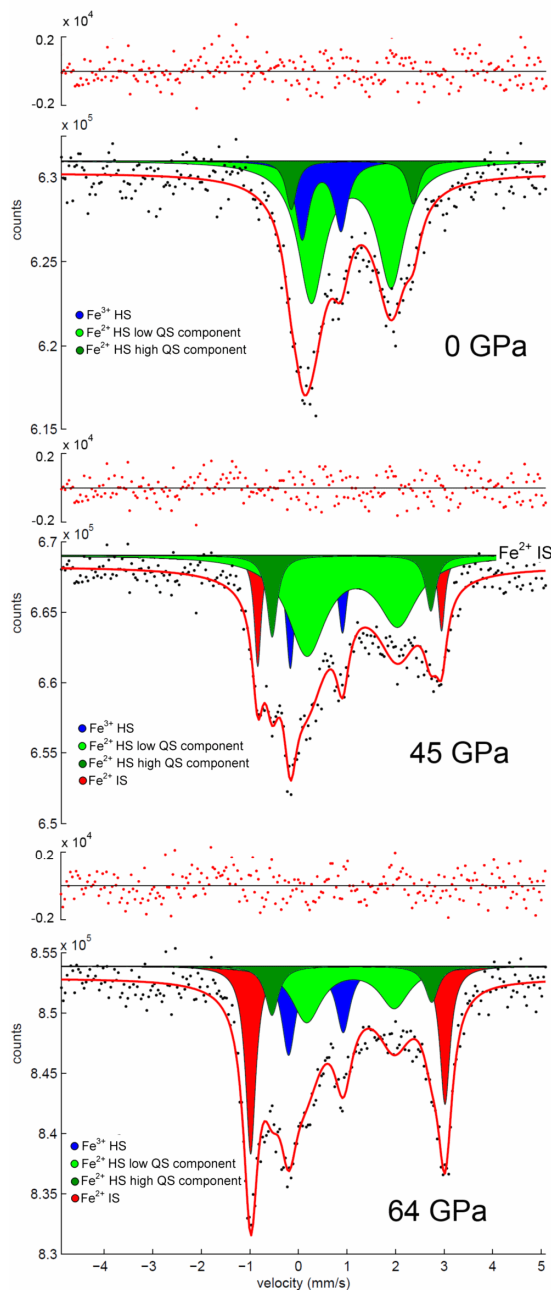

Fig. 5.2.3.1. Selected high-pressure conventional Mössbauer spectra of $Mg_{0.83}Fe_{0.21}Al_{0.06}Si_{0.91}O_3$ perovskite at room temperature. The solid lines show the theoretical fit and the residual is indicated above each spectrum.

5.2.4 Results

At low pressures the Mössbauer spectra were fitted to three doublets, one assigned to HS Fe^{3+} with ~ 1 mm/s quadrupole splitting (QS) and ~ 0.35 mm/s centre shift (CS) and two assigned to HS Fe^{2+} (QS ~ 1.6 mm/s and ~2.5 mm/s, both CS ~ 1 mm/s), based on their hyperfine parameters. Up to 37 GPa the spectra remain nearly unchanged with only moderate decrease of the CS and increase of the QS of all components (Fig. 5.2.4.1). At 37 GPa a new component begins to emerge, similar to all previous Mössbauer studies of Al-free FePv (Lin et al., 2008; McCammon et al., 2010, 2008; Narygina et al., 2010), which is accompanied by an intensity reduction of the HS low QS Fe^{2+} doublet. The new component has QS > 3 mm/s and CS ~ 1
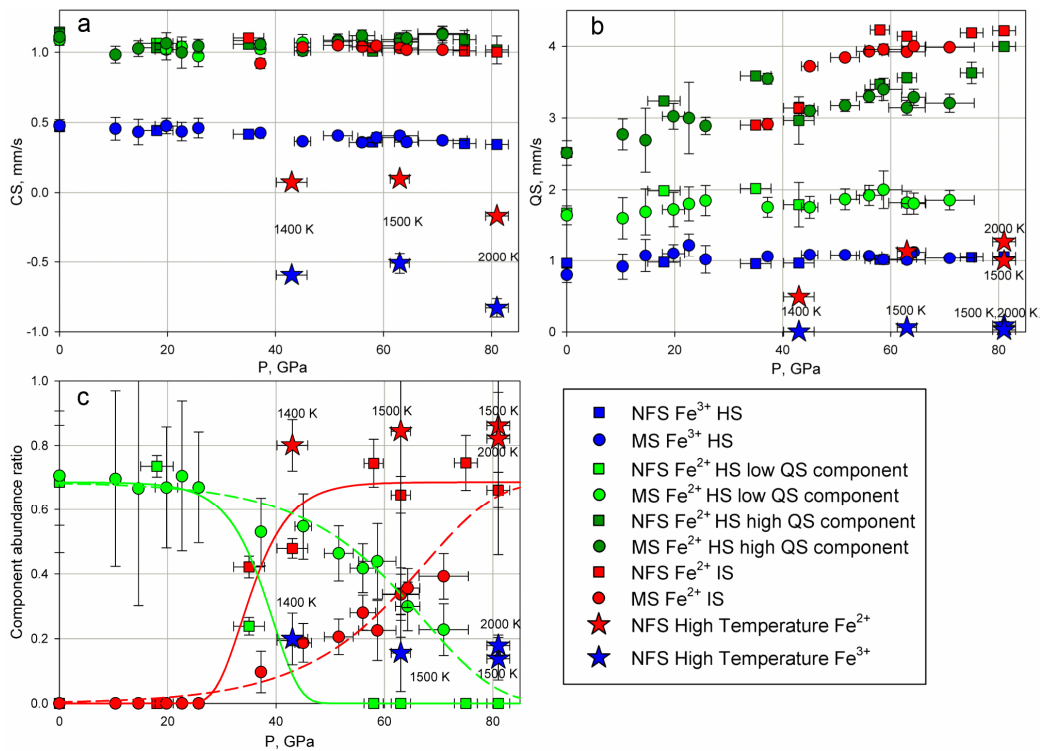
Fig. 5.2.4.1. Effect of pressure on the hyperfine parameters of $Mg_{0.83}Fe_{0.21}Al_{0.06}Si_{0.91}O_3$ perovskite as measured by Mössbauer spectroscopy (MS) and nuclear forward scattering (NFS): (a) Centre shift (CS); (b) Quadrupole splitting (QS); (c) Relative abundance. Green and red curves indicate the trends of the relative abundance for the Fe^{2+} high-spin (HS) low QS and Fe^{2+} intermediate-spin (IS) components, respectively, while the dashed and solid curves indicate the trends for the MS and NFS data, respectively . For clarity the relative abundance of the Fe^{3+} and HS high QS Fe^{2+} components are not shown, which remain relatively constant at all pressures at values of 20% and 10%, respectively.

mm/s. With further pressure increase the relative area ratio of the new component grows at the expense of the HS low QS doublet. The relative area ratios of the HS high QS Fe^{2+} (~10%) and Fe^{3+} (~20%) components remain essentially unchanged as a function of pressure. As discussedfurther below, we regard the two HS Fe^{2+} components to correspond to the two different configurations of Fe^{2+} in the A-site first introduced by Hsu et al. (2010). Based on arguments already presented in McCammon et al. (2008), Narygina et al. (2010) and McCammon et al. (2013), the new Fe^{2+} component is assigned to IS Fe^{2+}. The zero pressure NFS spectrum of FeAlPv is dominated by quantum beats arising from the HS Fe^{2+} component with QS ~1.6 mm/s and CS~1 mm/s (Fig. 5.2.4.2). The deviation of the fit at 0 GPa can be due to additional components that are present only at low pressure, such as from a small degree of amorphization due to the metastabilty of FeAlPv at ambient conditions. These components are not normally resolvable in a conventional Mössbauer spectrum due to peak overlap. Good fits to the NFS spectra are obtained above 35 GPa after annealing at high temperatures, and hyperfine parameters and the relative abundance of components are in good agreement with our Mössbauer data. At 35 GPa high frequency beats begin to appear, arising from a new high QS component. The relative abundance of the dominant low pressure HS Fe^{2+} component starts to decrease from this pressure and reduces to zero at 58 GPa (Fig. 5.2.4.1, 5.2.4.2). The QS of the new component increases rapidly from 3.0 mm/s at 35 GPa to 4.2 mm/s at 57 GPa. Upon further compression no further changes of the spectra are observed.

High temperature NFS spectra of FeAlPv (Fig. 5.2.4.3) are more challenging to fit. The approach that is most consistent with all available information comprises two QS components, one with QS ~ 0 and CS ~ -0.7 mm/s, and one with QS ~ 0.5-1.2 mm/s and CS ~ 0 mm/s. The relative abundance of the near zero QS component is equal within uncertainty to the proportion of Fe^{3+}, while likewise the relative abundance of the second component is equal to the total Fe^{2+} proportion. After temperature quenching, the relative abundance and hyperfine parameters of all components return to their original values before heating.

The misfit seen in the fits in Fig. 5.2.4.3 can be attributed to several factors. The spectra are fit to two components with distinct hyperfine parameters; however both CS and QS will vary due to small deviations of temperature during data collection. The data therefore represent a superposition of multiple spectra arising from slightly different hyperfine parameters. However

incorporating such an approach in the fitting process is not statistically meaningful due to the increased number of degrees of freedom, even though the conclusions would be unchanged. We emphasize the robustness of the fits shown in Fig. 5.2.4.3 despite their apparent flat appearance, and that the derived hyperfine parameters fulfill all of the required consistency checks (trends in CS, QS and relative abundance with pressure and temperature). Nevertheless we explored other possible fits of the high temperature NFS data and present one alternative in the supplementary material.
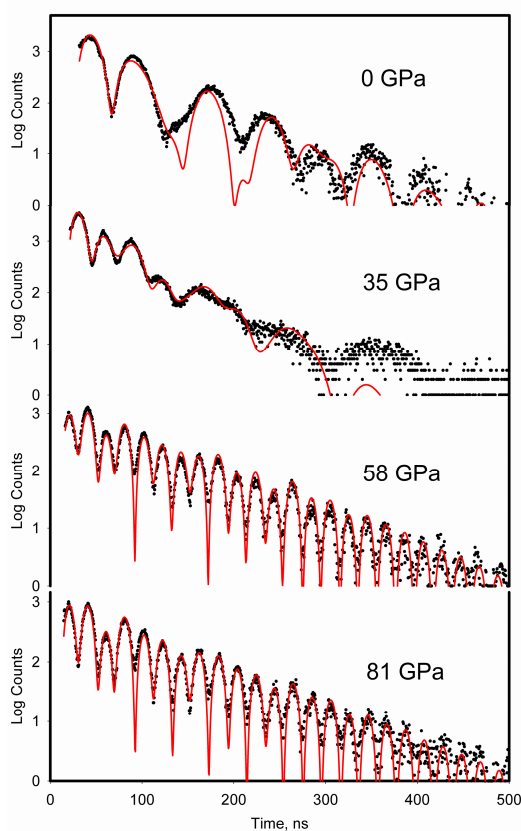
Fig. 5.2.4.2. Selected high-pressure NFS spectra of $Mg_{0.83}Fe_{0.21}Al_{0.06}Si_{0.91}O_3$ perovskite at room temperature. The solid lines show the theoretical fits.

5.2.5 Discussion

There is an ongoing debate regarding the nature of Fe^{2+} in FePv and FeAlPv at high pressure. There is general agreement that a dramatic change occurs in Mössbauer and NFS spectra through the appearance of a new high QS component with increasing pressure, but the community is polarized as to whether this represents HS to IS crossover, or stable HS Fe^{2+} undergoing a

change in the local environment of the A-site. The latter hypothesis is particularly favored by computational studies that show the presence of multiple discrete atomic configurations of Fe^{2+} in the A-site that has been postulated to explain observations in Mössbauer and NFS data (Bengtson et al., 2009, 2008; Caracas et al., 2010; Hsu et al., 2011, 2010; Li, 2005; Stackhouse et al., 2007; Umemoto et al., 2010; Zhang and Oganov, 2006). Our room temperature FeAlPv spectra, similar to those published in the literature for both FePv and FeAlPv with similar compositions (McCammon et al., 2010, 2008; Narygina et al., 2010; Potapkin et al., 2013) and derived hyperfine parameters that fall within ranges defined by previous data (reviewed by McCammon et al., 2013), provide an explanation for these results from computational studies.
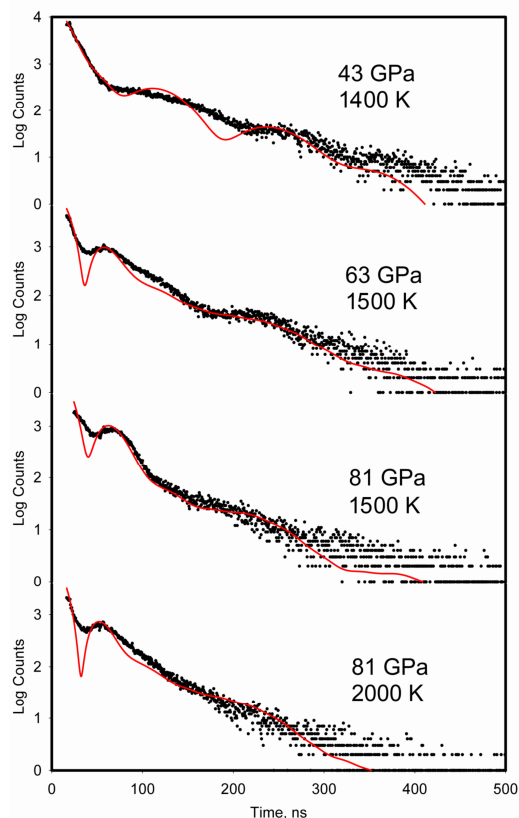
Fig 5.2.4.3. High-pressure NFS spectra of $Mg_{0.83}Fe_{0.21}Al_{0.06}Si_{0.91}O_3$ perovskite at high temperature. The solid lines show the theoretical fits.

Ab initio calculations have reported that Fe^{2+} may occupy metastable positions in addition to the dominant position of lowest energy within the large A-site cage in the perovskite structure, and thus Fe^{2+} may experience different electrical field gradients. It is therefore possible for iron to have the same spin state and crystallographic coordination, yet different QS (Bengtson et al.,

77

2009, 2008; Caracas et al., 2010; Hsu et al., 2011, 2010; Li, 2005; Stackhouse et al., 2007; Umemoto et al., 2010; Zhang and Oganov, 2006). We suggest that our Mössbauer spectra show evidence for two HS configurations, namely that the HS low QS component (light green in Figs. 5.2.3.1 and 5.2.4.1) corresponds to the stable position of Fe^{2+} within the A-site and that the HS high QS component (dark green in Figs. 5.2.3.1 and 5.2.4.1) corresponds to a metastable position of Fe^{2+} within the A-site. Thus at ambient conditions, ~ 10% of Fe^{2+} atoms occupy a metastable position.

We observe a dramatic difference in the behavior of HS high QS and low QS Fe^{2+} components with pressure (Fig. 5.2.4.1). The QS of the HS high QS Fe^{2+} component (dark green in Figs. 5.2.3.1 and 5.2.4.1) increases gradually with pressure over the entire pressure range and its abundance ratio (~ 10% of total Fe) remains unchanged within experimental error at all examined pressures. In contrast the relative abundance of the HS low QS Fe^{2+} component (light green in Figs. 5.2.3.1 and 5.2.4.1) starts to decrease at 35 GPa at the expense of increasing relative abundance of a new Fe^{2+} component with high QS (red in Figs. 5.2.3.1 and 5.2.4.1). The transition to the new component is much sharper in the NFS data (35-55 GPa) compared to the Mössbauer data (35-85 GPa), which we attribute to the well focused nature of the synchrotron beam which significantly reduces pressure gradients in the radial direction, in contrast to conventional Mössbauer spectroscopy where absorption spectra are acquired from the entire pressure chamber due to the significantly larger beam size. X-ray diffraction studies show no significant increase of structural distortion in this pressure range (Boffa Ballaran et al., 2012; Catalli et al., 2011, 2010; Lundin et al., 2008); hence it is unlikely that the transition is caused by a change in the structure. The most plausible cause for the change in relative abundance of the Fe^{2+} components is spin crossover, and further arguments in favor of assignment of the new component to IS Fe^{2+} are discussed in the literature (reviewed by McCammon et al., 2013).

In the high temperature NFS spectra the component with almost zero QS is inferred to be due to Fe^{3+}, since it is well known that temperature causes a decrease in QS of HS Fe^{3+} (Kantor et al., 2009) and its relative abundance is equivalent to the value for Fe^{3+} in the room temperature spectra. The second component in the high temperature NFS spectra is therefore assigned to Fe^{2+} because of consistency with the total Fe^{2+} abundance. Previous studies have demonstrated that temperatures around 1000 K promote HS to IS crossover and stabilize the IS state relative to the

HS state (Lin et al., 2008; McCammon et al., 2008), and our data are consistent with these observations.

The CS values provide a measure of the mean temperature of the sample. There are two main contributions to the CS – isomer shift and second order Doppler shift (SOD) (e.g., Greenwood and Gibb, 1971; Housley and Hess, 1966). The SOD varies approximately linearly with temperature for both Fe^{2+} and Fe^{3+} components in the high-temperature Debye limit, which can be estimated as $\Delta v = -7.3 \cdot 10^{-4}$ mm/s/K. Therefore the SOD provides a measure of the temperature of exactly those atoms which are responsible for the spectral signal. We obtain temperatures based on the change in CS between spectra collected under hot and cold conditions (assuming that the isomer shift does not change with temperature) of 1690(13) K, 1530(50) K and 1900(3) K for the spectra at 43 GPa, 63 GPa and 81 GPa, respectively, which is in good agreement with spectroradiometry measurements (1400 K, 1500 K and 2000 K, respectively). Our previous experiments (Kupenko et al., 2012b) showed that large discrepancies can occur between optically measured temperatures and temperatures deduced from the SOD in samples that are thick or where the laser and X-ray beams are not well aligned. The good agreement between the temperatures determined by the two different methods in this study therefore indicates that the internal temperature of the sample is close to that of the surface temperature, and hence that the double-sided laser heating setup provides homogeneous heating of the sample.

5.2.6 Conclusion

At ambient temperature and pressures above 35 GPa Fe^{2+} in FeAlPv occurs predominantly in a component assigned to the IS state with a minor proportion assigned to the HS state located in a metastable next nearest neighbor environment position within the A-site. The component assigned to IS Fe^{2+} is stable at pressures and temperatures corresponding to those in the lower mantle and we observe no evidence of spin crossover of Fe^{3+} up to 81 GPa and 2000 K. We therefore conclude that iron in FeAlPv in the lower mantle occurs almost entirely as Fe^{2+} in the IS state and Fe^{3+} in the HS state.

5.2.7 Acknowledgments

Education and Research (BMBF), the German Research Foundation (DFG) in their normal funding program and the Priority Program 1236, and the PROCOPE exchange program.

5.2.8 Supplementary information

We present an alternative fit to the high temperature NFS spectra of FeAlPv. Fig. 5.2.8.1 illustrates a fit with two quadrupole components: one with QS ~ 0 and CS ~ –0.8 mm/s (80% relative abundance) and one with QS ~ 0.7 mm/s and CS ~ 0 mm/s (20% relative abundance).

Statistically the fits to the NFS data are slightly better than those presented in the main paper, although it is not possible to extract a unique interpretation of the fits. A large increase in intensity of the low velocity component could arise from a number of effects, including a redistribution of d electrons within iron atoms, a change in the probability of the high- and low-energy transitions between the nuclear excited and ground states, or electron transfer between iron and oxygen. Future collection of complementary energy domain Mössbauer data under similar pressure and temperature conditions using the synchrotron Mössbauer source (SMS) (Potapkin et al., 2013, 2012) could help to resolve the ambiguities in data interpretation.
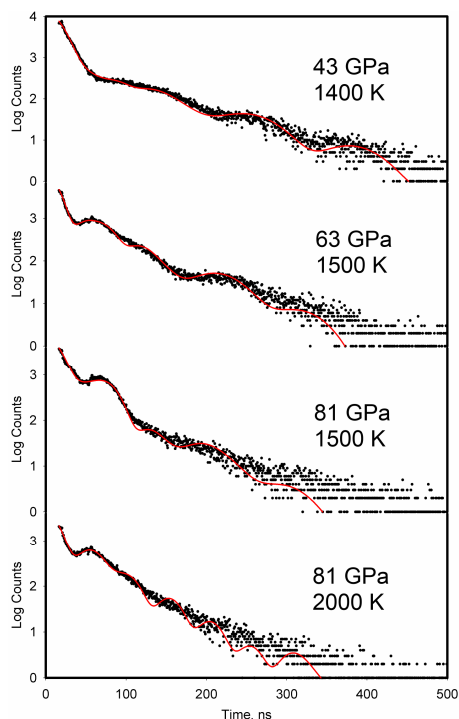

Fig. 5.2.8.1. High-pressure NFS spectra of $Mg_{0.83}Fe_{0.21}Al_{0.06}Si_{0.91}O_3$ perovskite at high temperature showing an alternative fit to the spectra. The solid red lines show the theoretical fits.

5.3   Oxidation state of the lower mantle: *in situ* observations of the iron electronic configuration in magnesium silicate perovskite at extreme conditions

I. Kupenko[a,b], C. McCammon[b], R. Sinmyo[b], V. Cerantola[b], V. Potapkin[c], A.I. Chumakov[a], A. Kantor[a], R. Rüffer[a], L. Dubrovinsky[b]

[a] *European Synchrotron Radiation Facility, CS 40220, 38043, Grenoble, Cedex 9, France*

[b] *Bayerisches Geoinstitut Universität Bayreuth, D-95440 Bayreuth, Germany*

[c] *Jülich Centre for Neutron Science JCNS und Peter Grünberg Institut PGI JCNS-2, D-52425 Juelich, Germany*

5.3.1   Abstract

We have investigated the electronic configuration of iron in Fe-, Al-containing magnesium silicate perovskite, the main component of the lower mantle, at conditions of the deep Earth's interior using the energy domain Synchrotron Mössbauer Source (SMS) technique. We show that the high ferric iron content observed previously in quenched samples is preserved at high temperatures and high pressures. Our data are consistent with high-spin to intermediate-spin (HS-IS) crossover in Fe^{2+} at high pressures and ambient temperature. We see no evidence of spin crossover in Fe^{3+} occupying the A-position of silicate perovskite. On laser heating at pressures above ~ 40 GPa we observe a new doublet with relative area below 5% which likely corresponds to Fe^{3+} in the octahedral (B-site) position in silicate perovskite. We conclude that at lower mantle conditions Fe^{3+} remains predominantly in the HS state, while Fe^{2+} occurs solely in the IS state.

5.3.2   Introduction

$MgSiO_3$ perovskite that contains Fe and Al (hereafter FeAlPv) is considered to be the most abundant phase in the Earth and to constitute roughly 75% of the lower mantle (e.g., Irifune et al., 2010; Ringwood, 1982). Iron can occur in both ferrous (Fe^{2+}) and ferric (Fe^{3+}) forms in FeAlPv. In contrast to phases in the upper mantle, the amount of ferric iron in FeAlPv is expected to be high (Frost et al., 2004; McCammon, 1997), but until now all estimations of $Fe^{3+}/\Sigma Fe$ in the lower mantle have been based on measurements at room temperature from quenched samples.

The spin state of iron in FeAlPv in different valence states may affect the thermodynamic properties, electrical and thermal conductivities, and other properties of the Earth's interior (e.g., Frost et al., 2004; Goncharov et al., 2008; Potapkin et al., 2013). Many studies have been performed to determine the spin state of Fe in FeAlPv, but the conclusions reached are not uniform. Interpretation of spectra is complicated by the presence of two sites in the orthorhombic (CdFeO$_3$-type) perovskite structure: a large distorted 8- to 12-coordinated site, hereafter referred to as "A", and a smaller relatively undistorted octahedral site, hereafter referred to as "B". Ferrous iron occupies the A-site exclusively and was reported to exhibit a spin crossover from the high-spin (HS) to the intermediate-spin (IS) state (Kupenko et al., 2014; Lin et al., 2008; McCammon et al., 2008; Potapkin et al., 2013). However, all computational studies have found the HS configuration of Fe^{2+} to be the most stable (e.g., Hsu et al., 2012; Zhang and Oganov, 2006) and attribute the experimentally observed pressure-induced changes in hyperfine parameters of ferrous iron to small changes in its local environment (Hsu et al., 2012). Ferric iron was reported to occupy either exclusively the A-site and to be in the HS state (Kupenko et al., 2014; McCammon et al., 2008; Potapkin et al., 2013) or to occupy both A- and B-sites with Fe_A^{3+} remaining in the HS state at lower mantle conditions and Fe_B^{3+} exhibiting HS to low-spin (LS) crossover at pressures around 50 GPa (Catalli et al., 2011). Several studies have additionally proposed that high pressures and high temperatures may promote the site exchange of Fe^{3+} and Al^{3+} by the reaction (HS Fe_A^{3+})+Al_B^{3+}→(LS Fe_B^{3+})+Al_A^{3+} (Catalli et al., 2011; Fujino et al., 2012).

The majority of previous reports describing the spin state behavior in FeAlPv at lower mantle conditions are based on analysis of temperature-quenched samples (Catalli et al., 2011; Fujino et al., 2012; Li et al., 2004; Potapkin et al., 2013). An indication of the temperature effect to stabilize IS Fe^{2+} relative to HS Fe^{2+} was provided by McCammon et al. (2008); however, in their study the temperature was limited to only 1000 K. More recent results based on Nuclear Forward Scattering (NFS) (Kupenko et al., 2014) extended temperatures to lower mantle conditions. However, NFS is not well suited to materials with a large number of components arising from multiple sites, valence states and spin states (which is the case for FeAlPv), which leads to spectral complexity and non-uniqueness of fitting models. Energy-domain Mössbauer spectroscopy (MS) is better suited for the analysis of iron distribution between individual structural sites in FeAlPv, and its oxidation and electronic states (McCammon et al., 2008; Potapkin et al., 2013). However, studies of lower mantle phases at the relevant high pressure and temperature conditions are not possible using conventional MS

with a radioactive source due to the challenge of focusing gamma rays in the laboratory. The recently developed Synchrotron Mössbauer Source (SMS) allows measurements of high quality and well resolved energy domain spectra on timescales of only a few hours, combining the advantages of synchrotron radiation and MS technique (Potapkin et al., 2012).

In this paper we present a high-pressure high-temperature study of FeAlPv using the SMS technique to elucidate the electronic configuration of iron *in situ* at lower mantle conditions in order to constrain the properties of the most abundant phase in the most voluminous shell within the Earth.

5.3.3 Methods

The FeAlPv sample used in the present study was from the same synthesis run as used by Potapkin et al. (2013), Kupenko et al. (2014), and Sinmyo et al. (2014). It was synthesized in the multianvil press from a mixture of MgO, SiO_2, Al_2O_3, $^{57}Fe_2O_3$ (90% enriched) starting materials in a rhenium capsule at 26 GPa and 1800°C for 30 min. Before synthesis, the starting materials were heated at 973 K for 1 day in a H_2-CO_2 gas-mixing furnace, in which oxygen fugacity was controlled at $\log fO_2 = -21$ to reduce Fe^{3+} to Fe^{2+}. After the multianvil experiment, the recovered sample was characterized at ambient conditions using the electron microprobe (JEOL, JXA-8200, under the operating conditions 15 kV and 15 nA). Electron microprobe analysis on the sample used for the present study showed the chemical composition to be $Mg_{0.832(21)}Fe_{0.209(22)}Al_{0.060(2)}Si_{0.916(24)}O_3$, which is the same within measurement accuracy to those of the samples used by Potapkin et al. (2013), Kupenko et al. (2014), and Sinmyo et al. (2014). However the $Fe^{3+}/\Sigma Fe$ ratio measured for the present FeAlPv sample using Mössbauer spectroscopy (35±5%) is intermediate between the values measured for the samples of Potapkin et al. (2013) (50±5%) and Kupenko et al. (2014) (20%±3%). This difference is likely due to a temperature dependence of the $Fe^{3+}/\Sigma Fe$ ratio (as reported, for example, by Frost et al., 2004) coupled with temperature gradients in the multianvil assembly, as it is expected that the region of the sample in the center of the assembly is hotter than the part of the sample at the edges.

For high-pressure generation cylindrical-type BX-90 diamond anvil cells (DAC) (Kantor et al., 2012) were used that were mounted with 250 μm culets diamonds. A 200 μm thick Re gasket was pre-indented to about 30 μm thick and a 125 μm hole was drilled in the centre. A thin layer (about 5 to 7 μm thick) of polycrystalline FeAlPv with composition as given above

was loaded in the gasket at room pressure and temperature and afterwards Ne was loaded at 1.2 kbar (Kurnosov et al., 2008) as a pressure medium and thermal insulator. The pressure was determined by the ruby fluorescence method.

High temperature measurements were performed using a modified version of the portable double-sided laser-heating system (Dubrovinsky et al., 2010, 2009; Kupenko et al., 2012b). Two infrared fiber lasers were focused to ~ 40 μm full width at half maximum (FWHM). The system implements π-shapers (Prakapenka et al., 2008) that convert an initial Gaussian-shaped beam to one with a flat top distribution. The surface temperature was measured by the standard spectroradiometry method (Shen et al., 2010) using an Acton SP2300 spectrometer (Princeton Instruments) with a PIXIS400 CCD detector.

SMS spectra were recorded at the Nuclear Resonance Beamline (Rüffer and Chumakov, 1996) ID18 of the European Synchrotron Radiation Facility using the (111) Bragg reflection of a ^{57}FeBO3 single crystal mounted on a Wissel velocity transducer driven with a sinusoidal wave form (Potapkin et al., 2012). The X-ray beam was focused to 20 μm vertical and 10 μm horizontal dimensions using Kirkpatrick-Baez mirrors. The linewidth of the SMS and the absolute position of the centre shift (CS) was controlled before and after each measurement using a $K_2Mg^{57}Fe(CN)_6$ reference single line absorber. The velocity scale was calibrated using 25 μm thick natural α-Fe foil. Each spectrum took ~ 1-2 hours to collect. The spectra were fitted using a full transmission integral with a normalized Lorentzian-squared source lineshape using the MossA software package (Prescher et al., 2012). Room temperature spectra were collected from 12 to 77 GPa. After 39 GPa the sample was laser heated at ~ 2000 K (measured by the spectroradiometry method) at each pressure step to relax stress and spectra were collected before, during, and after heating.

5.3.4   Results

At low pressure and ambient temperature the spectra consist of two main absorption features with a shoulder in between (Fig. 5.3.4.1) that can be fitted with two doublets that correspond to HS Fe^{2+} and HS Fe^{3+} according to their hyperfine parameters (Fig. 5.3.4.2). Upon pressure increase a new doublet begins to emerge above ~ 40 GPa and becomes well resolved above 52 GPa (Fig. 5.3.4.1). The doublet has extremely high quadrupole splitting (QS) and is similar to the component reported in previous studies (Kupenko et al., 2014; McCammon et al., 2008; Potapkin et al., 2013). Upon pressure increase the abundance of the new high QS component grows at the expense of the doublet corresponding to HS Fe^{2+}. After heating of
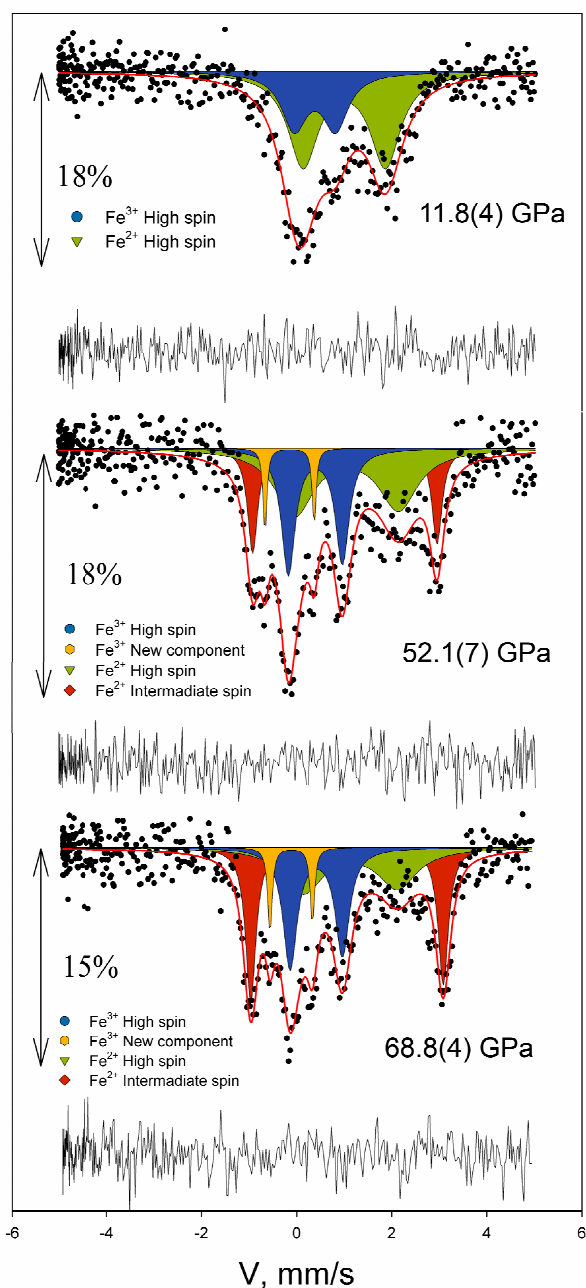
Fig. 5.3.4.1. Selected high-pressure SMS spectra of $Mg_{0.83}Fe_{0.21}Al_{0.06}Si_{0.92}O_3$ perovskite at room temperature. The solid lines show the theoretical fit, the arrows show the amount of absorption and the residual is indicated below each spectrum. After 39 GPa the sample was laser heated at ~ 2000 K at each pressure step.

the sample at ~ 40 GPa and ~ 2000 K (as measured by spectroradiometry) another new doublet was observed with narrow linewidth (FWHM ~ 0.1 mm/s), relatively low CS (~ –0.2 mm/s) and QS (~ 0.9 mm/s) (Fig. 5.3.4.1). The CS of the new narrow doublet remains almost unchanged at pressures up to 77 GPa (Fig. 5.3.4.2). The relative area of the narrow doublet

remained below ~ 5% in all of our experiments (Fig. 5.3.4.2), and its first appearance at 40 GPa and slight increase of intensity upon re-heating of the sample at higher pressures correlate clearly with a decrease in the relative area of the HS Fe^{3+} component by a similar amount. The hyperfine parameters of all components (without considering the low CS Fe^{3+} doublet) are consistent with previously reported values from energy domain Mössbauer spectroscopy studies (reviewed by McCammon et al., 2013).
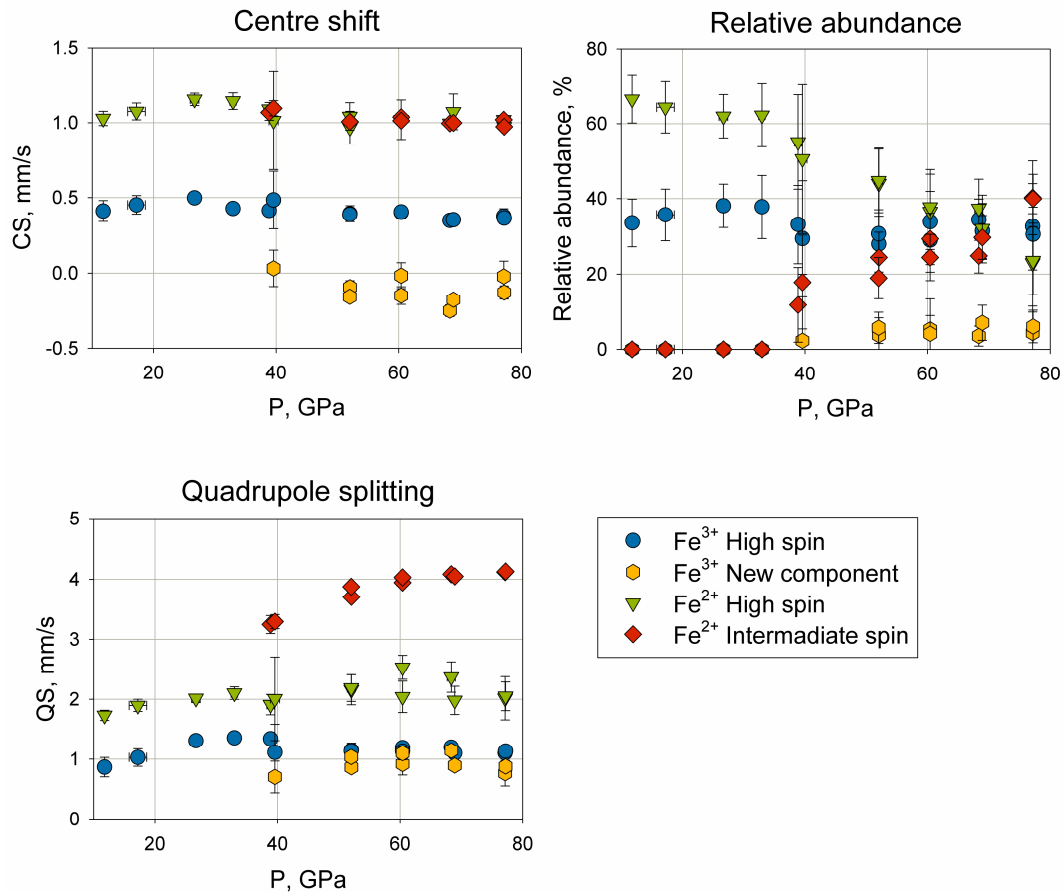
Fig. 5.3.4.2. Effect of pressure on the hyperfine parameters of $Mg_{0.83}Fe_{0.21}Al_{0.06}Si_{0.92}O_3$ perovskite at room temperature. After 39 GPa the sample was laser heated at ~ 2000 K at each pressure step.

At high temperature the CS values of the Mössbauer components provide the novel possibility of an internal thermometer to probe the mean temperature of the sample independently of the spectroradiometry measurements. The latter show only the highest temperature of the sample surface and therefore tend to overestimate temperature (e.g., Campbell et al., 2007). There are two main contributions to the CS – the isomer shift and the second order Doppler shift (SOD) (e.g., Greenwood and Gibb, 1971). The SOD varies approximately linearly with temperature for both Fe^{2+} and Fe^{3+} components in the high-temperature Debye limit (Housley and Hess, 1966), which can be estimated as $\Delta v = -7.3 \cdot 10^{-4}$

mm/s/K. Although we made an effort to prepare samples that were thin (about 5 to 7 µm thick), the high temperature SMS spectra show a superposition of components that can be modeled as absorption arising from hotter and cooler (hereafter referred to as "warm") material (Fig. 5.3.4.3) (Kupenko et al., 2012b; see also Supplementary Information for additional discussion).
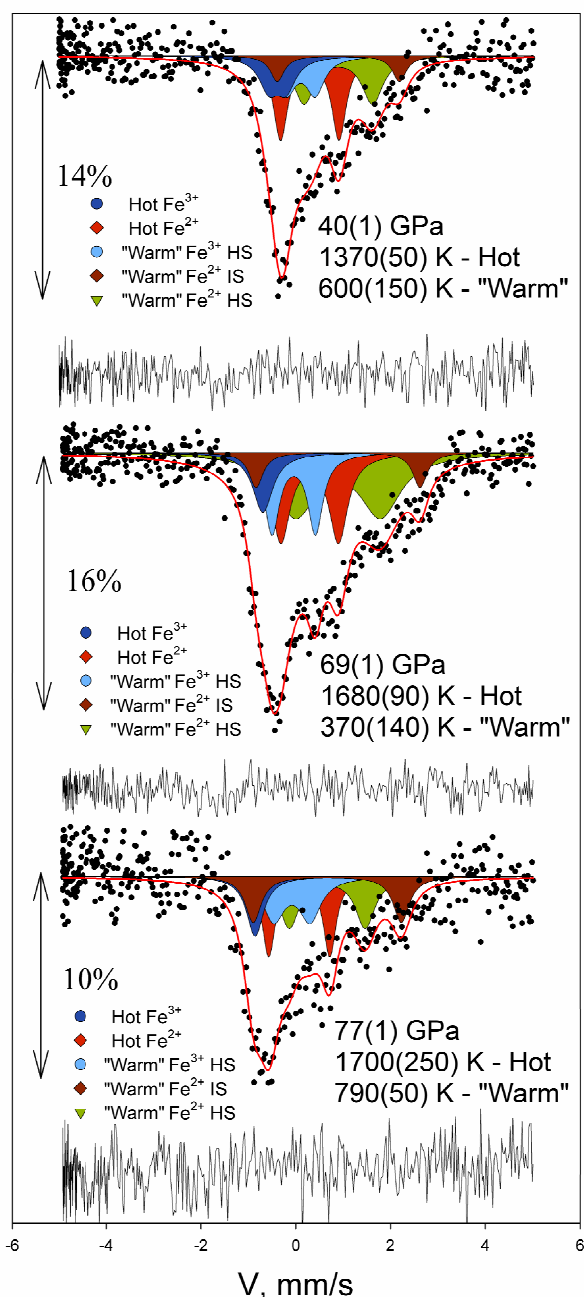
Fig. 5.3.4.3. Selected SMS high-pressure spectra of $Mg_{0.83}Fe_{0.21}Al_{0.06}Si_{0.92}O_3$ perovskite at high temperature. Due to nonhomogeneous heating the spectra show a superposition of absorption arising from hotter and cooler (referred to as "warm") material. Temperatures were determined from the shift of the CS values. HS: high-spin; IS: intermediate-spin.

Temperatures were determined independently from the shifts of CS for Fe^{2+} and Fe^{3+} for both the hot and "warm" components of the spectra. Consistent results were obtained and the standard deviation of the temperature determination did not exceed ±250 K and ±160 K for the hot and "warm" regions, respectively. The hot components of the spectra consist of two doublets that can be assigned to Fe^{2+} and Fe^{3+}. The "warm" components of the spectra consist of the same components as at ambient temperature: two doublets corresponding to Fe^{2+} (low QS and high QS) and one Fe^{3+} doublet. It is not possible to resolve the low CS Fe^{3+} doublet likely due to its low abundance and the presence of temperature gradients that reduce resolution. For both the hot and "warm" regions, all components show a decrease of QS and CS relative to the values at ambient temperature (Fig. 5.3.4.4).
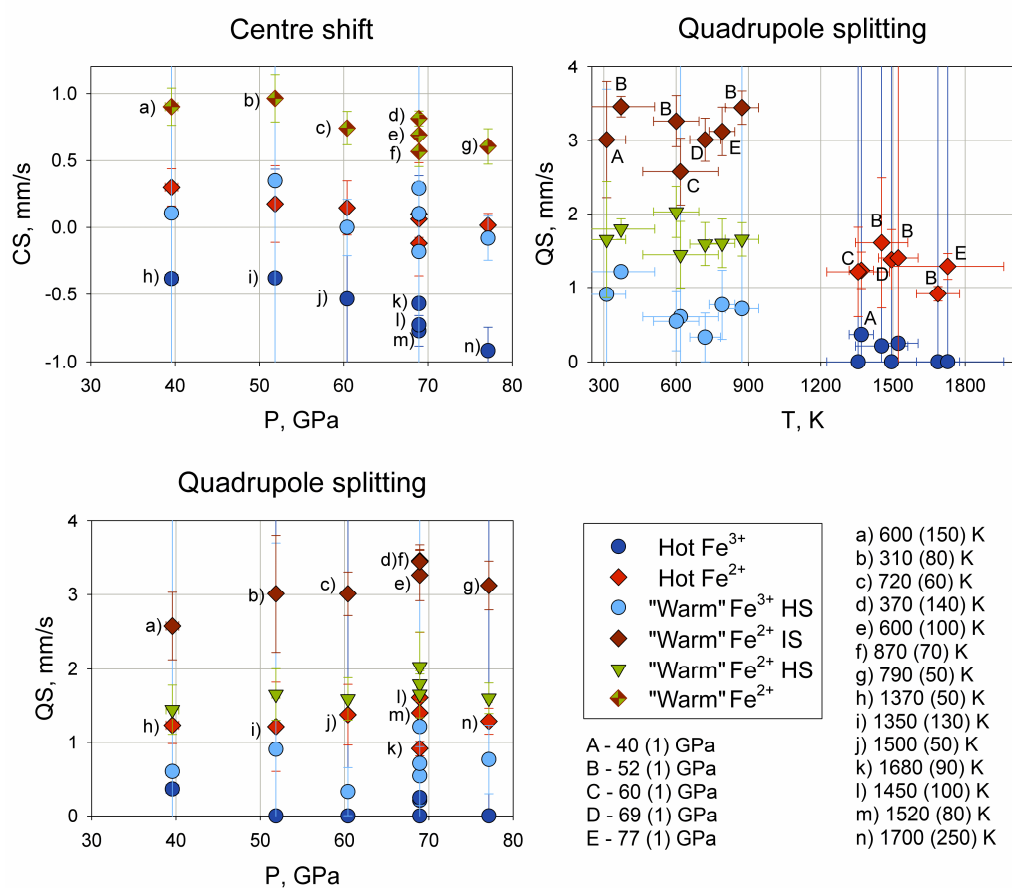
Fig. 5.3.4.4. Effect of pressure and temperature on the hyperfine parameters of $Mg_{0.83}Fe_{0.21}Al_{0.06}Si_{0.92}O_3$ perovskite. Due to nonhomogeneous heating two sets of data are presented arising from hotter and cooler (referred to as "warm") material. Temperatures were determined from the shift of the CS values.

5.3.5 Discussion

A. Fe^{3+} high pressure behavior

Chemical composition based on electron microprobe data, Mössbauer spectroscopy at ambient conditions, and previous single crystal X-ray diffraction data of FeAlPv (Glazyrin et al., 2014; Kupenko et al., 2012b; Vanpeteghem et al., 2006) lead to a crystal chemical formula for the sample used in this study of $(Mg_{0.832(21)}Fe^{2+}_{0.136(14)}Fe^{3+}_{0.073(7)})(Al_{0.060(2)}Si_{0.916(24)})O_3$. Charge balance and site occupancy considerations indicate that for this material synthesized at 26 GPa in a multi-anvil apparatus, the A-site is completely occupied by magnesium, ferrous and ferric iron, and the B-site contains 0.024 ± 0.024 vacancies per formula unit.

Our data show no significant change in the hyperfine parameters of the dominant Fe^{3+}_A doublet with increasing pressure at room temperature (Figs. 5.3.4.1, 5.3.4.2), indicating that no spin transition in that component occurs. However, heating at 40 GPa in the DAC results in a decrease in the relative area of the doublet associated with Fe^{3+}_A and the appearance of a new Fe^{3+} doublet with low CS that we may assign to ferric iron on the B-site (Fe^{3+}_B). This assignment leads to the (approximate) crystal chemical formula $(Mg_{0.832}Fe^{2+}_{0.136}Fe^{3+}_{0.063})(Al_{0.060}Si_{0.916}Fe^{3+}_{0.01})O_3$, which is within the uncertainty of the chemical analysis. Rapid saturation of the change in the relative area of Fe^{3+}_B with increasing pressure suggests that the occupation of the B-site by ferric iron is controlled by the number of defects arising from synthesis of the sample at 26 GPa, rather than as the result of an exchange reaction involving Al^{3+} (Catalli et al., 2011; Fujino et al., 2012). We note that high-pressure high-temperature single crystal diffraction studies of FeAlPv with different compositions (Dubrovinsky et al., 2010; Glazyrin et al., 2014; Kupenko et al., 2012b) firmly exclude the presence of Al on the A-site, while a few percent of Fe^{3+} on the B-site would be hardly detectable by X-ray diffraction methods.

The observed QS of the Fe^{3+}_B component (~ 1 mm/s) is much lower than the values reported in previous NFS studies (Catalli et al., 2011, 2010; Lin et al., 2012) for LS ferric iron in the B-site (~ 2.7-3.5 mm/s). At the same time the hyperfine parameters (QS and CS) of Fe^{3+}_B are in excellent agreement with values reported for LS Fe^{3+} in octahedral oxygen coordination in the high-pressure phases of FeOOH (Xu et al., 2013) and $CaFe_2O_4$ (Greenberg et al., 2013). Thus, we conclude that Fe^{3+}_B is in the LS state already at about 40 GPa.

The difference of our results to those reported earlier (Catalli et al., 2011; Fujino et al., 2012) may arise due to different methodologies used in sample preparation and chemical composition characterization. The composition of FeAlPv in earlier studies (Catalli et al., 2011; Fujino et al., 2012) were assumed to be the same as the starting glass or the low-pressure phases that were loaded into the DAC and eventually transformed into FeAlPv by laser heating at high pressure. Our present study shows clearly that chemical composition and particularly $Fe^{3+}/\Sigma Fe$ of FeAlPv depend on the conditions of synthesis and thermal history, and are not always equivalent to the starting material. We do not observe any high QS component in our Mössbauer spectra with a CS that can be attributed to Fe^{3+}; hence we suggest that one possibility for the high QS component reported by (Catalli et al., 2011, 2010) is the presence of some Fe^{2+} in their samples.

The data collected during the laser heating confirm that a large proportion of ferric iron in FeAlPv, observed previously in the quenched samples (Frost et al., 2004; McCammon, 2005, 1997), is preserved at the lower mantle conditions. However, our data show that only a small amount of LS Fe^{3+}_B is present in a composition of FeAlPv relevant for the Earth's lower mantle, which does not increase upon heating. We see no evidence of a spin change involving Fe^{3+}_A, but only a decrease of QS and CS values due to temperature that is consistent with previous NFS data (Kupenko et al., 2014). We, therefore, conclude that HS-LS crossover in Fe^{3+} plays a negligible role in determining the properties of the deep Earth, while at the same time changes in the type and distribution of vacancies (e.g., in the A- and B-sites) may significantly influence elastic properties of FeAlPv and, hence, the geochemistry of the Earth's lower mantle, in particular in its upper part.

B. Fe^{2+} spin crossover

The nature of the new Fe^{2+} component with extremely high QS continues to be a matter of strong debate. Ab initio computations predict that Fe^{2+} remains in the HS state at all mantle pressures (Hsu et al., 2010; Stackhouse et al., 2007; Umemoto et al., 2010; Wentzcovitch et al., 2012; Zhang and Oganov, 2006) and attribute the high QS Fe^{2+} component to different stable local atomic configurations of HS Fe^{2+}_A. Indeed Mössbauer studies have shown the presence of two different HS Fe^{2+} environments where the doublet with higher QS becomes more stable at both reduced temperature and higher pressure as predicted by theory (Lauterbach et al., 2000; McCammon, 1994); however the experimentally observed QS value of the latter doublet lies well below that of the new high QS Fe^{2+} component.

Table 5.3.5.1 summarizes all experimental data available from NFS, MS and X-ray emission spectroscopy (XES) for FeAlPv from studies where iron occurs predominantly as Fe^{2+}. There is a large variation in the pressure range over which the high QS Fe^{2+} component dominates the NFS and MS spectra, likely due to technical issues such as differences in non-hydrostatic stress and pressure gradients between studies, which has undoubtedly contributed to the controversy. However, there are several features that are common to all studies. All XES spectra show a drop in the Kβ' line intensity and a shift of the $K\beta_{1,3}$ line energy that imply a drop in the average quantum spin number according to conventional data analysis. All NFS and MS spectra show the appearance of the high QS Fe^{2+} component at moderately low pressures (< 50 GPa) with increase in its contribution to the spectra with increasing pressure and increasing temperature. While hyperfine parameters derived from NFS and MS spectra do not provide unequivocal identification of spin state, their values and trends with pressure and temperature enable changes in spin state to be clearly identified. All of the experimental data available from XES, NFS and MS methods are consistent with assignment of the high QS component at high pressures and ferrous component at high temperatures to IS Fe^{2+} (Table 5.3.5.1).

C. Reevaluation of previous NFS spectra

The current study using the SMS technique enables a reevaluation of NFS data collected on a similar sample at similar conditions. The new low CS Fe^{3+} component has a low abundance and cannot be resolved with the low brilliance of a conventional radioactive MS source. The time domain representation of the low CS Fe^{3+} component is a weak low frequency modulation of the main pattern and is also undetectable. The new SMS data enable the component to be clearly resolved, which provides a more accurate measure of cation distribution. We are, therefore, able to reevaluate and improve the fitting model proposed in Kupenko et al. (2014). Both the conventional MS and NFS data from Kupenko et al. (2014) can be fitted with the model proposed in the current study. Notably, the refitted NFS spectra also confirm the presence of the additional Fe^{3+} component with about 5% abundance (Supplementary Information).

NFS data show that HS-IS spin crossover of Fe^{2+} takes place over an extremely narrow pressure range regardless of the fitting model. Kupenko et al. (2014) attributed the differences of NFS and MS spin crossover pressure ranges to pressure gradients inside the DAC. SMS data were collected at the same conditions as NFS data on the same beamline and

therefore should show similar results; however, SMS data indicate a much broader pressure range for HS-IS crossover. In order to resolve this inconsistency we looked to fundamental properties of the NFS technique. In the time domain representation the FWHM of the corresponding lines in absorption spectra determines the decay rate of the corresponding beats. A time window of NFS spectra is gated to exclude electronic scattering of a synchrotron X-ray beam, which appear at early time of the spectra and, therefore, cuts off the initial part of the quantum beats. The FWHM of the HS Fe^{2+} component is the highest among the all components (Fig. 5.3.4.1) and its main contribution should, therefore, appear in the gated region. The FWHM of the HS Fe^{2+} doublet increases with pressure, which amplifies the effect. As a result the component cannot be detected (or is difficult to detect) at high pressures. Our results clearly show the disadvantage of the NFS technique for studies of multi component systems with a high dispersion of component linewidths.

The NFS high temperature data from Kupenko et al. (2014) show only a limited number of spectral features and therefore a unique fit is not possible. However, the results from the current SMS high temperature study enable a more complex (but realistic) fitting model to be applied. We observe that the five-doublet fit for SMS spectra reported in the current study significantly improves the quality of the fits to the NFS high temperature spectra (Supplementary Information). The energy-domain representation provided by SMS enables a high temperature fitting model to be determined that consistently fits the data collected by the two different techniques.

5.3.6 Conclusions

Our in situ Mössbauer spectroscopy measurements at pressures up to ~80 GPa and temperatures above 1700 K have unambiguously established the valence and spin states of iron in Fe-, Al-bearing silicate perovskite at lower mantle conditions. Our data confirm the conclusions based on the studies of quenched samples that a large proportion of iron in FeAlPv in the lower mantle is in the ferric state (Frost et al., 2004; McCammon, 2005, 1997). We see no evidence of a spin change involving Fe_A^{3+}, neither at high pressures nor at high temperatures. The abundance of Fe_B^{3+} is on the order of 5% of total iron content and probably below the detection limits of methods other than energy domain Mössbauer spectroscopy. The low amount of Fe_B^{3+} at lower mantle conditions suggests that spin crossover of Fe^{3+} does not affect the properties of FeAlPv in the deep Earth's interior. All previous experimental data (XES, NFS, MS) of FeAlPv are consistent with HS-IS crossover of Fe^{2+} and high

Table 5.3.5.1. Summary of experimental data that provide information about the Fe^{2+} electronic state in $(Mg,Fe)SiO_3$ and $(Mg,Fe)(Si,Al)O_3$ perovskite at high pressure and/or high temperature.

Reference	Method	Experimental observation	Interpretation based on the present study
Badro et al. (2004)	XES	S ~ 2 at 30 GPa and RT; S ~ 1 at 70 GPa and RT	all Fe^{2+} is HS at 30 GPa; all Fe^{2+} is IS at 70 GPa
Li et al. (2004)	XES	S drops from 2 to ~ 1 continuously on compression from 30 to 100 GPa at RT	IS Fe^{2+} first appears at 30 GPa and gradual HS-IS crossover takes place with increasing pressure that is complete by 100 GPa
Lin et al. (2008)	XES	S ~ 1 at 108 GPa and RT and remains constant with heating up to 3000 K	all Fe^{2+} is IS at 108 GPa and remains stable with heating up to at least 3000 K
Lin et al. (2010)	XES	S ~ 1 at 120 GPa and RT; S increases to ~ 1.5 on decompression to 60 GPa and RT	all Fe^{2+} is IS at 120 GPa and partially reverts to HS Fe^{2+} on decompression to 60 GPa
Jackson, (2005)	NFS	Appearance of high frequency component (high QS doublet) at ~ 40 GPa and RT; contribution increases on compression but does not visually dominate spectrum even at 120 GPa	IS Fe^{2+} first appears at 40 GPa and gradual HS-IS crossover takes place with increasing pressure that is not complete by 120 GPa
Li et al. (2006)	NFS	Appearance of high QS doublet at ~20 GPa and RT; contribution increases on compression but does not visually dominate spectrum even at 100 GPa	IS Fe^{2+} first appears at 40 GPa and gradual HS-IS crossover takes place with increasing pressure that is not complete by 100 GPa
Lin et al. (2008)	NFS	High QS doublet dominates spectrum at 110 GPa and RT	all Fe^{2+} is IS at 110 GPa
McCammon et al. (2008); Narygina et al. (2010)	NFS, MS	Appearance of high QS doublet at ~ 30 GPa and RT; contribution increases with both compression and heating; doublet visually dominates NFS spectra at 110 GPa and constitutes 100% of Fe^{2+} absorption at 110 GPa in MS spectra	IS Fe^{2+} first appears at ~ 30 GPa and HS-IS crossover takes place with increasing pressure up to 60-80 GPa where it is then complete; IS Fe^{2+} proportion increases with heating up to at least 1000 K
Grocholski et al. (2009)	NFS	High QS doublet present at 50 and 65 GPa at RT but does not dominate spectrum	Some IS Fe^{2+} is present at 50 and 65 GPa but other components and/or phases are also present
Lin et al. (2012)	NFS	Appearance of high QS doublet at ~24 GPa and RT; contribution increases on compression and visually dominates spectrum by ~ 60 GPa with minimal change up to 110 GPa	IS Fe^{2+} first appears at 24 GPa and HS-IS crossover takes place with increasing pressure up to ~60 GPa and IS Fe^{2+} proportion remains approximately the same up to 110 GPa
Kupenko et al. (2014)	NFS, MS	Appearance of high QS doublet at ~ 35 GPa and RT; contribution increases with both compression and heating but pressure for completion is different for the NFS (~50 GPa) than for the MS (>90 GPa) experiment	IS Fe^{2+} first appears at ~ 35 GPa and HS-IS crossover takes place with increasing pressure to completion more rapidly in the NFS experiment likely due to fundamental properties of the NFS technique (see Discussion subsection 3). IS Fe^{2+} proportion increases with heating up to at least 2000 K

S: average quantum spin number; RT: room temperature; XES: X-ray emission spectroscopy; MS: Mössbauer spectroscopy (energy domain); NFS: Nuclear forward scattering; IS: intermediate-spin; HS: high-spin; QS: quadrupole splitting.

temperature data show that the IS state is stabilized relative to the HS state at high pressures and high temperatures. We therefore conclude that FeAlPv in the lower mantle contains predominantly IS Fe^{2+} and HS Fe^{3+}. Further examination of the relations between the $Fe^{3+}/\Sigma Fe$ ratio, the type and distribution of vacancies in FeAlPv, and the synthesis conditions is necessary in order to elucidate their possible effects on the elastic and transport properties of Fe-, Al-bearing silicate perovskite at conditions of the deep Earth's interior.

5.3.7 Acknowledgments

5.3.8 Supplementary information

A. Refitting of nuclear forward scattering (NFS) spectra

The outstanding energy resolution of Synchrotron Mössbauer Source (SMS) spectra enables improved fitting of the Kupenko et al. (2014) high temperature nuclear forward scattering (NFS) spectra, and also the opportunity to verify the consistency of their conventional radioactive source Mössbauer spectroscopy (MS) spectra with the fits proposed in the present paper. At room temperature addition of the new low CS Fe^{3+} doublet provides consistent fits of the MS spectra (Fig. 5.3.8.1a) and the NFS spectra (Fig. 5.3.8.1b). The original fits to the high temperature NFS spectra of Kupenko et al. (2014) assuming a uniform temperature of the entire sample show some deviations from the experimental data (Fig. 5.3.8.2a), while the new fits incorporating nonhomogeneous heating as derived in the present paper provide an excellent model of the data (Fig. 5.3.8.2b).

B. Thermal gradients in laser-heated DAC experiments

The temperature gradient observed in SMS spectra collected from laser-heated diamond anvil cell (DAC) experiments is likely the result of nonhomogeneous thermal isolation of the powder sample. Diamond has a high thermal conductivity; therefore, small deviations in thickness of the thermal insulation between the diamonds and the sample result in significant variation in the quality of the heating. We observed several places on the sample that could

be well heated but a shift in position of 5-10 µm may result in a substantial reduction of temperature at the same laser power. Defocusing of the laser beam did not result in any change of the heating spot size. An increase of the laser power allowed the spot to reach higher temperatures but did not noticeably change the size of the spot. We compared the size of the laser heated spot with that of the X-ray beam in our experiment. The size of the X-ray beam was measured to be 20 vertical µm by 10 horizontal µm, while a rough estimation of the heated spot size based on correction of the relative areas of the hot and "warm" subspectra with the difference in the recoil-free fraction lead to a diameter in the range of 7-10 µm. Our results demonstrate the importance of sample preparation considerations for experiments involving laser heating in the DAC coupled with X-ray techniques using a large beamsize.
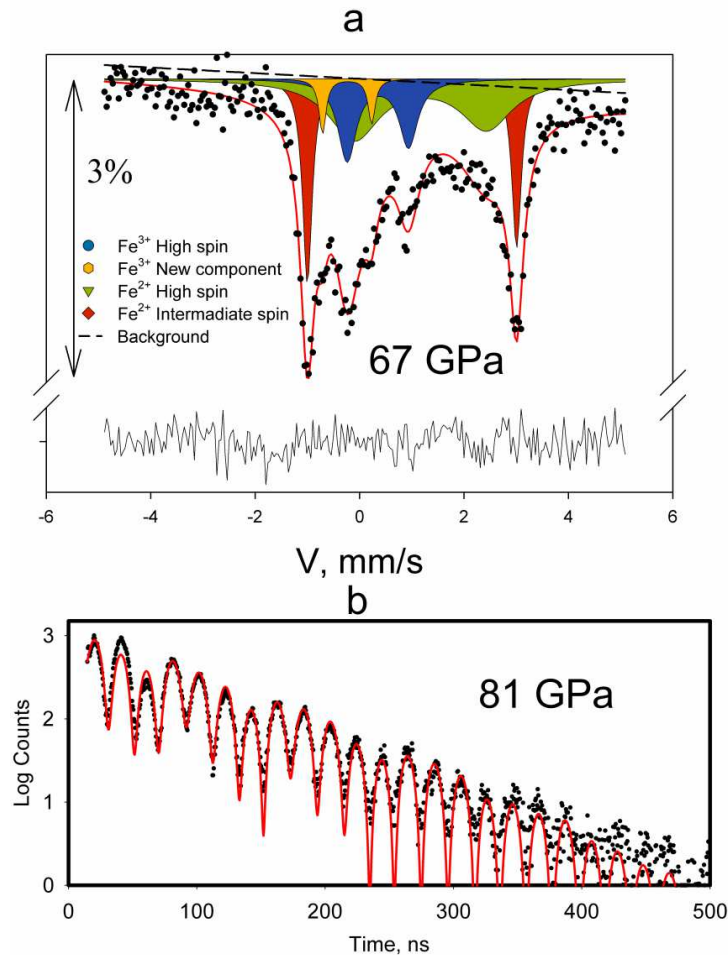

Fig. 5.3.8.1. High-pressure spectra of $Mg_{0.83}Fe_{0.21}Al_{0.06}Si_{0.92}O_3$ perovskite at room temperature reported in Kupenko et al. (2014) fitted with the model from the current paper. The solid lines show the theoretical fits. a) Conventional radioactive source Mössbauer spectrum; b) NFS spectrum. The arrows indicate the degree of absorption in the Mössbauer spectrum and the residual of the fit is indicated below the spectrum.
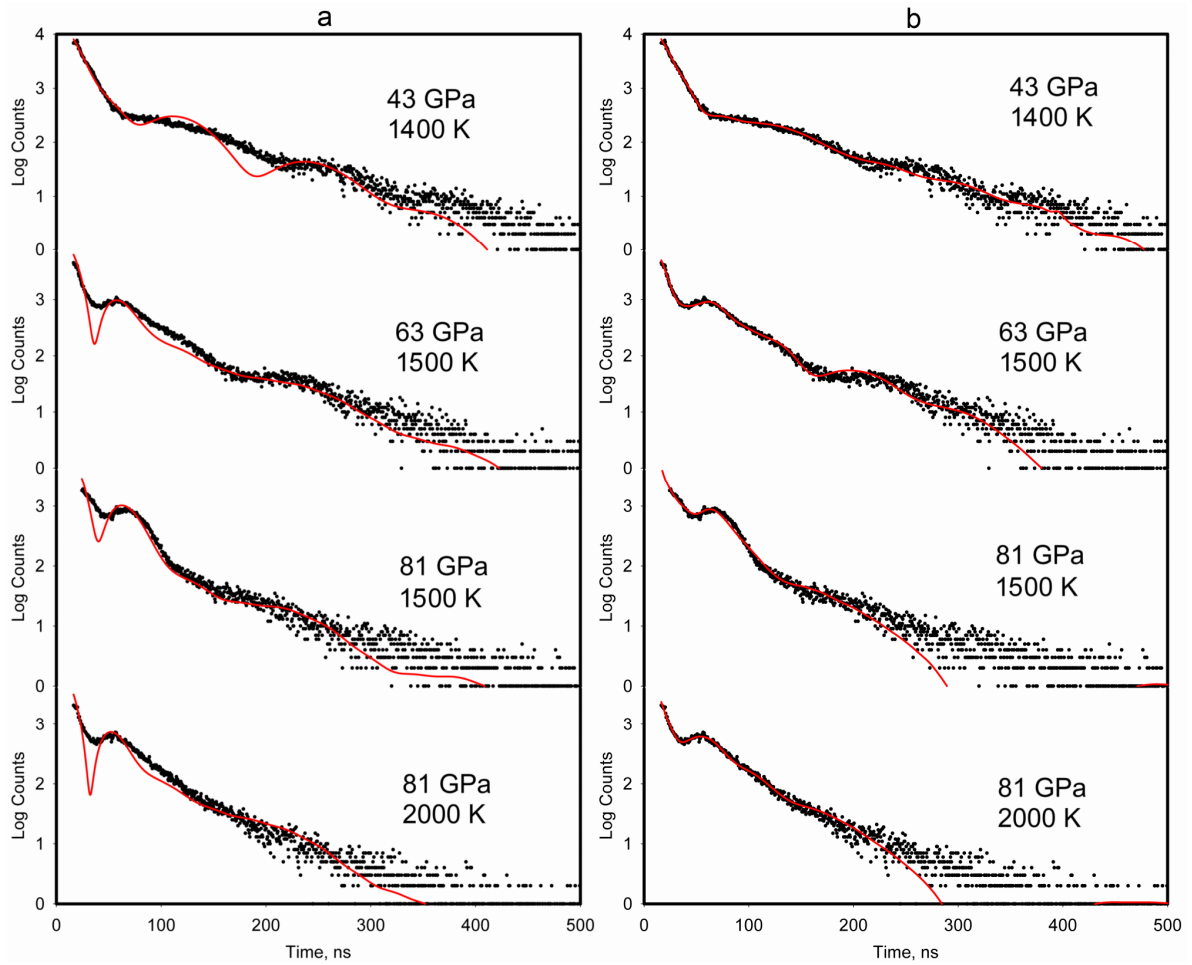
Fig. 5.3.8.2. Comparison of the (a) original fits with the (b) new fits to the high-pressure high-temperature NFS spectra of $Mg_{0.83}Fe_{0.21}Al_{0.06}Si_{0.92}O_3$ perovskite reported by Kupenko et al. (2014). The fits in part (b) correspond to the ones derived from the SMS spectra as described in the main text of the present paper. The indicated temperatures are those measured using spectroradiometry.

5.4   *In situ* Raman spectroscopic study of the pressure induced structural changes in ammonia borane

Ilya Kupenko[1], Leonid Dubrovinsky[1], Vladimir Dmitriev[2], Natalia Dubrovinskaia[3]

[1]*Bayerisches Geoinstitut, Universität Bayreuth, 95440 Bayreuth, Germany*

[2]*Swiss-Norwegian Beam Line, ESRF, F-38043 Grenoble Cedex, France*

[3]*Material Physics and Technology at Extreme Conditions, Laboratory of Crystallography, Physics Department, Universität Bayreuth, 95440 Bayreuth, Germany*

5.4.1   Abstract

The effect of static compression up to 65 GPa at ambient temperature on ammonia borane (**AB**), BH_3NH_3, have been investigated using in situ Raman spectroscopy in a diamond anvil cells. Two phase transitions were observed at approximately 12 GPa and previously not reported transition at 27 GPa. It was demonstrated that ammonia borane behave differently under compression at quasi-hydrostatic and non-hydrostatic conditions. The ability of BH_3NH_3 to generate second harmonic of the laser light observed up to 130 GPa suggests that the non-centrosymmetric point group symmetry is preserved in the material up to very high pressures.

5.4.2   Introduction

AB is a promising candidate for hydrogen storage due to its remarkably high gravimetric (19.6 wt% H) and volumetric (145 gH L^{-1}) hydrogen content (Blaquiere et al., 2008; Stephens et al., 2007). Hydrogen is irreversibly released from **AB** in 3 steps in the temperature range between 80 and 500 °C with sequential formation of polymeric aminoborane, iminoborane and boron nitride (Baitalow et al., 2002; Baumann et al., 2005; Bowden et al., 2008; Denney et al., 2006; Hu et al., 1978; Storozhenko et al., 2005; Wolf et al., 2000). At ambient conditions **AB** is a soft white powder. It crystallizes into tetragonal structure (space group *I4mm*) with disordered hydrogen (Bowden et al., 2007). The low temperature phase at 255 K was investigated by Raman spectroscopy (Hess et al., 2008) and powder neutron diffraction (Yang et al., 2008) and its properties were studied using ab initio calculations (Song et al., 2012). Numerous investigations were made to examine high-pressure behavior of **AB**, but the results are still controversial

(Chellappa et al., 2009; Chen et al., 2010; Custelcean and Dreger, 2003; Filinchuk et al., 2009; Kumar et al., 2010; Lin et al., 2012, 2008; Nylén et al., 2009; Xie et al., 2009). In some of previous studies phase transitions in **AB** were recognized on pressure dependence of Raman spectra and were reported near 1 GPa (Chellappa et al., 2009; Custelcean and Dreger, 2003; Lin et al., 2008; Nylén et al., 2009; Xie et al., 2009), at 5 GPa (Chellappa et al., 2009; Lin et al., 2008; Nylén et al., 2009; Xie et al., 2009), at 8 GPa (Xie et al., 2009), at 10 GPa (Chellappa et al., 2009; Xie et al., 2009), and at 12 GPa (Lin et al., 2008). The phase transition at 1 GPa was in detail investigated using X-ray diffraction (Chen et al., 2010; Filinchuk et al., 2009; Kumar et al., 2010; Lin et al., 2012) and thermal conductivity measurements (Andersson et al., 2011) and it is identified as a disorder-order phase transition from the tetragonal *I4mm* to orthorhombic *Cmc2$_1$* structure. Meanwhile there is no consensus about behavior of **AB** on compression based on X-ray diffraction data. In the work by Filinchuk et al. (2009) no other transitions were observed up to 12 GPa apart one at 1 GPa, while Kumar et al. (2010) suggested one more transition to the triclinic P1 structure around 8 GPa and no further transitions from 8 up to 27 GPa. In the work by Chen et al. (2010) a phase transition at 5 GPa was reported and no further transformations were detected upon compression up to 23 GPa.. Lin et al. (2012) reported second order isostructural phase transition was around 5 GPa and first order transition to P2$_1$ structure at 13 GPa. Several theoretical calculations were done concerning high pressure phases of **AB** (Andersson et al., 2011; Filinchuk et al., 2009; Lin et al., 2012; Ramzan and Ahuja, 2010; Wang et al., 2011) but again with no consensus.

This study was aimed to improve our understanding of the high-pressure behavior of **AB** that can be very useful in the future design of the storage medium for hydrogen.

5.4.3   Experimental methods

Commercially available crystalline **AB** powder (>97% purity) was purchased from Sigma Aldrich. The purity was checked at ambient conditions by the Raman spectroscopy and X-ray powder diffraction. All observed Raman modes of the starting material were found to be associated with the **AB** so it was used without further purification. High-pressure measurements were carried out using diamond anvil cells (DACs). The diamonds used had 250 µm culets. A 200 µm thick Re gasket was pre-indented to about 30 µm thicknesses and a 125 µm hole was drilled in the centre. Samples were loaded at room temperature. Ne or He as a pressure medium

was loaded at pressure of 1.2 kbar. Some cells were loaded with no pressure transmitting medium. A few ruby balls were placed into the pressure chamber and used as a pressure marker. The pressure was determined with precision of 0.1 GPa by measuring the frequency shift of the ruby R1 fluorescence line (Mao et al., 1986). The pressure was measured before and after each spectra collection. The difference in pressure was not exceeding 0.5 GPa.

One DAC with small culet-size (120 µm) diamonds for investigations in a megabar pressure range was loaded without a pressure medium. In this case the pressure was measured using Raman spectra of diamond itself (Dubrovinskaia et al., 2010).

The Raman spectroscopy was performed by exciting Raman modes using a 514.5 nm Ar^+ ion laser (Coherent Innova 300). The scattered signal was collected in a backscattering geometry and analysed by a T64000 System (Dilor XY) with the liquid nitrogen cooled CCD detector. The 1800 groove/mm grating was used with a final resolution of 0.6 cm^{-1}.

Second harmonic generation (λ=535.44 nm) was realised using the Nd^{3+}:YAG (λ= 1071nm) SPI laser light with a power varied from 5 to 30W in different measurements. The laser beam was focused by MolTech π-shapers and Precitec laser heads (Dubrovinsky et al., 2009). The observation and spectral analysis of the generated light were done using respectively uEye™ usb-cameras and Acton SP2300 spectrometer (Princeton Instruments) with the PIXIS400 CCD detector. The 1200 groove/mm grating was used with a final resolution of 0.032 nm.

All experiments were carried out at room temperature.

5.4.4   Results

C. High pressure Raman spectroscopic measurements on BH_3NH_3

Raman vibrational spectra of **AB** were measured as a function of pressure from 0.8 to over 64 GPa (Fig. 5.4.4.1). At 0.8 GPa all modes of the Raman spectrum can be assigned using factor group analysis (Hess et al., 2008) and they are in good agreement with previous studies (Chellappa et al., 2009; Custelcean & Dreger, 2003; Lin et al., 2008; Xie et al., 2009) (Fig. 5.4.4.1). A broad weak peak at 546 cm^{-1} is assigned as a librational mode (see Chapter 5.4.8 for better resolution). The two weak modes that are assigned as a combination of N-H and B-H rocking deformation modes, ρ(N-B-H), are observed at 738 and 1093 cm^{-1}, respectively. The B-

N stretching manifests itself in two modes, ^{11}B-N, $v(^{11}$B-N), at 803 cm^{-1} and less intensive ^{10}B-N, $v(^{10}$B-N), at 817 cm^{-1}. Two B-H bending modes at 1164 and 1192 cm^{-1} are assigned as symmetric, ω_s(B-H), and asymmetric, ω_{as}(B-H), respectively. The symmetric, ω_s(N-H), and asymmetric, ω_{as}(N-H), N-H bending modes are observed at 1376 and 1596 cm^{-1}. There are symmetric, v_s(B-H), and asymmetric, v_{as}(B-H), B-H stretching modes at 2291 cm^{-1}.and 2382 cm^{-1}, respectively. The N-H stretching vibrations are seen at 3251 cm^{-1} for symmetric, v_s(N-H), and at 3312 cm^{-1} for asymmetric, v_{as}(N-H), modes. Fermi resonance at 3176 cm^{-1} is also observed.
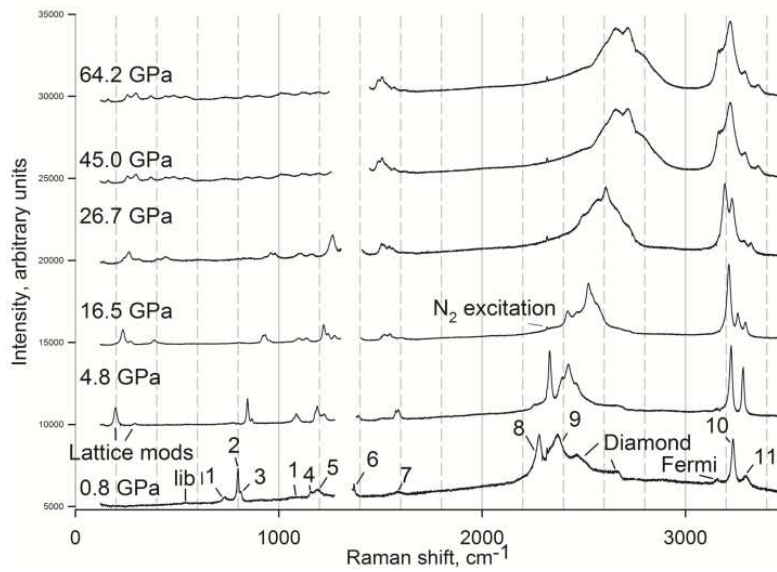

Fig. 5.4.4.1. Representative high pressure Raman spectra of **AB**. 1. N-H and B-H rocking deformation modes ρ(N-B-H). 2. ^{11}B-N stretching mode $v(^{11}$B-N). 3. ^{10}B-N stretching mode $v(^{10}$B-N). 4. Symmetric B-H bending mode ω_s(B-H). 5. Asymmetric B-H bending mode ω_s(B-H). 6. Symmetric N-H bending mode ω_s(N-H). 7. Asymmetric N-H bending mode ω_{as}(N-H). 8. Symmetric B-H stretching mode v_s(B-H). 9. Asymmetric B-H stretching mode v_s(B-H). 10. Symmetric N-H stretching mode v_s(N-H). 11. Asymmetric B-H stretching mode v_s(B-H).

Lattice vibration region

The Raman spectra of **AB** and the Raman frequency shift as a function of pressure for the lattice vibration region (100 cm^{-1} to 700 cm^{-1}) are shown in Fig. 5.4.4.2. At 0.8 GPa none of the lattice modes are observed. At pressure of 2.4 GPa there are two clearly seen lattice modes: LM1 at 180 cm^{-1} and LM2 at 237 cm^{-1}. With increasing pressure both modes exhibit the blue shift and one new mode LM3 at 245 cm^{-1} appears at 10.2 GPa . The monotonous blue shift of the all three

Table 5.4.4.1. The pressure dependence of the Raman shift (dv/dP, cm^{-1}/GPa) of various Raman modes of **AB** within three pressure intervals corresponding to different high pressure phases.

phase mode	2-10 GPa phase	10-26 GPa phase	Above 26 GPa phase
LM1	4.0(7)	3.09(13)	1.90(5)
LM2	18.8(1.6)	5.2(3)	2.42(12)
LM3	-	3.77(14)	2.87(17)
LM4	-	-	1.18(10)
LM5	-	-	1.97(12)
LM6	-	-	2.75(8)
LM7	-	-	1.59(6)
LM8	-	-	2.89(8)
Low frequency ρ(N-B-H)$_1$	4.4(5)	3.6(3)	2.39(7)
Low frequency ρ(N-B-H)$_2$	-	2.11(13)	1.29(5)
Low frequency ρ(N-B-H)$_3$	-	-	1.3(4)
High frequency ρ(N-B-H)$_1$	3.3(8)	0.84(10)	1.18(4)
High frequency ρ(N-B-H)$_2$	4.6(4)	2.91(15)	1.92(6)
High frequency ρ(N-B-H)$_3$	-	1.6(4)	-
$v(^{11}$B-N$)_1$	8.5(7)	4.2(3)	3.36(15)
$v(^{11}$B-N$)_2$	-	5.2(4)	3.70(18)
$v(^{11}$B-N$)_3$	-	-	3.7(5)
$v(^{10}$B-N$)$	9.1(6)	4.9(3)	4.3(3)
ω_s(B-H)	2.8(3)		
ω_{as}(B-H)$_1$	2.1(4)	2.68(15)	2.40(13)
ω_{as}(B-H)$_2$	4.9(5)	5.4(3)	-
ω_{as}(B-H)$_3$	-	3.2(4)	2.53(9)
ω_s(N-H)	0.1(3)	-0.3(7)	
ω_{as}(N-H)	1.3(8)	1.6(2)	0.52(7)
v_s(B-H)	8.6(6)	6.7(4)	5.99(16)
v_{as}(B-H)$_1$	7.9(6)	8.3(5)	5.7(2)
v_{as}(B-H)$_2$	11.0(1.5)	5.8(4)	6.2(3)
v_{as}(B-H)$_3$	12.3(1.7)	7.9(6)	5.4(1.7)
v_s(N-H)	-0.9(3)	-1.67(15)	-1.75(4)
v_{as}(N-H)$_1$	-1.5(4)	-2.9(3)	-0.34(13)
v_{as}(N-H)$_2$	-	2.9(3)	2.13(4)
v_{as}(N-H)$_3$	-	-	0.29(8)

lattice modes is observed up to 26.0 GPa when splitting of LM2 occurs. The single LM2 mode splits at into two peaks located at 398 cm^{-1} (LM5) and at 435 cm^{-1} (LM2). The latter has a broad shoulder (see Chapter 5.4.8 for better resolution) extended to at approximately 485 cm^{-1}. Upon further compression this shoulder becomes a clearly resolved peak (LM6) that indicates that the LM2 singlet splits in fact into a triplet above ~ 26 GPa. At 26.7 GPa LM1 splits into two peaks with approximate separation of 20 cm^{-1}. Further shift of the both peaks under pressure is characterized by the very similar pressure dependence dv/dP (Table 5.4.4.1). One new mode LM7 at 138 cm^{-1} appears at 26.7 GPa. All lattice modes above 26.7 GPa exhibit blue shift without any significant changes both in the shape of the peaks and in their pressure dependence (Table 5.4.4.1). At 53.5 GPa LM3 splits into a doublet with ~ 5 cm^{-1} between the bands.
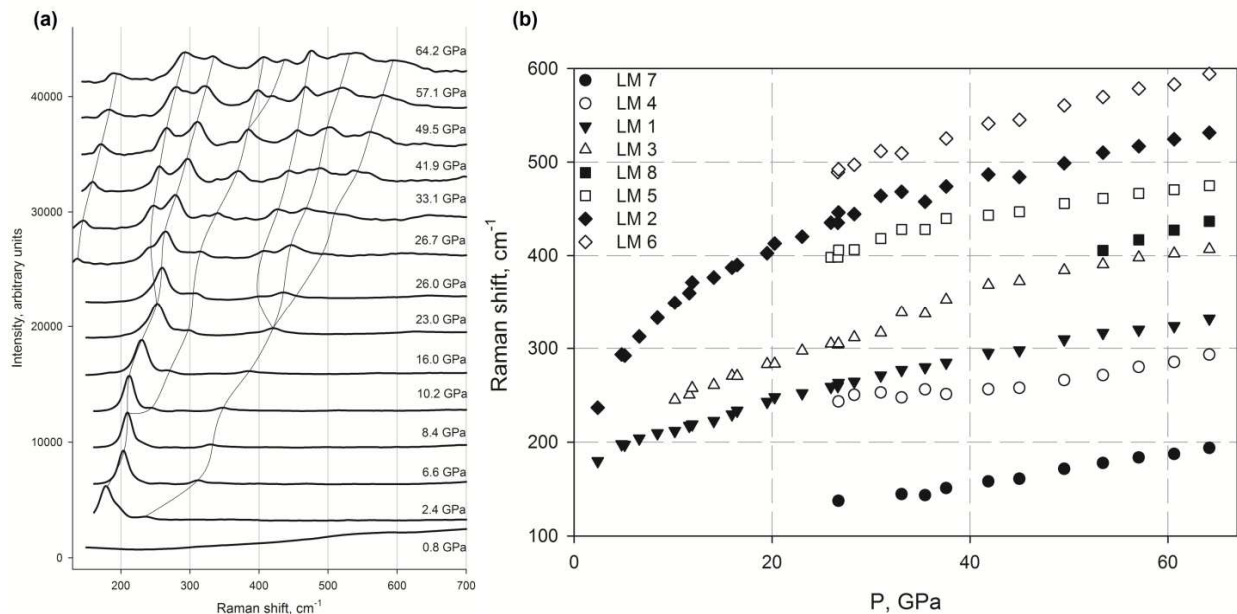

Fig. 5.4.4.2. Raman spectra of **AB** shown in the lattice vibration region (a) and the Raman frequency shift as a function of pressure (b).

B-H and N-H rocking deformation region

The Raman spectra and the Raman frequency shift as a function of pressure for the B-H and N-H rocking deformation region are shown in Fig. 5.4.4.3. Low frequency mode (738 cm^{-1}) splits into a doublet at 2.4 GPa that exhibits blue shift up to 6.6 GPa where this doublet cannot be resolved, then at 16.0 GPa a splitting to a doublet occurs once again. At 26.7 GPa a weak low frequency shoulder of this mode appears. This shoulder cannot be resolved above 41.9 GPa. High

frequency mode (1093 cm^{-1}) that looks like a broad weak peak at 0.8 GPa shows red shift and appears as a part of a doublet at 2.4 GPa. Upon further compression it splits into a triplet at 6.6 GPa. At 10.2 GPa a splitting of the central peak of the triplet occurs accompanied with weakening of high and low frequency shoulders. At 11.6 GPa high frequency B-H and N-H rocking deformation mode appears as a doublet at that blue shifts up to the maximum pressure achieved in this study.
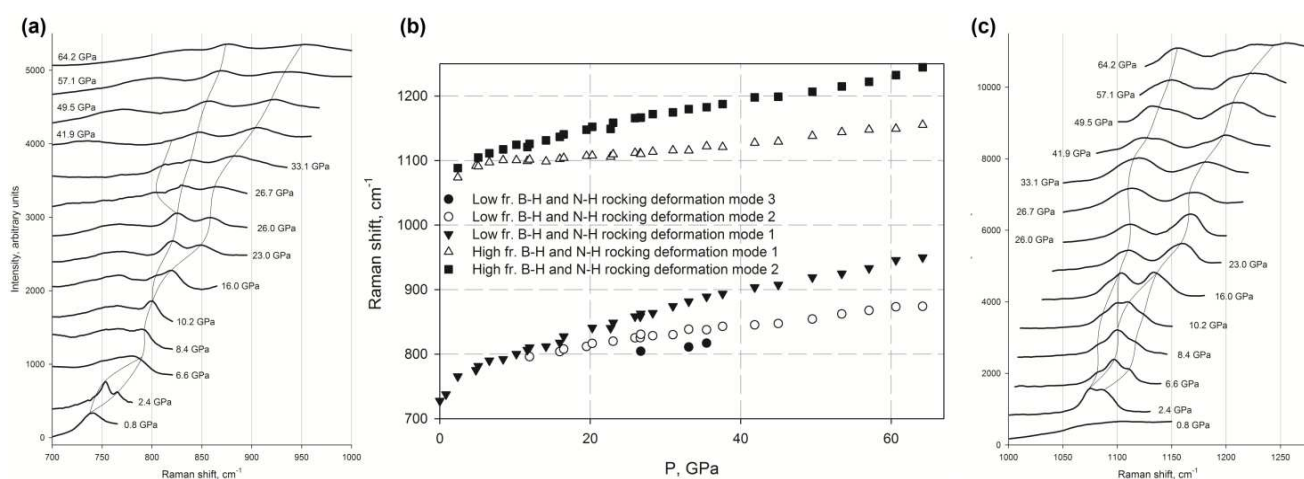

Fig. 5.4.4.3. Raman spectra of **AB** in the B-H and N-H rocking deformation region (a,c) and the Raman frequency shift as a function of pressure (b).

B-N stretching region

The Raman spectra and the Raman frequency shift as a function of pressure for the B-N stretching region are shown in Fig. 5.4.4.4. Frequencies of both B-N stretching modes significantly increase with pressure (Table 5.4.4.1) up to 10.2 GPa when splitting of the ^{11}B-N mode occurs. At 26.7 GPa the ^{10}B-N mode can be seen only as a weak shoulder and a low frequency shoulder of ^{11}B-N mode is appearing. All four peaks continue increasing in frequency with pressure and merge into a broad single peak at around 45 GPa.

B-H bending region

The Raman spectra and the Raman frequency shift as a function of pressure for the B-H bending region are shown in Fig. 5.4.4.5. The symmetric B-H bending mode clearly seen at 0.8 GPa is decreasing in intensity with pressure and is barely detectable at 8.4 GPa. The asymmetric mode splits into a doublet at 2.4 GPa. With further pressure increase it exhibits a blue shift, and at 11.6

GPa it splits again. Above 26 GPa this doublet merges into one peak and remains single up to 45 GPa when the band is masked by the diamond vibrational band at 1332 cm^{-1}.
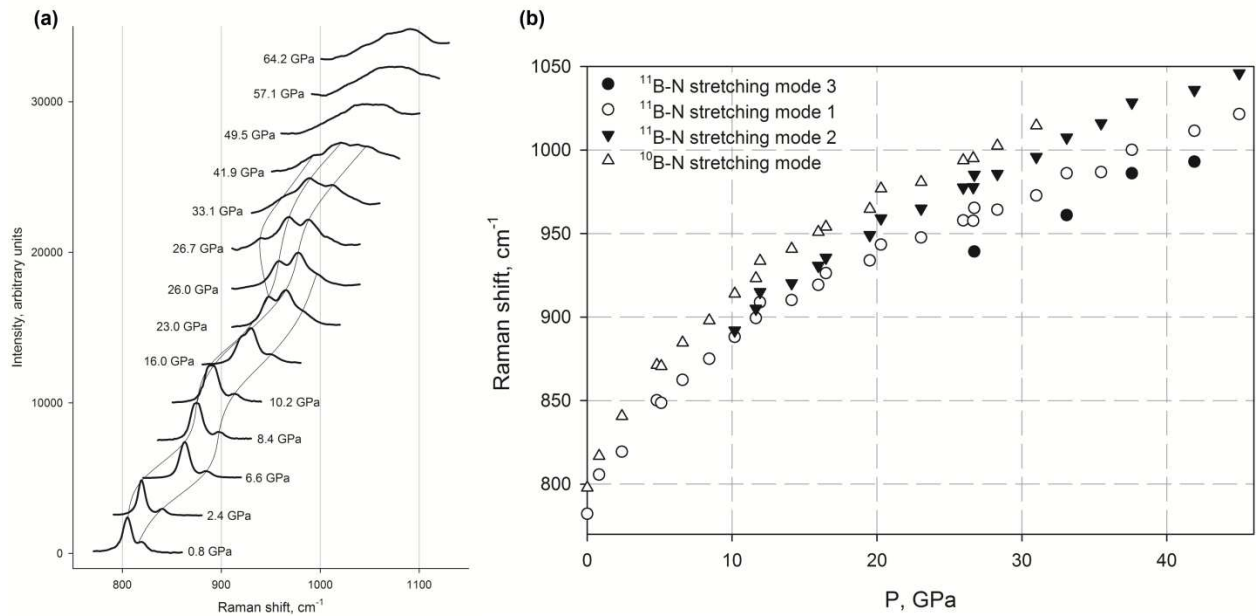

Fig. 5.4.4.4. Raman spectra of **AB** in the B-N stretching region (a) and the Raman frequency shift as a function of pressure (b).
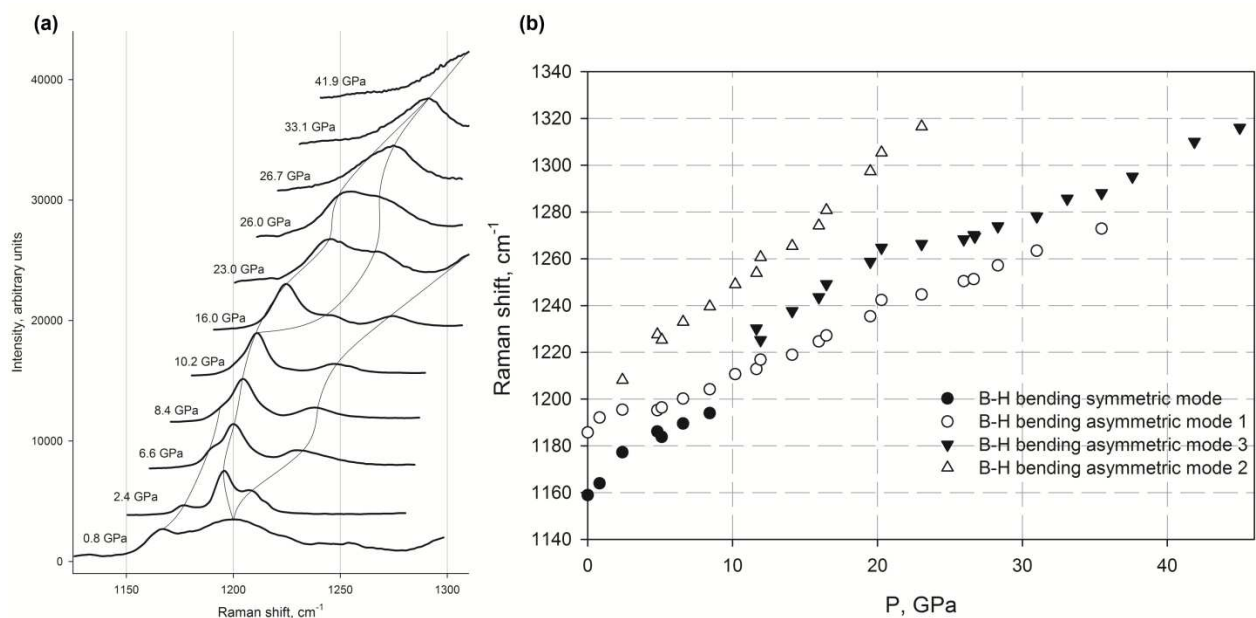

Fig.5.4.4.5. Raman spectra of **AB** in the B-H bending region (a) and the Raman frequency shift as a function of pressure (b).

N-H bending region

The Raman spectra and the Raman frequency shift as a function of pressure for the N-H bending region are shown in Fig. 5.4.4.6. The symmetric bending mode stays as a singlet with no changes and coalesced into the diamond peak above 16.0 GPa and is not presented. The asymmetric mode at 2.4 GPa splits into a doublet and is red shifting in the pressure range 0.8-4.8 GPa. Above 4.8 GPa it shows blue shift and at 10.2 GPa merges to a singlet. With further pressure increase this mode rapidly loses intensity and can be seen only as a very weak peak at 16.5 GPa. At 11.9 GPa a broad peak at 1540 cm^{-1} which is ascribed as an overtone of the low frequency N-H rocking modes is clearly seen. With increasing pressure it first splits into a doublet at 16.0 GPa and then both these peaks split again at 26.7 GPa.
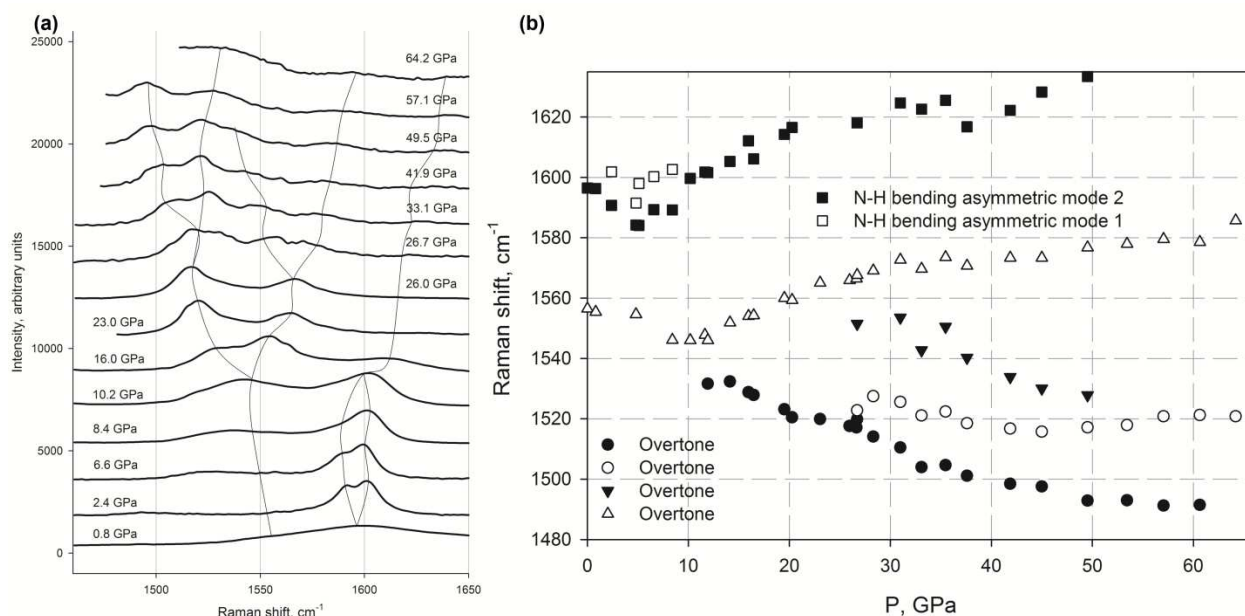

Fig. 5.4.4.6. Raman spectra of **AB** in the N-H bending region (a) and the Raman frequency shift as a function of pressure (b).

B-H stretching region

The Raman spectra and the Raman frequency shift as a function of pressure for the B-H stretching region are shown in Fig. 5.4.4.7. All modes between 2200 and 2600 cm^{-1} exhibit blue shift during compression. At 0.8 GPa three main peaks are observed: the B-H symmetric mode at 2291 cm^{-1}, the B-H asymmetric mode at 2382 cm^{-1}, and a broad shoulder at 2460 cm^{-1} that is the second-order Raman peak of diamond (Xu et al., 2002). At 2.4 GPa this shoulder disappears

while the asymmetric mode splits into a doublet and also the 2365 cm^{-1} mode, assigned in (Lin et al., 2008) as an overtone of the B-H bending mode, is seen. (The small narrow peak at 2331 cm^{-1} which is not affected by pressure is an excitation of N_2 molecules in the air). Upon further compression all four modes continue blue shifting and become worse resolved with no significant changes up to 64 GPa.
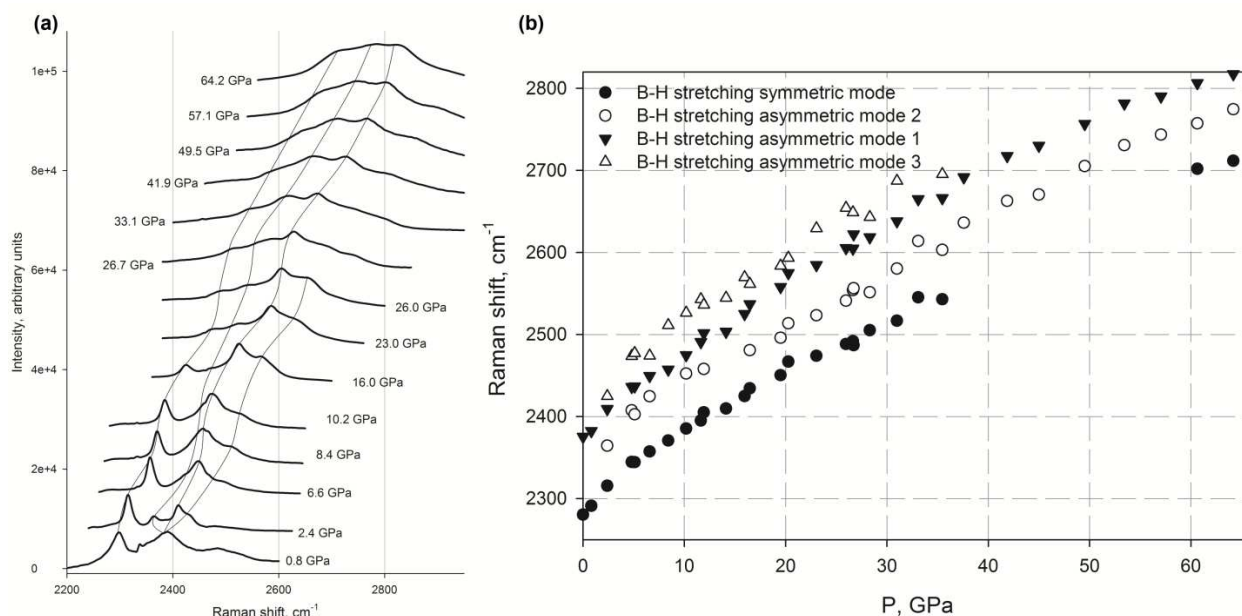

Fig. 5.4.4.7. Raman spectra of **AB** in the B-H stretching region (a) and the Raman frequency shift as a function of pressure (b).

N-H stretching region

The Raman spectra and the Raman frequency shift as a function of pressure for the B-H stretching region are shown in Fig. 5.4.4.8. Fermi resonant and both N-H stretching modes show red shifting at pressures between 0.8 and 5.1 GPa. At 6.6 GPa the Fermi resonant mode disappears, while the stretching modes continue red shifting. At 16.0 GPa the asymmetric mode splits into a doublet. The higher frequency peak of the doublet starts blue shifting and the lower frequency peak continues red shifting. At 26.0 GPa the higher frequency mode splits into two modes again, both exhibiting blue shifting but with different pressure dependences (Table 5.4.4.1). The symmetric mode red shifts up to maximum pressure achieved in this study, 64 GPa, while the low frequency peak of the asymmetric mode shows no significant shifting above 30 GPa.

106
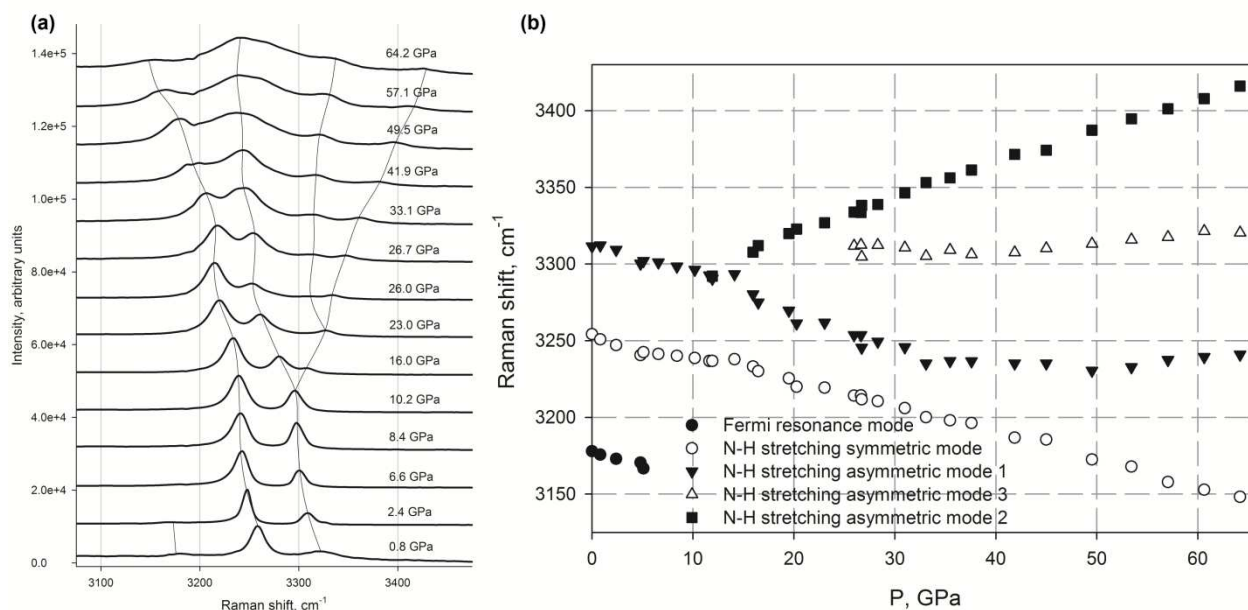
Fig.5.4.4 8. Raman spectra of **AB** in the N-H stretching region (a) and the Raman frequency shift as a function of pressure (b).

D. Second harmonic generation

The observation and spectral measurements of the generated second harmonic (SH) of the laser light were made up to 130 GPa (Fig. 5.4.4.9). At each pressure step measurements of position of the peak, its intensity and the full width at half maximum was made at different powers of the exiting light. No any notable changes of the position of the peak (λ=535.44 nm) and of the full width at half maximum (0.2 nm at 10 W power of the exciting laser) with respect to the pressure were observed. It is difficult to comment on absolute values of the SH intensity as a function of
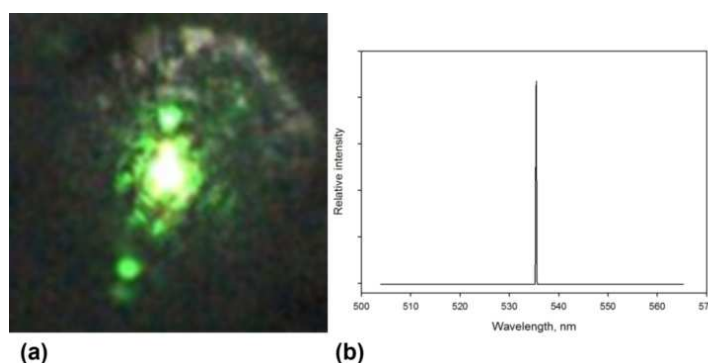

Fig. 5.4.4.9. Photograph showing the green light generated upon irradiation of **AB** by the NIR (1070 nm) light at 130 GPa (a); the spectrum of the corresponding SHG (b).

pressure because the intensity is strongly affected by thickness of the generating medium (Klimontovich, 1966) and it is hardly possible to conduct measurements at exactly the same point of the sample. However, the SHG effect was clearly observed up to the highest pressure, 130 GPa, reached in this study (Fig. 5.4.4.9) that implies the absence of the center of inversion in the point group symmetry of all **AB** phases detected throughout this pressure interval.

5.4.5 Discussion

The low-pressure phase transformation at about 1 GPa (Tr. I), is well established and described in literature (Andersson et al., 2011; Chellappa et al., 2009; Chen et al., 2010; Custelcean & Dreger, 2003; Filinchuk et al., 2009; Kumar et al., 2010; Lin et al., 2008; Nylén et al., 2009; Xie et al., 2009), so that we did not focus on it in this work. Based on the analysis of the behavior of the Raman modes above about 5 GPa described in Chapter 5.4.4, we report two phase transitions in **AB** observed in the present study: at around 10 GPa (Tr. II) and 26 GPa (Tr. III). The clear manifestation of Tr. II is splitting of the LM1 and ^{11}B-N stretching modes, each one into a doublet (Fig. 5.4.4.2 and Fig. 5.4.4.4 respectively), observed at 10.2 GPa. Although splitting of the low frequency asymmetric B-H bending mode is clearly seen only at 11.6 GPa and splitting of the asymmetric N-H stretching mode and low frequency B-H and N-H rocking deformation mode are clearly seen only at 16.0 GPa, the broadening and asymmetric form of the corresponding peaks is already visible at 10.2 GPa (Figs. 5.4.4.3, 5.4.4.5 and 5.4.4.8) indicated as the pressure of Tr. II. At the same pressure the asymmetric N-H bending mode merges from a doublet to a singlet (Fig. 5.4.4.6). The high frequency B-H and N-H rocking deformation modes merge from triplet to a doublet also at 10.2 GPa (Fig. 5.4.4.3c). The comparison of our observations with other studies is presented in Table 5.4.5.1.

Significant changes are seen in Raman spectra at approximately 26 GPa. First, further splitting of LM1 is obvious, and splitting of LM2 and low frequency B-H and N-H rocking deformation modes (not reported in any previous publications) is observed (Fig. 5.4.4.3). Second, the new LM7 lattice mode appears at 26.7 GPa (Fig. 5.4.4.2) and the high frequency asymmetric N-H stretching mode splits (Fig. 5.4.4.8). In the work by Chellappa et al. (2009) similar splitting was declared to occur in the **AB**-H_2 complex, but we did not detect any hydrogen modes by the Raman spectroscopy in the 4150-4450 cm^{-1} range. The low frequency peak of the asymmetric B-H bending mode merges into a singlet at this pressure

In the entire pressure interval studied all Raman modes of **AB** are blue shifting upon further compression above 26 GPa except the symmetric and low frequency asymmetric N-H stretching modes that are red shifting. Such behavior of the modes indicates strengthening of the B-H···H-N dihydrogen bonding at higher pressures. Our result is in odds with Chellappa et al. (2009) where the partial breakdown of dihydrogen bond is declared due to reversing of the pressure dependence of the symmetric N-H stretching mode beyond 50 GPa.

Table 5.4.5.1. The comparison of this study with Chellappa et al. (2009), Lin et al. (2008), and Xie et al.(2009).

This study	Lin et al. (2008)	Chellappa et al. (2009)	Xie et al. (2009)
Tr. II at around 10GPa			
Splitting of LM1	not observed	observed	observed at 5 GPa
Splitting of [11]B-N stretching mode	observed	not observed	not observed
Splitting of asymmetric B-H bending mode	observed	observed	observed
Splitting of asymmetric N-H stretching mode	not observed	observed	not observed
Splitting of low frequency B-H and N-H rocking deformation mode	observed	not observed	not observed
Merging to a singlet of asymmetric N-H bending mode	was always a singlet	observed	observed
Merging to a doublet of high frequency B-H and N-H rocking deformation modes	not observed	not observed	observed
Tr. III at around 26 GPa			
Further splitting of LM1	-	not observed	-
Splitting of LM2	-	not observed	-
Splitting of low frequency B-H and N-H rocking deformation modes	-	not observed	-
Appearing of LM7	-	not observed	-
Splitting of high frequency asymmetric N-H stretching mode	-	observed in **AB**-H_2 complex	-
Merging of asymmetric B-H bending mode	-	observed	-

Several spectra of **AB** were collected during decompression. Considerable hysteresis was observed for the second phase transition. While the phase III first appears at 26 GPa on compression, the peaks corresponding to this phase were detected down to 19.4 GPa. Hysteresis was not observed for the first phase transition (near 10 GPa) between phases I and II.

Based on the available Raman spectroscopy data we can suppose that the reported phase transitions happen due to strengthening of hydrogen bonding which leads to the appearance of richer Raman spectra. In turn, strengthening of the H-H interactions may explain relatively low pressure dependence of the Raman shift for such a rather soft material as **AB**.
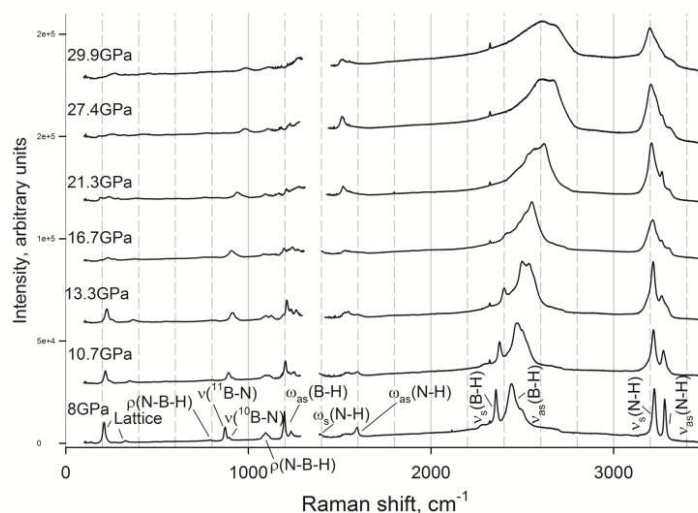

Fig.5.4.5.1. Representative high pressure Raman spectra taken upon non–hydrostatic compression of **AB**.

In order to find reasons of some differences in Raman modes behavior in our study compared to Chellappa et al. (2009), Lin et al. (2008), and Xie et al. (2009) we have investigated several cells loaded with no pressure transmitting medium. Raman vibrational spectra of **AB** under non-hydrostatic conditions were measured in the pressure interval from 8 to 29 GPa (Fig. 5.4.5.1). The resolution of Raman peaks became much worse so that the splitting of some modes just could not be detected. Besides a lack of resolution, the major difference between the spectra obtained in hydrostatic and non-hydrostatic conditions is that the splitting of the lattice modes and N-H stretching modes, occurring only at 26 GPa in hydrostatic conditions, starts at lower pressure, of about 16 GPa in non-hydrostatic conditions and is manifested in a little different way. Namely, in non-hydrostatic conditions in the lattice region only splitting of LM1 (Fig. 5.4.5.2b) occurs without splitting of LM2 and appearing of a new LM7 mode (Fig. 5.4.5.2a). In

the N-H stretching region the splitting of the low frequency asymmetric stretching mode takes place (Fig. 5.4.5.2d) in non-hydrostatic conditions, while in hydrostatic conditions the high frequency asymmetric mode splits (Fig. 5.4.5.2c). So it may be that hydrostatic conditions not only change the pressure of the phase transition, but also allow a transformation to a different phase. That can explain some discrepancy in observations in our study and previous ones.
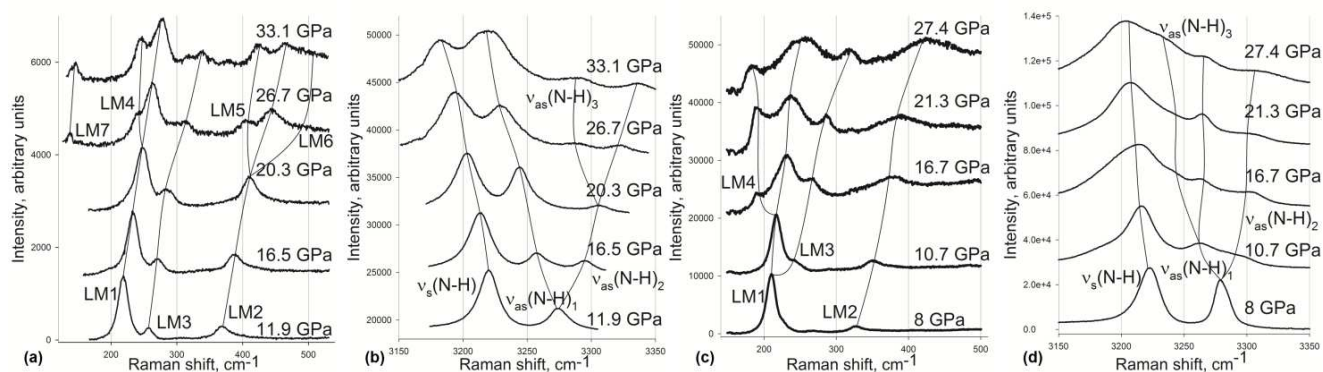

Fig. 5.4.5.2. Comparison of Raman spectra of **AB** obtained at hydrostatic (a) and (c) and non-hydrostatic (b) and (d) compression. (a) and (b) – lattice region, (c) and (d) – N-H stretching region.

In-house X-ray studies of the crystal structure of **AB** at high pressure are difficult due to the low scattering power of elements forming ammonia borane. Therefore there is no any structural data on **AB** at pressures above 27 GPa. That is why any additional information about the symmetry of high-pressure phase(s) is valuable. It is well-known that the SHG is only possible in anisotropic media without inversion symmetry (Klimontovich, 1966). Thus, due to the observation of the SHG in the whole studied pressure interval, we are able to definitely declare that regardless pressure ranges and phase transformations AB stays as a non-centrosymmetric structure up to at least 130 GPa.

5.4.6   Conclusions

Two pressure induced phase transitions in **AB** were observed based on the Raman spectroscopy data. The transitions were identified on the increase of the number of the Raman modes at pressures of 10 GPa and 26 GPa. The red shift of the vibrational frequency of the symmetric N-H stretching mode up to 65 GPa suggests strengthening of the dihydrogen bond. It was found that the material behaves differently under hydrostatic and non-hydrostatic compression. **AB** was found to have nonlinear optical properties, namely the ability for the laser light second harmonic

generation that is an evidence of the absence of the center of symmetry in the crystal structure of the **AB** high pressure polymorphs. The X-ray structural investigations are necessary in the future for identification of the high-pressure phases of **AB**.

5.4.7 Acknowledgment

### 5.4.8 Supplementary materials
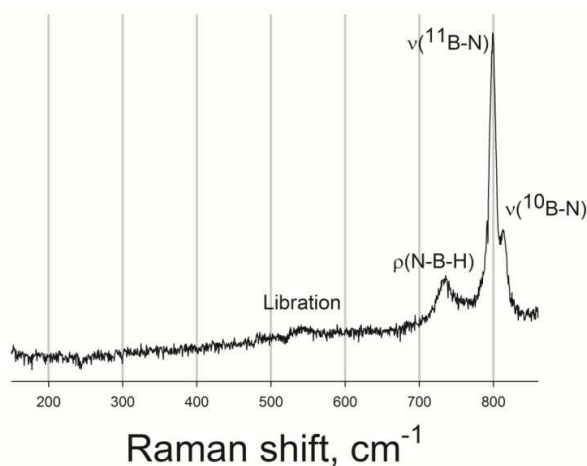
Fig. 5.4.8.1. Raman spectrum of **AB** shown in the lattice vibration region, low frequency B-H and N-H rocking deformation region and B-N stretching region at 0.8 GPa.
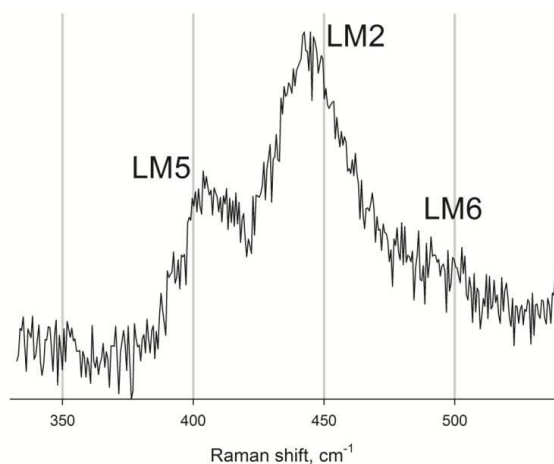

Fig. 5.4.8.2. Raman spectrum of **AB** shown in the high frequency lattice region at 26.7 GPa.

112

VI. References

Akahama, Y., Kawamura, H., 2006. Pressure calibration of diamond anvil Raman gauge to 310 GPa. J. Appl. Phys. 100, 043516.

Anders, E., Ebihara, M., 1982. Solar-system abundances of the elements. Geochim. Cosmochim. Acta 46, 2363–2380.

Anderson, D.L., 1989. Theory of the Earth. Blackwell Scientific Publications.

Andersson, O., Filinchuk, Y., Dmitriev, V., Quwar, I., Talyzin, A., Sundqvist, B., 2011. Phase coexistence and hysteresis effects in the pressure-temperature phase diagram of NH_3BH_3. Phys. Rev. B 84, 1–11.

Anzellini, S., Dewaele, A., Mezouar, M., Loubeyre, P., Morard, G., 2013. Melting of iron at Earth's inner core boundary based on fast X-ray diffraction. Science 340, 464–6.

Badro, J., Fiquet, G., Guyot, F., Rueff, J.-P., Struzhkin, V. V, Vankó, G., Monaco, G., 2003. Iron partitioning in Earth's mantle: toward a deep lower mantle discontinuity. Science 300, 789–91.

Badro, J., Rueff, J.-P., Vankó, G., Monaco, G., Fiquet, G., Guyot, F., 2004. Electronic transitions in perovskite: possible nonconvecting layers in the lower mantle. Science 305, 383–386.

Baitalow, F., Baumann, J., Wolf, G., Jaenicke-Rößler, K., Leitner, G., 2002. Thermal decomposition of B–N–H compounds investigated by using combined thermoanalytical methods. Thermochim. Acta 391, 159–168.

Baumann, J., Baitalow, F., Wolf, G., 2005. Thermal decomposition of polymeric aminoborane $(H_2BNH_2)_x$ under hydrogen release. Thermochim. Acta 430, 9–14.

Bengtson, A., Li, J., Morgan, D., 2009. Mössbauer modeling to interpret the spin state of iron in $(Mg,Fe)SiO_3$ perovskite. Geophys. Res. Lett. 36, L15301.

Bengtson, A., Persson, K., Morgan, D., 2008. Ab initio study of the composition dependence of the pressure-induced spin crossover in perovskite $(Mg_{1-x},Fe_x)SiO_3$. Earth Planet. Sci. Lett. 265, 535–545.

Blaquiere, N., Diallo-Garcia, S., Gorelsky, S.I., Black, D.A., Fagnou, K., 2008. Ruthenium-catalyzed dehydrogenation of ammonia boranes. J. Am. Chem. Soc. 130, 14034–5.

Boehler, R., 1993. Temperatures in the Earth's core from melting-point measurements of iron at high static pressures. Nature 363, 534–536.

Boehler, R., 2000. High-pressure experiments and the phase diagram of lower mantle and core materials. Rev. Geophys. 38, 221.

Boehler, R., Musshoff, H.G., Ditz, R., Aquilanti, G., Trapananti, A., 2009. Portable laser-heating stand for synchrotron applications. Rev. Sci. Instrum. 80, 045103.

Boehler, R., Santamaría-Pérez, D., Errandonea, D., Mezouar, M., 2008. Melting, density, and anisotropy of iron at core conditions: new x-ray measurements to 150 GPa. J. Phys. Conf. Ser. 121, 022018.

Boffa Ballaran, T., Kurnosov, A., Glazyrin, K., Frost, D.J., Merlini, M., Hanfland, M., Caracas, R., 2012. Effect of chemistry on the compressibility of silicate perovskite in the lower mantle. Earth Planet. Sci. Lett. 333-334, 181–190.

Bowden, M., Autrey, T., Brown, I., Ryan, M., 2008. The thermal decomposition of ammonia borane: A potential hydrogen storage material. Curr. Appl. Phys. 8, 498–500.

Bowden, M.E., Gainsford, G.J., Robinson, W.T., 2007. Room-Temperature Structure of Ammonia Borane. Aust. J. Chem. 60, 149.

Bowley, H.J., Gardiner, D.J., Gerrard, D.L., Graves, P.R., Louden, J.D., Turrell, G., 1990. Practical Raman Spectroscopy. Berichte der Bunsengesellschaft für Phys. Chemie 94, 1047–1047.

Boyd, F.R., England, J.L., 1960. Apparatus for phase-equilibrium measurements at pressures up to 50 kilobars and temperatures up to 1750°C. J. Geophys. Res. 65, 741–748.

Burns, R.G., 1993. Mineralogical Applications of Crystal Field Theory, Second ed. Cambridge University Press.

Campbell, A.J., Seagle, C.T., Heinz, D.L., Shen, G., Prakapenka, V.B., 2007. Partial melting in the iron–sulfur system at high pressure: A synchrotron X-ray diffraction study. Phys. Earth Planet. Inter. 162, 119–128.

Caracas, R., Mainprice, D., Thomas, C., 2010. Is the spin transition in Fe^{2+}-bearing perovskite visible in seismology? Geophys. Res. Lett. 37, L13309.

Catalli, K., Shim, S.-H., Dera, P., Prakapenka, V.B., Zhao, J., Sturhahn, W., Chow, P., Xiao, Y., Cynn, H., Evans, W.J., 2011. Effects of the Fe^{3+} spin transition on the properties of aluminous perovskite—New insights for lower-mantle seismic heterogeneities. Earth Planet. Sci. Lett. 310, 293–302.

Catalli, K., Shim, S.-H., Prakapenka, V.B., Zhao, J., Sturhahn, W., Chow, P., Xiao, Y., Liu, H., Cynn, H., Evans, W.J., 2010. Spin state of ferric iron in $MgSiO_3$ perovskite and its effect on elastic properties. Earth Planet. Sci. Lett. 289, 68–75.

Chellappa, R.S., Somayazulu, M., Struzhkin, V. V, Autrey, T., Hemley, R.J., 2009. Pressure-induced complexation of NH_3BH_3-H_2. J. Chem. Phys. 131, 224515.

Chen, J., Couvy, H., Liu, H., Drozd, V., Daemen, L.L., Zhao, Y., Kao, C.-C., 2010. In situ X-ray study of ammonia borane at high pressures. Int. J. Hydrogen Energy 35, 11064–11070.

Custelcean, R., Dreger, Z.A., 2003. Dihydrogen Bonding under High Pressure: A Raman Study of BH_3NH_3 Molecular Crystal. J. Phys. Chem. B 107, 9231–9235.

Denney, M.C., Pons, V., Hebden, T.J., Heinekey, D.M., Goldberg, K.I., 2006. Efficient catalysis of ammonia borane dehydrogenation. J. Am. Chem. Soc. 128, 12048–9.

Dewaele, A., Datchi, F., Loubeyre, P., Mezouar, M., 2008. High pressure–high temperature equations of state of neon and diamond. Phys. Rev. B 77, 94106–94115.

Dubrovinskaia, N., Dubrovinsky, L., 2003. Whole-cell heater for the diamond anvil cell. Rev. Sci. Instrum. 74, 3433.

Dubrovinskaia, N., Dubrovinsky, L., Caracas, R., Hanfland, M., 2010. Diamond as a high pressure gauge up to 2.7 Mbar. Appl. Phys. Lett. 97, 251903.

Dubrovinsky, L., Boffa-Ballaran, T., Glazyrin, K., Kurnosov, A., Frost, D., Merlini, M., Hanfland, M., Prakapenka, V.B., Schouwink, P., Pippinger, T., Dubrovinskaia, N., 2010. Single-crystal X-ray diffraction at megabar pressures and temperatures of thousands of degrees. High Press. Res. 30, 620–633.

Dubrovinsky, L., Glazyrin, K., McCammon, C.A., Narygina, O., Greenberg, E., Übelhack, S., Chumakov, A.I., Pascarelli, S., Prakapenka, V., Bock, J., Dubrovinskaia, N., Ubelhack, S., 2009. Portable laser-heating system for diamond anvil cells. J. Synchrotron Radiat. 16, 737–741.

Dziewonski, A.M., Anderson, D.L., 1981. Preliminary reference Earth model. Phys. Earth Planet. Inter. 25, 297–356.

Eremets, M.I., 1996. High Pressure Experimental Methods. Oxford Science, Oxford.

Farrugia, L.J., 1999. WinGX suite for small-molecule single-crystal crystallography. J. Appl. Crystallogr. 32, 837–838.

Fei, Y., Ricolleau, A., Frank, M., Mibe, K., Shen, G., Prakapenka, V., 2007. High-Pressure Geoscience Special Feature: Toward an internally consistent pressure scale. Proc. Natl. Acad. Sci. 104, 9182–9186.

Filinchuk, Y., Nevidomskyy, A., Chernyshov, D., Dmitriev, V., 2009. High-pressure phase and transition phenomena in ammonia borane NH_3BH_3 from x-ray diffraction, Landau theory, and ab initio calculations. Phys. Rev. B 79, 1–11.

Fiquet, G., Guyot, F., Badro, J., 2008. The Earth's Lower Mantle and Core. Elements 4, 177–182.

Frost, D.J., Liebske, C., Langenhorst, F., McCammon, C.A., Tronnes, R.G., Rubie, D.C., 2004. Experimental evidence for the existence of iron-rich metal in the Earth ' s lower mantle. Nature 428, 409–412.

Fujino, K., Nishio-Hamane, D., Seto, Y., Sata, N., Nagai, T., Shinmei, T., Irifune, T., Ishii, H., Hiraoka, N., Cai, Y.Q., Tsuei, K.-D., 2012. Spin transition of ferric iron in Al-bearing Mg–perovskite up to 200 GPa and its implication for the lower mantle. Earth Planet. Sci. Lett. 317-318, 407–412.

Glazyrin, K., Boffa Ballaran, T., Frost, D.J., McCammon, C.A., Kantor, A., Merlini, M., Hanfland, M., Dubrovinsky, L., 2014. Magnesium silicate perovskite and effect of iron oxidation state on its bulk sound velocity at the conditions of the lower mantle. Earth Planet. Sci. Lett. 393, 182–186.

Goncharov, A.F., Haugen, B.D., Struzhkin, V. V, Beck, P., Jacobsen, S.D., 2008. Radiative conductivity in the Earth's lower mantle. Nature 456, 231–4.

Goodman, J., 2000. Secular Instability and Planetesimal Formation in the Dust Layer. Icarus 148, 537–549.

Greenberg, E., Rozenberg, G.K., Xu, W., Pasternak, M.P., McCammon, C.A., Glazyrin, K., Dubrovinsky, L.S., 2013. Mott transition in $CaFe_2O_4$ at around 50 GPa. Phys. Rev. B 88, 214109.

Greenwood, N.N., Gibb, T.C., 1971. Mossbauer Spectroscopy. Chapman and Hall Ltd, London.

Gregoryanz, E., Degtyareva, O., Somayazulu, M., Hemley, R., Mao, H., 2005. Melting of Dense Sodium. Phys. Rev. Lett. 94, 185502–185506.

Grocholski, B., Shim, S.-H., Sturhahn, W., Zhao, J., Xiao, Y., Chow, P.C., 2009. Spin and valence states of iron in $(Mg_{0.8}Fe_{0.2})SiO_3$ perovskite. Geophys. Res. Lett. 36, L24303.

Gu, T., Wu, X., Qin, S., Dubrovinsky, L., 2011. In situ high-pressure study of FeP: Implications for planetary cores. Phys. Earth Planet. Inter. 184, 154–159.

Häuserma, D., Hanfland, M., 1996. Optics and beamlines for high-pressure research at the european synchrotron radiation facility. High Press. Res. 14, 223–234.

Hess, N.J., Bowden, M.E., Parvanov, V.M., Mundy, C., Kathmann, S.M., Schenter, G.K., Autrey, T., 2008. Spectroscopic studies of the phase transition in ammonia borane: Raman spectroscopy of single crystal NH_3BH_3 as a function of temperature from 88 to 330 K. J. Chem. Phys. 128, 034508.

Hirose, K., 2006. Postperovskite phase transition and its geophysical implications. Rev. Geophys. 44, RG3001.

Housley, R., Hess, F., 1966. Analysis of Debye-Waller-Factor and Mössbauer-Thermal-Shift Measurements. I. General Theory. Phys. Rev. 146, 517–526.

Hsu, H., Blaha, P., Cococcioni, M., Wentzcovitch, R.M., 2011. Spin-State Crossover and Hyperfine Interactions of Ferric Iron in $MgSiO_3$ Perovskite. Phys. Rev. Lett. 106, 118501.

Hsu, H., Umemoto, K., Blaha, P., Wentzcovitch, R.M., 2010. Spin states and hyperfine interactions of iron in $(Mg,Fe)SiO_3$ perovskite under pressure. Earth Planet. Sci. Lett. 294, 19–26.

Hsu, H., Yu, Y.G., Wentzcovitch, R.M., 2012. Spin crossover of iron in aluminous $MgSiO_3$ perovskite and post-perovskite. Earth Planet. Sci. Lett. 359-360, 34–39.

Hu, M.G., Geanangel, R.A., Wendlandt, W.W., 1978. The thermal decomposition of ammonia borane. Thermochim. Acta 23 (2), 249–255.

Hummer, D., Fei, Y., 2012. Synthesis and crystal chemistry of Fe^{3+}-bearing $(Mg,Fe^{3+})(Si, Fe^{3+})O_3$ perovskite. Am. Mineral. 97, 1915–1921.

Irifune, T., Shinmei, T., McCammon, C.A., Miyajima, N., Rubie, D.C., Frost, D.J., 2010. Iron partitioning and density changes of pyrolite in Earth's lower mantle. Science 327, 193–195.

Jackson, J.M., 2005. A synchrotron Mossbauer spectroscopy study of $(Mg,Fe)SiO_3$ perovskite up to 120 GPa. Am. Mineral. 90, 199–205.

Kantor, I., Dubrovinsky, L., McCammon, C.A., 2006. Spin crossover in $(Mg,Fe)O$: A Mössbauer effect study with an alternative interpretation of x-ray emission spectroscopy data. Phys. Rev. B 73, 100101.

Kantor, I., Dubrovinsky, L., McCammon, C.A., Steinle-Neumann, G., Kantor, A., Skorodumova, N., Pascarelli, S., Aquilanti, G., 2009. Short-range order and Fe clustering in $Mg_{1-x}Fe_xO$ under high pressure. Phys. Rev. B 80, 014204.

Kantor, I., Prakapenka, V., Kantor, A., Dera, P., Kurnosov, A., Sinogeikin, S., Dubrovinskaia, N., Dubrovinsky, L., 2012. BX90: a new diamond anvil cell design for X-ray diffraction and optical measurements. Rev. Sci. Instrum. 83, 125102.

Klimontovich, Y.L., 1966. Kvantovye generatory sveta i nelinejnaya optika. Prosveshhenie, Moscow.

Kolesnikov, A., Kutcherov, V.G., Goncharov, A.F., 2009. Methane-derived hydrocarbons produced under upper-mantle conditions. Nat. Geosci. 2, 566–570.

117

Kotrbová, M., Kadečková, S., Novák, J., Brádler, J., Smirnov, G.V., Shvydko, Y.V., 1985. Growth and perfection of flux grown $FeBO_3$ and $^{57}FeBO_3$ crystals. J. Cryst. Growth 71, 607–614.

Kubo, A., Akaogi, M., 2000. Post-garnet transitions in the system $Mg_4Si_4O_{12}$–$Mg_3Al_2Si_3O_{12}$ up to 28 GPa: phase relations of garnet, ilmenite and perovskite. Phys. Earth Planet. Inter. 121, 85–102.

Kumar, R.S., Ke, X., Zhang, J., Lin, Z., Vogel, S.C., Hartl, M., Sinogeikin, S., Daemen, L., Cornelius, A.L., Chen, C., Zhao, Y., 2010. Pressure induced structural changes in the potential hydrogen storage compound ammonia borane: A combined X-ray, neutron and theoretical investigation. Chem. Phys. Lett. 495, 203–207.

Kupenko, I., Dubrovinsky, L., Dmitriev, V., Dubrovinskaia, N., 2012a. In situ Raman spectroscopic study of the pressure induced structural changes in ammonia borane. J. Chem. Phys. 137, 074506.

Kupenko, I., Dubrovinsky, L., Dubrovinskaia, N., McCammon, C.A., Glazyrin, K., Bykova, E., Ballaran, T.B., Sinmyo, R., Chumakov, a. I., Potapkin, V., Kantor, A., Rüffer, R., Hanfland, M., Crichton, W., Merlini, M., 2012b. Portable double-sided laser-heating system for Mössbauer spectroscopy and X-ray diffraction experiments at synchrotron facilities with diamond anvil cells. Rev. Sci. Instrum. 83, 124501.

Kupenko, I., McCammon, C.A., Sinmyo, R., Prescher, C., Chumakov, A.I., Kantor, A., Rüffer, R., Dubrovinsky, L., 2014. Electronic spin state of Fe,Al-containing $MgSiO_3$ perovskite at lower mantle conditions. Lithos 189, 167–172.

Kurnosov, A., Kantor, I., Boffa-Ballaran, T., Lindhardt, S., Dubrovinsky, L., Kuznetsov, A., Zehnder, B.H., 2008. A novel gas-loading system for mechanically closing of various types of diamond anvil cells. Rev. Sci. Instrum. 79, 045110.

Lauterbach, S., McCammon, C.A., van Aken, P., Langenhorst, F., Seifert, F., 2000. Mössbauer and ELNES spectroscopy of $(Mg,Fe)(Si,Al)O_3$ perovskite: a highly oxidised component of the lower mantle. Contrib. to Mineral. Petrol. 138, 17–26.

Lee, K.K.M., O'Neill, B., Panero, W.R., Shim, S.-H., Benedetti, L.R., Jeanloz, R., 2004. Equations of state of the high-pressure phases of a natural peridotite and implications for the Earth's lower mantle. Earth Planet. Sci. Lett. 223, 381–393.

Lewis, J., 2004. Physics and Chemistry of the Solar System, 2nd ed. Elsevier Academic Press, Boston.

Li, J., Struzhkin, V. V, Mao, H.-K., Shu, J., Hemley, R.J., Fei, Y., Mysen, B., Dera, P., Prakapenka, V., Shen, G., 2004. Electronic spin state of iron in lower mantle perovskite. Proc. Natl. Acad. Sci. U. S. A. 101, 14027–30.

Li, J., Sturhahn, W., Jackson, J.M., Struzhkin, V. V., Lin, J.F., Zhao, J., Mao, H.K., Shen, G., 2006. Pressure effect on the electronic structure of iron in (Mg,Fe)(Si,Al)O_3 perovskite: a combined synchrotron Mössbauer and X-ray emission spectroscopy study up to 100 GPa. Phys. Chem. Miner. 33, 575–585.

Li, L., 2005. Electronic spin state of ferric iron in Al-bearing perovskite in the lower mantle. Geophys. Res. Lett. 32, L17307.

Lin, J.-F., Alp, E.E., Mao, Z., Inoue, T., McCammon, C.A., Xiao, Y., Chow, P., Zhao, J., 2012. Electronic spin states of ferric and ferrous iron in the lower-mantle silicate perovskite. Am. Mineral. 97, 592–597.

Lin, J.-F., Degtyareva, O., Prewitt, C.T., Dera, P., Sata, N., Gregoryanz, E., Mao, H.-K., Hemley, R.J., 2004. Crystal structure of a high-pressure/high-temperature phase of alumina by in situ X-ray diffraction. Nat. Mater. 3, 389–93.

Lin, J.-F., Speziale, S., Prakapenka, V.B., Dera, P., Lavina, B., Watson, H.C., 2010. High-pressure X-ray diffraction and X-ray emission studies on iron-bearing silicate perovskite under high pressures. High Press. Res. 30, 230–237.

Lin, J.-F., Watson, H., Vankó, G., Alp, E.E., Prakapenka, V.B., Dera, P., Struzhkin, V. V., Kubo, A., Zhao, J., McCammon, C.A., Evans, W.J., 2008. Intermediate-spin ferrous iron in lowermost mantle post-perovskite and perovskite. Nat. Geosci. 1, 688–691.

Lin, Y., Ma, H., Matthews, C.W., Kolb, B., Sinogeikin, S., Thonhauser, T., Mao, W.L., 2012. Experimental and Theoretical Studies on a High Pressure Monoclinic Phase of Ammonia Borane. J. Phys. Chem. C 116, 2172–2178.

Lin, Y., Mao, W.L., Drozd, V., Chen, J., Daemen, L.L., 2008. Raman spectroscopy study of ammonia borane at high pressure. J. Chem. Phys. 129, 234509.

Liu, L.-G., 1976. The high-pressure phases of MgSiO_3. Earth Planet. Sci. Lett. 31, 200–208.

Lundin, S., Catalli, K., Santillán, J., Shim, S.-H., Prakapenka, V.B., Kunz, M., Meng, Y., 2008. Effect of Fe on the equation of state of mantle silicate perovskite over 1Mbar. Phys. Earth Planet. Inter. 168, 97–102.

Mao, H.K., Xu, J.J., Bell, P.M., 1986. Calibration of the ruby pressure gauge to 800 kbar under quasi-hydrostatic conditions. J. Geophys. Res. 91, 4673.

Mattern, E., Matas, J., Ricard, Y., Bass, J., 2005. Lower mantle composition and temperature from mineral physics and thermodynamic modelling. Geophys. J. Int. 160, 973–990.

McCammon, C.A., 1994. Mössbauer spectroscopy of quenched high-pressure phases: Investigating the Earth's interior. Hyperfine Interact. 90, 89–105.

McCammon, C.A., 1997. Perovskite as a possible sink for ferric iron in the lower mantle. Nature 387, 694–696.

McCammon, C.A., 2005. Geochemistry. The paradox of mantle redox. Science 308, 807–808.

McCammon, C.A., Dubrovinsky, L., Narygina, O., Kantor, I., Wu, X., Glazyrin, K., Sergueev, I., Chumakov, A.I., 2010. Low-spin Fe^{2+} in silicate perovskite and a possible layer at the base of the lower mantle. Phys. Earth Planet. Inter. 180, 215–221.

McCammon, C.A., Glazyrin, K., Kantor, A., Kantor, I., Kupenko, I., Narygina, O., Potapkin, V., Prescher, C., Sinmyo, R., Chumakov, A., Rüffer, R., Sergueev, I., Smirnov, G., Dubrovinsky, L., 2013. Iron spin state in silicate perovskite at conditions of the Earth's deep interior. High Press. Res. 1–10.

McCammon, C.A., Kantor, I., Narygina, O., Rouquette, J., Ponkratz, U., Sergueev, I., Mezouar, M., Prakapenka, V., Dubrovinsky, L., 2008. Stable intermediate-spin ferrous iron in lower-mantle perovskite. Nat. Geosci. 1, 684–687.

McCammon, C.A., Lauterbach, S., Seifert, F., Langenhorst, F., van Aken, P. a., 2004. Iron oxidation state in lower mantle mineral assemblages. Earth Planet. Sci. Lett. 222, 435–449.

Mikhaylushkin, A., Simak, S., Dubrovinsky, L., Dubrovinskaia, N., Johansson, B., Abrikosov, I., 2007. Pure Iron Compressed and Heated to Extreme Conditions. Phys. Rev. Lett. 99, 165505–165509.

Ming, L., Bassett, W.A., 1974. Laser heating in the diamond anvil press up to 2000°C sustained and 3000°C pulsed at pressures up to 260 kilobars. Rev. Sci. Instrum. 45, 1115.

Mössbauer, R.L., 1958. Kernresonanzfluoreszenz von Gammastrahlung in Ir^{191}. Zeitschrift für Anorg. und Allg. Chemier Phys. 151, 124–143.

Murakami, M., Hirose, K., Kawamura, K., Sata, N., Ohishi, Y., 2004. Post-perovskite phase transition in $MgSiO_3$. Science 304, 855–8.

Narygina, O., Dubrovinsky, L.S., Samuel, H., McCammon, C.A., Kantor, I.Y., Glazyrin, K., Pascarelli, S., Aquilanti, G., Prakapenka, V.B., 2011. Chemically homogeneous spin transition zone in Earth's lower mantle. Phys. Earth Planet. Inter. 185, 107–111.

Narygina, O. V., Kantor, I.Y., McCammon, C.A., Dubrovinsky, L.S., 2010. Electronic state of Fe^{2+} in $(Mg,Fe)(Si,Al)O_3$ perovskite and $(Mg,Fe)SiO_3$ majorite at pressures up to 81 GPa and temperatures up to 800 K. Phys. Chem. Miner. 37, 407–415.

Nylén, J., Sato, T., Soignard, E., Yarger, J.L., Stoyanov, E., Häussermann, U., 2009. Thermal decomposition of ammonia borane at high pressures. J. Chem. Phys. 131, 104506.

Ohta, K., Hirose, K., Onoda, S., Shimizu, K., 2007. The effect of iron spin transition on electrical conductivity of (Mg,Fe)O magnesiowüstite. Proc. Jpn. Acad. Ser. B. Phys. Biol. Sci. 83, 97–100.

Ohta, K., Hirose, K., Shimizu, K., Sata, N., Ohishi, Y., 2010. The electrical resistance measurements of $(Mg,Fe)SiO_3$ perovskite at high pressures and implications for electronic spin transition of iron. Phys. Earth Planet. Inter. 180, 154–158.

Palyanov, Y.N., Kupriyanov, I.N., Sokol, A.G., Khokhryakov, A.F., Borzdov, Y.M., 2011. Diamond Growth from a Phosphorus–Carbon System at High Pressure High Temperature Conditions. Cryst. Growth Des. 11, 2599–2605.

Parakhonskiy, G., Dubrovinskaia, N., Bykova, E., Wirth, R., Dubrovinsky, L., 2011. Experimental pressure-temperature phase diagram of boron: resolving the long-standing enigma. Sci. Rep. 1, DOI:10.1038/srep00096.

Pippinger, T., Dubrovinsky, L., Glazyrin, K., Miletich, R., Dubrovinskaia, N., 2011. Detection of melting by in-situ observation of spherical-drop formation in laser-heated diamond-anvil cells. Física la Tierra 23, 29–41.

Potapkin, V., Chumakov, A.I., Smirnov, G. V., Celse, J.-P., Rüffer, R., McCammon, C.A., Dubrovinsky, L., 2012. The [57]Fe synchrotron Mössbauer source at the ESRF. J. Synchrotron Radiat. 19, 559–569.

Potapkin, V., McCammon, C.A., Glazyrin, K., Kantor, A., Kupenko, I., Prescher, C., Sinmyo, R., Smirnov, G. V, Chumakov, A.I., Rüffer, R., Dubrovinsky, L., 2013. Effect of iron oxidation state on the electrical conductivity of the Earth's lower mantle. Nat. Commun. 4, 1427.

Prakapenka, V.B., Kubo, A., Kuznetsov, A., Laskin, A., Shkurikhin, O., Dera, P., Rivers, M.L., Sutton, S.R., 2008. Advanced flat top laser heating system for high pressure research at GSECARS: application to the melting behavior of germanium. High Press. Res. 28, 225–235.

Prescher, C., McCammon, C.A., Dubrovinsky, L., 2012. MossA : a program for analyzing energy-domain Mössbauer spectra from conventional and synchrotron sources. J. Appl. Crystallogr. 45, 329–331.

Ramzan, M., Ahuja, R., 2010. High pressure and temperature study of hydrogen storage material BH_3NH_3 from ab initio calculations. J. Phys. Chem. Solids 71, 1137–1139.

Ringwood, A.E., 1962. A model for the upper mantle. J. Geophys. Res. 67, 857–867.

Ringwood, A.E., 1982. Phase Transformations and Differentiation in Subducted Lithosphere: Implications for Mantle Dynamics, Basalt Petrogenesis, and Crustal Evolution. J. Geol. 90, 611–643.

Rüffer, R., Chumakov, A.I., 1996. Nuclear Resonance Beamline at ESRF. Hyperfine Interact. 97-98, 589–604.

Santoro, M., Lin, J.-F., Struzhkin, V. V., Mao, H., Hemley, R.J., 2005. In situ raman spectroscopy with laser-heated diamond anvil cells, in: Chen, J., Wang, Y., Duffy, T.S., Shen, G., Dobrzhinetskaya, L.F. (Eds.), Advances in High-Pressure Technology for Geophysical Applications. Elsevier B.V.

Schröder, T., Schneider, M., Rosenthal, T., Eisele, A., Gold, C., Scheidt, E.-W., Scherer, W., Berthold, R., Oeckler, O., 2011. Nanostructures in metastable $GeBi_2Te_4$ obtained by high-pressure synthesis and rapid quenching and their influence on physical properties. Phys. Rev. B 84, 184104–184114.

Schultz, E., Mezouar, M., Crichton, W., Bauchau, S., Blattmann, G., Andrault, D., Fiquet, G., Boehler, R., Rambert, N., Sitaud, B., Loubeyre, P., 2005. Double-sided laser heating system for in situ high pressure–high temperature monochromatic x-ray diffraction at the esrf. High Press. Res. 25, 71–83.

Sheldrick, G.M., 2008. A short history of SHELX. Acta Crystallogr. A. 64, 112–22.

Shen, G., Rivers, M.L., Wang, Y., Sutton, S.R., 2001. Laser heated diamond cell system at the Advanced Photon Source for in situ x-ray measurements at high pressure and temperature. Rev. Sci. Instrum. 72, 1273.

Shen, G., Wang, L., Ferry, R., Mao, H., Hemley, R.J., 2010. A portable laser heating microscope for high pressure research. J. Phys. Conf. Ser. 215, 012191.

Sinmyo, R., Pesce, G., Greenberg, E., McCammon, C.A., Dubrovinsky, L., 2014. Lower mantle electrical conductivity based on measurements of Al, Fe-bearing perovskite under lower mantle conditions. Earth Planet. Sci. Lett. 393, 165–172.

Smirnov, G. V., Sklyarevskii, V. V., Voskanyan, R.A., Artem'ev, A.N., 1969. Nuclear Diffraction of Resonant Radiation by an Antiferromagnetic Crystal. JETP Lett. 9, 70–73.

Smirnov, G. V., van Bürck, U., Chumakov, A.I., Baron, A.Q.R., Rüffer, R., 1997. Synchrotron Mössbauer source. Phys. Rev. B 55, 5811–5815.

Song, Q., Hou, Y.-Q., Li, L.-S., Jiang, Z.-Y., Zhou, B., Zhang, X.-D., 2012. Structural, elastic, and electronic properties of orthorhombic NH_3BH_3: An ab initio study. Phys. B Condens. Matter 407, 565–570.

Stackhouse, S., Brodholt, J.P., Price, G.D., 2007. Electronic spin transitions in iron-bearing $MgSiO_3$ perovskite. Earth Planet. Sci. Lett. 253, 282–290.

Stephens, F.H., Pons, V., Tom Baker, R., 2007. Ammonia-borane: the hydrogen source par excellence? Dalt. Trans. 2613–26.

Storozhenko, P.A., Svitsyn, R.A., Ketsko, V.A., Buryak, A.K., Ul'yanov, A. V., 2005. Ammineborane: Synthesis and physicochemical characterization. Russ. J. Inorg. Chem. 50, 980–985.

Sturhahn, W., 2000. CONUSS and PHOENIX: Evaluation of nuclear resonant scattering data. Hyperfine Interact. 125, 149–172.

Sturhahn, W., 2005. The spin state of iron in minerals of Earth's lower mantle. Geophys. Res. Lett. 32, L12307.

Umemoto, K., Hsu, H., Wentzcovitch, R.M., 2010. Effect of site degeneracies on the spin crossovers in (Mg, Fe)SiO_3 perovskite. Phys. Earth Planet. Inter. 180, 209–214.

Vanpeteghem, C.B., Angel, R.J., Ross, N.L., Jacobsen, S.D., Dobson, D.., Litasov, K.D., Ohtani, E., 2006. Al, Fe substitution in the MgSiO3 perovskite structure: A single-crystal X-ray diffraction study. Phys. Earth Planet. Inter. 155, 96–103.

Wang, L., Bao, K., Meng, X., Wang, X., Jiang, T., Cui, T., Liu, B., Zou, G., 2011. Structural and dynamical properties of solid ammonia borane under high pressure. J. Chem. Phys. 134, 024517.

Weir, C., Lippincott, E., Van Valkenburg, A., Bunting, E., 1959. Infrared studies in the 1- to 15-micron region to 30,000 atmospheres. J. Res. NBS, Sect. A Phys. Chem. 63A.

Wentzcovitch, R.M., Hsu, H., Umemoto, K., 2012. First-principles studies of spin-state crossovers of iron in perovskite. Eur. J. Mineral. 24, 851–862.

Wolf, G., Baumann, J., Baitalow, F., Hoffmann, F.., 2000. Calorimetric process monitoring of thermal decomposition of B–N–H compounds. Thermochim. Acta 343, 19–25.

Wu, X., Steinle-Neumann, G., Narygina, O., Kantor, I., McCammon, C.A., Prakapenka, V., Swamy, V., Dubrovinsky, L., 2009. High-Pressure Behavior of Perovskite: $FeTiO_3$ Dissociation into $(Fe_{1-\delta},Ti_\delta)O$ and $Fe_{1+\delta}Ti_{2-\delta}O5$. Phys. Rev. Lett. 103, 65503–65507.

Xie, S., Song, Y., Liu, Z., 2009. In situ high-pressure study of ammonia borane by Raman and IR spectroscopy. Can. J. Chem. 87, 1235–1247.

Xu, J., Mao, H., Hemley, R.J., 2002. The gem anvil cell: high-pressure behaviour of diamond and related materials. J. Phys. Condens. Matter 14, 11549–11552.

Xu, W., Greenberg, E., Rozenberg, G.K., Pasternak, M.P., Bykova, E., Boffa-Ballaran, T., Dubrovinsky, L., Prakapenka, V., Hanfland, M., Vekilova, O.Y., Simak, S.I., Abrikosov, I.A., 2013. Pressure-Induced Hydrogen Bond Symmetrization in Iron Oxyhydroxide. Phys. Rev. Lett. 111, 175501.

Yang, J.B., Lamsal, J., Cai, Q., James, W.J., Yelon, W.B., 2008. Structural evolution of ammonia borane for hydrogen storage. Appl. Phys. Lett. 92, 091916.

Zerr, A., Miehe, G., Li, J., Dzivenko, D.A., Bulatov, V.K., Höfer, H., Bolfan-Casanova, N., Fialin, M., Brey, G., Watanabe, T., Yoshimura, M., 2009. High-Pressure Synthesis of Tantalum Nitride Having Orthorhombic U_2S_3 Structure. Adv. Funct. Mater. 19, 2282–2288.

Zhai, S., Ito, E., 2011. Recent advances of high-pressure generation in a multianvil apparatus using sintered diamond anvils. Geosci. Front. 2, 101–106.

Zhang, F., Oganov, A.R., 2006. Valence state and spin transitions of iron in Earth's mantle silicates. Earth Planet. Sci. Lett. 249, 436–443.

Zhao, J., Sturhahn, W., Lin, J., Shen, G., Alp, E.E., Mao, H., 2004. Nuclear resonant scattering at high pressure and high temperature. High Press. Res. 24, 447–457.

(Eidesstattliche) Versicherungen und Erklärungen

(§ 8 S. 2 Nr. 6 PromO)

Hiermit erkläre ich mich damit einverstanden, dass die elektronische Fassung meiner Dissertation unter Wahrung meiner Urheberrechte und des Datenschutzes einer gesonderten Überprüfung hinsichtlich der eigenständigen Anfertigung der Dissertation unterzogen werden kann.

(§ 8 S. 2 Nr. 8 PromO)

Hiermit erkläre ich eidesstattlich, dass ich die Dissertation selbständig verfasst und keine anderen als die von mir angegebenen Quellen und Hilfsmittel benutzt habe.

(§ 8 S. 2 Nr. 9 PromO)

Ich habe die Dissertation nicht bereits zur Erlangung eines akademischen Grades anderweitig eingereicht und habe auch nicht bereits diese oder eine gleichartige Doktorprüfung endgültig nicht bestanden.

(§ 8 S. 2 Nr. 10 PromO)

Hiermit erkläre ich, dass ich keine Hilfe von gewerbliche Promotionsberatern bzw. -vermittlern in Anspruch genommen habe und auch künftig nicht nehmen werde.

……………………………………………………………………………………….

Ort, Datum, Unterschrift